

Electronic Thesis and Dissertation Repository

8-15-2023 10:00 AM

Towards Clinical Microscopic Fractional Anisotropy Imaging

Nico JJ Arezza, *Western University*

Supervisor: Baron, Corey, *The University of Western Ontario*

Co-Supervisor: Menon, Ravi, *The University of Western Ontario*

A thesis submitted in partial fulfillment of the requirements for the Doctor of Philosophy degree
in Medical Biophysics

© Nico JJ Arezza 2023

Follow this and additional works at: <https://ir.lib.uwo.ca/etd>



Part of the [Biomedical Engineering and Bioengineering Commons](#), [Biophysics Commons](#), and the
[Other Physics Commons](#)

Recommended Citation

Arezza, Nico JJ, "Towards Clinical Microscopic Fractional Anisotropy Imaging" (2023). *Electronic Thesis and Dissertation Repository*. 9522.

<https://ir.lib.uwo.ca/etd/9522>

This Dissertation/Thesis is brought to you for free and open access by Scholarship@Western. It has been accepted for inclusion in Electronic Thesis and Dissertation Repository by an authorized administrator of Scholarship@Western. For more information, please contact wlsadmin@uwo.ca.

Abstract

Microscopic fractional anisotropy (μ FA) is a diffusion-weighted magnetic resonance imaging (dMRI) metric that is sensitive to neuron microstructural features without being confounded by the orientation dispersion of axons and dendrites. μ FA may potentially act as a surrogate biomarker for neurodegeneration, demyelination, and other pathological changes to neuron microstructure with greater specificity than other dMRI techniques that are sensitive to orientation dispersion, such as diffusion tensor imaging. As with many advanced imaging techniques, μ FA is primarily used in research studies and has not seen use in clinical settings.

The primary goal of this Thesis was to assess the clinical viability of μ FA by developing a rapid protocol for full brain μ FA imaging and then applying it to the study of a neurological disease. **Chapter 1** presents the motivation behind this Thesis and a detailed summary of general background information that supports the subsequent chapters. **Chapter 2** focuses on the development and optimization of a μ FA imaging protocol that involves the acquisition of dMRI data in two encoding schemes, linear tensor encoding and spherical tensor encoding, and then a joint fit of the data to the powder kurtosis signal representation. The technique was shown to have good repeat measurement reliability in white matter and measured values strongly correlated with another μ FA computed using the gamma signal representation. In **Chapter 3**, a modified signal representation was investigated to estimate μ FA and other indices while mitigating contaminating partial volume effects from free water, such as the cerebrospinal fluid in ventricles. The work described in **Chapter 4** explores the sensitivity of μ FA to hippocampal abnormalities in patients with unilateral temporal lobe epilepsy. **Chapter 5** summarizes the contributions of this Thesis and provides suggestions for future studies.

Keywords: diffusion magnetic resonance imaging, diffusion kurtosis, microscopic fractional anisotropy, neuroimaging, free water elimination, temporal lobe epilepsy

Summary for Lay Audience

Medical imaging gives us the ability to noninvasively view tissues and organs that are hidden within the body. It plays a critical role in the detection and diagnosis of diseases and injuries, lets us monitor progression or recovery, and even allows for prenatal screening. There are many different medical imaging modalities, and each has its own specific strengths and weaknesses.

Diffusion magnetic resonance imaging (dMRI) is a specialized imaging technique that is sensitive to the motion of water molecules in tissue, which is affected by interactions with obstacles such as membranes and macromolecules. dMRI takes advantage of the relationship between water diffusion and tissue properties to reveal details about tissue architecture on a microscopic level. Microscopic fractional anisotropy (μ FA) is a dMRI metric that quantifies the asymmetry of water diffusivity across different directions. For example, consider a typical neuron which has a long axon projecting from its cell body. Intracellular diffusivity is greater along the axon's length than in the directions perpendicular to it because of restricting membranes; thus, diffusion in the neuron is highly anisotropic. Disease or injury can alter the neuron's shape and properties, reducing anisotropy, and thus μ FA may potentially serve as a surrogate biomarker of injury or disease in neuroimaging.

The primary goal of this Thesis was to assess the clinical viability of μ FA by developing a rapid protocol for full brain μ FA imaging and then applying it to the study of a neurological disease. **Chapter 1** presents the motivation behind this Thesis and a detailed summary of general background information that supports the subsequent chapters. **Chapter 2** focuses on the development and optimization of a μ FA imaging protocol, and **Chapter 3** focuses on a modification to the technique that may improve its specificity to disease or injury in regions of the brain that are adjacent to cerebrospinal fluid-containing ventricles. The work described in **Chapter 4** explores the sensitivity of μ FA to hippocampal abnormalities in

patients with temporal lobe epilepsy. Finally, **Chapter 5** summarizes the contributions of this Thesis and provides suggestions for future studies.

Co-Authorship Statement

I, Nico Arezza, attest that I am the principal contributor to this Thesis and the work presented herein. Below are the full author lists for Chapters 2-4 and descriptions of their contributions.

Chapter 2 and Appendix A

Full Author List: **Nico Arezza**, Desmond Tse, Corey Baron

Contributions:

NA – conceptualization, methodology, experiments, writing

DT – MRI sequence design and testing

CB – conceptualization, methodology, review, supervision

Chapter 3

Full Author List: **Nico Arezza**, Tales Santini, Mohammad Omer, Corey Baron

Contributions:

NA – conceptualization, methodology, experiments, writing

TS – methodology, experiments, review

MO – preliminary experiments

CB – conceptualization, methodology, review, supervision

Chapter 4

Full Author List: **Nico Arezza**, Hana Abbas, Caroline Chadwick, Ingrid Johnsrude, Jorge Burneo, Ali Khan, Corey Baron

Contributions:

NA – methodology, data analysis, writing

HA – data collection, review

CC – data collection, review

IJ – data collection, review

JB – clinical, data collection, review

AK – methodology, software, data collection, review

CB – methodology, software, data collection, data analysis, review, supervision

Acknowledgments

This work was funded by the Western Graduate Research Stipend (WGRS), the Ontario Graduate Scholarship (OGS) program, the Queen Elizabeth II Graduate Scholarship in Science and Technology (QEII-GSST) Program, and the Natural Sciences and Engineering Research Council of Canada (NSERC).

First and foremost, I'd like to thank my primary supervisor, Dr. Corey Baron, whose insightful guidance and dedication have been driving forces behind my success. Your support was crucial in helping me get through the pandemic and the other obstacles that sprang up and I have learned so much from you over the past few years. Thank you for accepting me as your inaugural PhD student, taking a leap of faith in the process.

I'd like to thank my secondary supervisor, Dr. Ravi Menon, and my advisory committee, Dr. Rob Bartha and Dr. Jean Théberge. Each of you has challenged me to think critically and I thank you for your guidance and insight. I would also like to thank all the collaborators I've had the pleasure of working with, with a special thanks to Dr. Ali Khan and Dr. Tales Santini.

To all the staff in the Medical Biophysics department and at Robarts Research Institute, none of this would have been possible if not for you. Thank you for everything you've done for me.

It has been great to work with all the other students in the Baron Lab and at Robarts. I really enjoyed the little community we had on the first floor of Robarts and always left work in a great mood. It has truly been a pleasure to work alongside you. Thank you for making my time at Western so enjoyable, and a special thanks goes out to everyone who volunteered to go in the scanner!

I can't accept this doctorate without acknowledging some of my previous mentors. Thank you, Dr. Michael Kolios, for everything you've taught me. Thank you, Dr. Kristin Vickers, for sparking my interest in the brain and nervous system. Thank you to all the teachers and instructors who dealt with me throughout my studies!

Finally, I'd like to thank my family. Thank you, mom and dad, for supporting me every step of the way, for giving me encouragement, and for always having an open door. You never stopped believing in me. Thank you, Kirsten, for being there for me, for patiently listening to me ramble about my work, and for always being willing to help me with a figure or a presentation. I couldn't do it without you. And of course, thank you, Kida. Nothing is better than coming home and being greeted by you and your little wagging tail!

Dedication

This work is dedicated to Franca Vecchiarelli.

Rest in peace, Nonna.

Table of Contents

Abstract.....	ii
Summary for Lay Audience.....	iv
Co-Authorship Statement.....	vi
Acknowledgments.....	viii
Table of Contents.....	xi
List of Tables.....	xiv
List of Figures.....	xv
List of Acronyms and Abbreviations.....	xxvi
Chapter 1	1
1 Introduction.....	1
1.1. Overview.....	1
1.2. Scope of Thesis.....	2
1.3. Cell Types and Microstructure.....	4
1.3.1. Macrostructure.....	9
1.3.2. Pathological Changes in the Brain.....	10
1.4. Temporal Lobe Epilepsy.....	13
1.4.1. Hippocampus Physiology.....	14
1.5. Magnetic Resonance Imaging.....	16
1.5.1. Nuclear Magnetic Resonance.....	16
1.5.2. Signal Acquisition.....	18
1.5.3. Imaging Considerations.....	21
1.5.4. Echo Planar Imaging.....	23
1.6. Diffusion-weighted MRI.....	24
1.6.1. Physics of Diffusion.....	24
1.6.2. Diffusion and the MRI Signal.....	28
1.6.3. Diffusion Tensor Imaging.....	30
1.6.4. Advanced Diffusion Imaging.....	38
Chapter 2	44
2 Rapid Microscopic Fractional Anisotropy Imaging via an Optimized Linear Regression Formulation.....	44
2.1. Overview.....	44
2.2. Introduction.....	44
2.3. Theory.....	49
2.3.1. μ FA Estimation.....	49
2.3.2. Diffusion Coefficient Estimation Using the Powder Average Diffusion Kurtosis Signal Representation.....	50
2.3.3. μ A Optimization.....	51
2.4. Methods.....	52
2.4.1. Sequence Optimization.....	54
2.4.2. Comprehensive Acquisitions.....	56
2.4.3. Analysis.....	58
2.5. Results.....	59
2.5.1. Sequence Optimization.....	59
2.5.2. Comparison Between Different μ FA Techniques.....	63
2.5.3. Analysis of Repeatability.....	66

2.5.4. Minimalistic Sequence.....	67
2.6. Discussion.....	68
2.7. Conclusions.....	72
Chapter 3	74
3 Estimation of Free Water-Corrected Microscopic Fractional Anisotropy.....	74
3.1. Overview.....	74
3.2. Introduction.....	74
3.3. Materials and Methods.....	79
3.3.1. Fitting Algorithm.....	80
3.3.2. Synthetic dMRI Simulations.....	82
3.3.3. Monte Carlo Simulations.....	84
3.3.4. In Vivo.....	85
3.4. Results.....	87
3.4.1. Synthetic dMRI Simulations.....	87
3.4.2. Monte Carlo Simulations.....	89
3.4.3. In Vivo.....	90
3.5. Discussion.....	94
Chapter 4	103
4 Microscopic Fractional Anisotropy Asymmetry in Unilateral Temporal Lobe Epilepsy.....	103
4.1. Overview.....	103
4.2. Introduction.....	103
4.3. Methods.....	105
4.3.1. Participants.....	105
4.3.2. MRI Acquisition and Processing.....	106
4.3.3. Hippocampus Segmentation.....	107
4.3.4. Estimation of dMRI Parameters.....	108
4.3.5. Statistical Analysis.....	109
4.4. Results.....	110
4.5. Discussion.....	116
4.5.1. Confirmed MTS vs. MR-Negative TLE.....	117
4.5.2. Microscopic Fractional Anisotropy vs. Fractional Anisotropy.....	118
4.5.3. Limitations.....	119
4.6. Conclusions.....	120
Chapter 5	121
5 Conclusions.....	121
5.1. Limitations and Suggestions.....	122
5.1.1. Diffusion Time-Dependence.....	122
5.1.2. Sample Size and Demographics.....	124
5.1.3. k-space Trajectory.....	125
5.1.4. Microscopic Kurtosis.....	125
5.1.5. Protocol Optimized for White Matter.....	126
5.1.6. Fitting Errors in the Free Water Elimination Algorithm.....	127
5.1.7. Why no FWE in the TLE study?.....	127
5.2. Future Work.....	128
Appendices.....	130
References.....	144

Curriculum Vitae 157

List of Tables

Table 1-1: Spatial resolution and depth penetration of the major clinical imaging modalities. Adapted from [2] and modified.	2
Table 2-1: Summary of MRI sequences and data subsets for in vivo acquisitions.	53
Table 4-1: Clinical characteristics of patients with left and right temporal lobe epilepsy. ..	106
Table 5-1. Example diffusion MRI data in which the LTE and STE waveforms probe different diffusion times, resulting in different apparent diffusivities. When a joint fit to the powder average diffusion kurtosis representation is performed, the resulting μ FA estimate is biased.	123

List of Figures

Figure 1-1. The structure of a typical neuron. The cell body, or soma, is the genetic and metabolic center of the cell and gives rise to dendrites, which receive chemical information from other neurons or from sensory receptors, and the axon, which transmits electrical signals to the synapses. Image was drawn and water painted by Kirsten Cardinell and full permission was granted for its use in this work. 6

Figure 1-2. Oligodendrocytes form the myelin sheaths in the brain. Image was drawn and water painted by Kirsten Cardinell and full permission was granted for its use in this work. 8

Figure 1-3. T₁-weighted MRI slice depicting clearly delineable gray matter (GM), white matter (WM), and cerebrospinal fluid (CSF) regions. In this contrast scheme, CSF appears black, WM is a bright gray, and GM is a darker gray. Note that the extra-cranial space, while also black, does not represent CSF. This image was acquired with appropriate Research and Ethics Board approval..... 9

Figure 1-4. Examples of neuronal abnormalities that can result from injury or disease. Images were drawn and water painted by Kirsten Cardinell and full permission was granted for their use in this work. 12

Figure 1-5. An isolated dentate gyrus granular neuron (left) and cornu ammonis 1 pyramidal neuron (right). The scale bar represents 50 μm . Image adapted from “Cranial Irradiation Alters Dendritic Spine Density and Morphology in the Hippocampus”, Chakraborti A. *et al*, *PLoS ONE*, 2012..... 15

Figure 1-6. The precession frequency as a function of the position along the z-axis in the presence of a static gradient. The frequency bandwidth (shaded) determines the thickness of the excited slice. Image adapted from *Magnetic Resonance Imaging: Physical Principles and*

Sequence Design 2nd ed, Brown, R.W. *et al*, 2014 and modified to maintain consistency with the symbols and terminology used in this work..... 20

Figure 1-7. Simplified pulse sequence diagram for a diffusion-weighted echo planar imaging (EPI) acquisition. All waveforms are depicted as a function of time. Top: The slice selection gradient (blue, (a)) limits excitation from the initial 90° radiofrequency (RF) pulse to a single slice in the z-direction. On either side of the inverting 180° RF pulse are dephasing and rephasing diffusion-sensitizing gradients (green, (b)). The gradients applied during readout manipulate the k-space trajectory: each rectangular gradient in the x-direction (orange, (c)) moves the k-space sampling trajectory through a line in the **k_x** direction, while each “blip” gradient in the y-direction (yellow, (d)) shifts the sampling trajectory to a new line in **k_y**. The spoiler gradients at the end of the sequence (gray, (e)) remove any remaining transverse magnetization. Bottom: During readout, alternating lines of k-space are sampled in reverse directions..... 24

Figure 1-8. Probability distributions for the location of a particle experiencing Gaussian diffusion in the x-direction. Depicted curves were generated using a diffusion coefficient of **3.0 * 10⁻³ mm²/s**. 26

Figure 1-9. (a) Potential trajectories of water molecules experiencing restricted diffusion (red), hindered diffusion (blue), and free diffusion (green) along the x-direction. The circles represent cross-sections of neuronal axons with impermeable membranes. (b) Mean squared displacement of molecules along the x-direction (**x²**) as a function of diffusion time. The asymptotic dotted line depicts the maximum **x²** of molecules undergoing restricted diffusion, resulting from the finite size of the impermeable axons..... 27

Figure 1-10. A conventional “Stejskal-Tanner” pulsed gradient spin echo sequence with rectangular gradients. The initial 90° radiofrequency (rf) pulse excites the slice of the sample

that has a Larmor frequency matching the pulse frequency, which is determined by the slice selection gradient (G_{SS}). After a time, a 180° rf pulse is applied to invert the magnetization vectors, leading to the production of an echo. The diffusion-encoding gradients (shaded gray) are applied on either side of the second rf pulse to dephase and then rephase the individual spins. Note that the diffusion gradients are each applied for a duration of δ , are separated by a time of Δ (start to start), and have a gradient strength of G . Not depicted in this image are the gradients used to manipulate the k-space trajectory (G_x and G_y). Image adapted from *Magnetic Resonance Imaging: Physical Principles and Sequence Design 2nd ed*, Brown, R.W. et al, 2014..... 29

Figure 1-11. An ellipsoid depicting the eigenvalue/eigenvector pairs corresponding to the diffusion of water within a voxel. The black arrows portray the directions of the eigenvectors, while the eigenvalues (red) quantify the average diffusivity along those directions. In this example, the principal eigenvalue (λ_1) is greater than the other eigenvalues, implying that diffusion within this voxel is anisotropic and that diffusivity is greatest along v_1 . In a voxel with isotropic diffusion, the ellipsoid would instead resemble a sphere with $\lambda_1 = \lambda_2 = \lambda_3$ 31

Figure 1-12. Examples of mean diffusivity (MD), fractional anisotropy (FA), axial diffusivity, and radial diffusivity maps from a patient with epilepsy, all normalized to pixel intensities ranging from 0 to 1. This image was acquired with appropriate Research and Ethics Board approval..... 33

Figure 1-13. Logarithm of a typical diffusion MRI signal (S) from a tissue-containing voxel sampled at seven b-values. The low b-value signal fitted to the DTI signal representation (black), which assumes Gaussian diffusion within the voxel, resembles a straight line, while

the measured signal (red) deviates from this representation at higher b-values. Plot generated using simulated data..... 36

Figure 1-14. The effects of various tissue geometries on fractional anisotropy (FA). The cylinders can be said to approximate neuronal axons, while the spheres can represent non-neuronal, spherical cells. Though columns 1-3 all depict intact axons, the decreasing orientational coherence from left to right leads to decreasing values of FA. This confounding effect of axon orientation limits the specificity of FA to white matter neurodegeneration. The diffusion tensor signal representation cannot distinguish between incoherently arranged axons (column 3) and spherical cells (column 4), as diffusion appears isotropic in both cases. Image adapted from “Microanisotropy imaging: quantification of microscopic diffusion anisotropy and orientational order parameter by diffusion MRI with magic-angle spinning of the q-vector”, Lasic S. *et al*, *Frontiers in Physics*, 2014. 37

Figure 1-15. Diffusion tensor imaging (DTI) and diffusion kurtosis imaging (DKI) signal representations fitted to MRI signal (S) from a tissue-containing voxel sampled at seven b-values. By characterizing the variance of diffusivities, or kurtosis, the DKI representation (blue) better fits the acquired data (red) than the DTI representation (black). Plot generated using simulated data..... 39

Figure 1-16. The effects of various tissue geometries on both fractional anisotropy (FA) and microscopic fractional anisotropy (μ FA). The cylinders can be said to approximate neuronal axons, while the spheres can represent non-neuronal, spherical cells. FA and μ FA are equivalent in voxels containing coherently aligned axons (column 1) and voxels containing only spherical cells (column 4), but when voxels contain crossing axons, as in columns 2-3, μ FA correctly detects anisotropic diffusion whereas FA reports reduced anisotropy due to the confounding effects of fiber orientation. Image retrieved from “Microanisotropy imaging:

quantification of microscopic diffusion anisotropy and orientational order parameter by diffusion MRI with magic-angle spinning of the q-vector”, Lasic S. *et al*, *Frontiers in Physics*, 2014..... 41

Figure 2-1. Schematic representation of the spherical tensor encoding gradient waveforms. Diffusion encoding blocks have been inserted on both sides of a 180° pulse in all three gradient directions to acquire an STE diffusion MRI signal. Implicit gradient reversal due to the 180° pulse has been applied. 55

Figure 2-2. Logarithm of the diffusion MRI signal vs. b-value in frontal white matter. The plot shows the powder-averaged signal from a manually prescribed region of interest across four volunteers as measured with linear tensor encoding and spherical tensor encoding (black and blue circles, respectively), while the dashed lines show the third order cumulant fit. Also depicted are the standard deviations across the volunteers..... 60

Figure 2-3. Simulated μA^2 SNR in white matter as a function of the b-value and the ratio of STE to LTE acquisitions (n_{STE}/n_{LTE}). Though the maximum SNR occurred when $b = 2000$ s/mm^2 and $n_{STE}/n_{LTE} = 1.7$ (marked by an ‘X’), a wide range of parameters yielded SNRs greater than 95% of the maximum SNR, suggesting that there is flexibility in parameter choice when designing a protocol. Notably, a significant drop off in SNR occurred for $n_{STE}/n_{LTE} < 1$, suggesting that image quality is maximized when the number of STE acquisitions is greater than or equal to the number of LTE acquisitions..... 61

Figure 2-4. Example μA^2 images acquired with the standard (left) and suboptimal (right) subsets of the data without denoising. Lower image quality is observed in the right case, with some irregular features highlighted by the yellow circles. Images were acquired with rate 2 in-plane parallel imaging combined with rate 2 simultaneous multislice. 62

Figure 2-5. Example μ FA images from one volunteer. Images were acquired using the gamma signal representation with the standard subset (left), joint linear regression with the standard subset (center), and simplified linear regression (i.e., D computed from DTI using only b-values of 100 and 1000 s/mm²) (right). Comparable image quality is observed for the three methods. Images were acquired with rate 2 in-plane parallel imaging combined with rate 2 simultaneous multislice..... 64

Figure 2-6. Voxelwise correlations between μ FA estimates acquired using different techniques in white matter (left) and Bland-Altman plots depicting biases between the methods in white matter (right): (a) μ FA_{gamma} vs. μ FA_{joint}, (b) μ FA_{gamma} vs. μ FA_{simp}, and (c) μ FA_{joint} vs. μ FA_{simp}. The dashed red line and solid black line in each of the scatter plots represent the identity and regression lines, respectively. The solid black line in the Bland-Altman plots represents the mean bias, and the dashed grey lines represent the ± 1.96 standard deviation lines. 65

Figure 2-7. Bland-Altman plots assessing the test-retest reliability of μ FA estimates acquired using different techniques in white matter. The solid black line represents the mean bias, and the dashed grey lines represent the ± 1.96 standard deviation lines. 66

Figure 2-8. Example μ FA, μA^2 , and LTE and STE variance maps acquired using equation 2.2 in a subsampled data set: The acquisition comprised of 16 LTE directions at $b = 2000$ s/mm² and 3, 6, and 18 STE directions at $b = 100, 1000, \text{ and } 2000$ s/mm², respectively. This direction scheme corresponds to a total scan time of approximately 3.3 min with 220 mm x 220 mm x 96 mm coverage at an isotropic 2 mm resolution. All images were normalized to a maximum pixel value of 1. Images were acquired with rate 2 in-plane parallel imaging combined with rate 2 simultaneous multislice..... 67

Figure 3-1. Free water partial volume effects at the interface between brain tissue and a ventricle containing cerebrospinal fluid (CSF). The image on the right depicts an ideal slice in

which the brain tissue and CSF are clearly delineated, while the center image depicts partial volume effects in voxels that contain both CSF and tissue, highlighted by yellow arrows. The goal of the proposed algorithm is to obtain parameter estimates specific to the tissue in these voxels. 77

Figure 3-2. Relative error in diffusion MRI indices measured in synthetic white matter (WM) and gray matter (GM) voxels at various SNR levels and a free water diffusivity of $3e - 3mm^2/s$. The x-axis depicts the simulated volume fraction (*fsim*), while the ground truth value for each metric is denoted as GT. The red line with crosses indicates the mean measurements made using the conventional (Conv) method at SNR=20, the black line with circles depicts the FWE method at SNR=20, the green line with inverted triangles depicts the FWE method at SNR=10, and the blue line with triangles depicts the FWE method at SNR=40. 88

Figure 3-3. Relative error in diffusion MRI indices measured in synthetic white matter (WM) and gray matter (GM) voxels with various free water diffusivities (*DCSF*) and an SNR of 20. The x-axis depicts the simulated volume fraction (*fsim*), while the ground truth value for each metric is denoted as GT. The red line with crosses indicates the mean measurements made using the conventional (Conv) method with $DCSF = 3e - 3mm^2/s$, the black line with circles depicts the FWE method with $DCSF = 3e - 3mm^2/s$, the purple line with inverted triangles depicts the FWE method with $DCSF = 2.85e - 3mm^2/s$, and the teal line with triangles depicts the FWE method with $DCSF = 3.15e - 3mm^2/s$ 89

Figure 3-4. Relative error in diffusion MRI indices measured using the conventional (Conv) and FWE methods on signals simulated using a Monte Carlo technique. The geometry consisted of infinitely long cylinders with a 1 μm radius and 0.7 intra-tube fraction. The x-axis depicts the simulated volume fraction (*fsim*), while the ground truth value for each metric is

denoted as GT. The red line with crosses indicates the measurements made using the conventional (Conv) method while the black line with circles indicates measurements made using the FWE method..... 90

Figure 3-5. (a) Example slices of tissue diffusivity (***DT***), anisotropic kurtosis (***Kaniso***), isotropic kurtosis (***Kiso***), microscopic fractional anisotropy (μ FA), and fluid volume fraction ($1-f$) measured in one of the healthy volunteers. The images on the left were computed using the free water elimination (FWE) method while those on the right were computed using the conventional (Conv) method. Note that ***DT*** is used interchangeably with ***D*** for the conventional method. (b) Sample slice depicting a binary map showing voxels with tissue volume fractions less than 0.25, which were omitted in region-of-interest analyses. 92

Figure 3-6. Example cerebral cortex images of tissue diffusivity (***DT***), anisotropic kurtosis (***Kaniso***), isotropic kurtosis (***Kiso***), microscopic fractional anisotropy (μ FA), and tissue volume fraction (f) measured in one of the healthy volunteers. The images on the left were computed using the free water elimination (FWE) method while those on the right were computed using the conventional (Conv) method. Note that ***DT*** is used interchangeably with ***D*** for the conventional method. The yellow arrow highlights a region in which a significant difference is observed between the FWE and conventional μ FA measurements due to high free water contamination..... 93

Figure 3-7. Comparison between the conventional (Conv) and free water elimination (FWE) methods in four healthy volunteers. Depicted on the left is a coronal T₁-weighted MPRAGE slice from one of the volunteers highlighting the five regions-of-interest (ROIs). Note that volumetric ROIs were used, despite the single slice depiction. On the right are plots comparing the mean diffusivity (***DT***), microscopic fractional anisotropy (μ FA), isotropic kurtosis (***Kiso***), and anisotropic kurtosis (***Kaniso***) produced by the Conv and FWE methods. In all ROIs, ***DT***

and *Kiso* were reduced when FWE was applied, while μ FA and *Kaniso* were elevated, though the magnitude of this difference varied by region. Note that *DT* is used interchangeably with *D* for the conventional method. 94

Figure 4-1. Sagittal and coronal T₁-weighted (top) and T₂-weighted (bottom) MR images from a healthy volunteer with insets highlighting the four hippocampal subregions used in this study: the subiculum (SB), cornu ammonis 1 (CA1), cornu ammonis 2 and 3 (CA2/3) and cornu ammonis 4 plus dentate gyrus (CA4/DG). Note that only the right hippocampus is labeled although both hippocampi were analyzed..... 111

Figure 4-2. (a) Example T₁-weighted coronal image from a TLE patient with confirmed MTS, with the four hippocampal subregions highlighted. (b) MD, FA, and μ FA coronal slices from the same patient before registration to T₁-space (left), and after registration to T₁-space and interpolation (right) depicting the ipsilateral and contralateral hippocampal regions. Note that for this patient, the left side (L) is the ipsilateral side and the right side (R) is the contralateral side. 112

Figure 4-3. Volume (normalized against the mean contralateral volume), MD, FA, and μ FA measurements in the ipsilateral and contralateral sides of each of the four hippocampal subregions across 9 TLE patients, plus mean measurements of both hemispheres across 9 healthy control volunteers (HC). The horizontal black lines depict the mean measurement across the cohort, and the gray ovals highlight a region spanning two standard deviations above and below the mean. The two plots with pink ovals highlight significant MD (p=0.012) and μ FA (p<0.01) asymmetries in the TLE cohort..... 113

Figure 4-4. Percentage difference (% Δ) between ipsilateral and contralateral measurements of volume, MD, FA, and μ FA in the full hippocampus (top) and CA4/DG region (bottom) in

unilateral TLE patients, and $\% \Delta$ between left and right measurements in 9 healthy control volunteers (HC).....	115
Figure B-0-1. Data acquisition and post-processing pipeline for the diffusion MRI data used in this work. For Chapter 2, <i>eddy_correct</i> was used to correct eddy current artifacts, while in Chapter 3 and Chapter 4, <i>topup</i> and <i>eddy</i> were used instead.....	132
Figure B-0-2. Example k-space signal magnitude [A.U.] for a single diffusion-weighted MRI slice. The blue dotted outline highlights the region that would be asymmetrically sampled if 6/8 partial Fourier is used, while the yellow dashed outline highlights the symmetrically sampled region. Data below the yellow dashed region would be estimated by assuming conjugate symmetry with the blue dotted region while simultaneously incorporating phase error corrections derived from the yellow dashed region.	134
Figure B-0-3: Eigenvalue (λ) spectrum of simulated dMRI data with the Marchenko-Pastur distribution superimposed. Image adapted from “Diffusion MRI noise mapping using random matrix theory”, Veraart, J. <i>et al</i> , <i>Magnetic Resonance in Medicine</i> , 2015, with permission from John Wiley and Sons (see Appendix C).	136
Figure B-0-4. A truncated k-space is shown on the left, with the white square representing the sampled region and the black outer region representing unsampled higher spatial frequencies. When the 2D Fourier transform is applied to this data, the result in image space (on the right) is a 2D sine cardinal (or <i>sinc</i>) function.	137
Figure B-0-5. Plot of pixel intensities of a 1D image with a single edge. The black line depicts the true image, while the red line depicts the image after convolution with a <i>sinc</i> function, the result of truncation in k-space. The blue dots depict the pixels sampled to create a discrete image. In (a), the image is sampled at suboptimal positions, capturing the signal fluctuations introduced by truncation in k-space. In (b), the image is repositioned so that it is sampled only	

at zero crossings, minimizing the ringing artifacts at the image edge. Image adapted from “Gibbs-ringing artifact removal based on local subvoxel shifts”, Kellner, E. *et al*, *Magnetic Resonance in Medicine*, 2015, with permission from John Wiley and Sons (see Appendix C).

..... 138

List of Acronyms and Abbreviations

<i>μA</i>	Microscopic anisotropy
<i>μFA</i>	Microscopic fractional anisotropy
<i>ADC</i>	Apparent diffusion coefficient
<i>BW</i>	Bandwidth
<i>CA</i>	Cornu ammonis
<i>CoV</i>	Coefficient of variance
<i>CSF</i>	Cerebrospinal fluid
<i>CTI</i>	Correlation tensor imaging
<i>D</i>	Apparent mean diffusivity
<i>DDE</i>	Double diffusion encoding
<i>DG</i>	Dentate gyrus <i>or</i> gyrus dentatus
<i>DKI</i>	Diffusion kurtosis imaging
<i>dMRI</i>	Diffusion-weighted magnetic resonance imaging
<i>DTI</i>	Diffusion tensor imaging
<i>EEG</i>	Electroencephalogram
<i>EPI</i>	Echo planar imaging
<i>f</i>	Tissue volume fraction
<i>FA</i>	Fractional anisotropy
<i>FOV</i>	Field-of-view
<i>FWE</i>	Free water elimination
<i>GM</i>	Grey matter

<i>HS</i>	Hippocampal sclerosis
<i>ILAE</i>	International League Against Epilepsy
<i>K</i>	Apparent kurtosis
<i>LTE</i>	Linear tensor encoding
<i>MD</i>	Mean diffusivity
<i>MRI</i>	Magnetic resonance imaging
<i>MS</i>	Multiple sclerosis
<i>MTS</i>	Mesial temporal sclerosis
<i>NMR</i>	Nuclear magnetic resonance
<i>paD</i>	Powder average diffusion
<i>paK</i>	Powder average kurtosis
<i>PC</i>	Principal component
<i>PCA</i>	Principal component analysis
<i>PET</i>	Positron emission tomography
<i>PGSE</i>	Pulsed gradient spin echo
<i>RF</i>	Radiofrequency
<i>ROI</i>	Region-of-interest
<i>SB</i>	Subiculum
<i>SDE</i>	Single diffusion encoding
<i>SMT</i>	Spherical mean technique
<i>SNR</i>	Signal-to-noise ratio
<i>STE</i>	Spherical tensor encoding
<i>TE</i>	Echo time

<i>TLE</i>	Temporal lobe epilepsy
<i>TR</i>	Repetition time
<i>WM</i>	White matter

Chapter 1

1 Introduction

1.1. Overview

Medical imaging provides a window into the interior of the body and plays a critical role in diagnosing disease and injury, planning treatments and surgeries, and monitoring progression or recovery over time. Though numerous imaging modalities have been developed, the most used techniques in clinical settings (in no particular order) are magnetic resonance imaging (MRI), x-ray imaging, nuclear medicine, ultrasound, and optical imaging. These modalities have different spatial resolution and depth penetration properties, as depicted in Table 1, and different methods from which image contrast is acquired. Among these techniques, MRI is unique in that it's capable of imaging at any depth in the body without the use of potentially harmful ionizing radiation, it provides high soft-tissue contrast, and its contrast mechanism can be customized. However, the tradeoff for these traits is a low signal which often necessitates the use of long scan times and, for some specialized applications, poor imaging resolution. Furthermore, due to the powerful magnets used in MRI, electronics and other objects such as cardiac pacemakers and internal insulin pumps, are contraindicated.

The versatility of MRI as an imaging instrument comes from its ability to target different contrast mechanisms via the use of unique pulse sequences and acquisition protocols. Some examples of contrast targets are magnetization relaxation rates, blood oxygen level, and the diffusion of water. Diffusion-weighted MRI (dMRI) sensitizes the MRI signal to the net movement of water molecules, which reflects the interactions that water molecules have with obstacles such as membranes, fibers, and macromolecules; thus,

diffusion contrast provides information about tissue microstructure by probing these boundaries. dMRI has primarily found use in brain imaging because neural tissue is highly organized and intracellular diffusion within neuronal axons is highly restricted, and because the brain is reasonably static, making it an imaging target that is less prone to deleterious motion artifacts [1].

Table 1-1: Spatial resolution and depth penetration of the major clinical imaging modalities.

Adapted from [2] and modified.

Modality	Spatial Resolution	Depth penetration
MRI	0.25-2 mm	Full body
Computed tomography ¹	0.5-1 mm	Full body
Positron emission tomography ²	5-10 mm	Full body
Single photon emission computed tomography ²	8-10 mm	Full body
Ultrasound	1-2 mm	A few cm
Optical fluorescence imaging ³	2-3 mm	<1 cm
Photoacoustic imaging ³	0.01-1 mm	0.6-3 cm

**Modalities highlighted in gray utilize ionizing radiation.*

¹X-ray imaging, ²Nuclear medicine, ³Optical imaging

1.2. Scope of Thesis

Microscopic fractional anisotropy (μ FA) is a dMRI metric that is sensitized to neuronal microstructure but unaffected by neuron fiber orientation dispersion, potentially giving it high specificity to microstructural abnormalities that can result from disease or injury. However, μ FA imaging protocols generally require prohibitively long scan times due to the use of specialized pulse sequences and other factors. The two primary goals of this thesis were to: (1) develop a protocol at 3T that can map μ FA in the human brain with good repeat measurement reliability and high specificity to disease, within a clinically relevant scan time, and (2) apply the μ FA protocol to the study of disease to assess its sensitivity to neuronal abnormalities. Chapters 2 and 3 involve developing and testing μ FA imaging

protocols, while Chapter 4 describes a preliminary work applying the technique to the study of temporal lobe epilepsy.

Chapter 2 outlines a protocol developed to estimate μ FA, which involves a joint fitting of two types of dMRI signal data (linear tensor encoding, or LTE, and spherical tensor encoding, or STE) to the powder average kurtosis (paK) signal representation. The paK representation is advantageous as it can be computed rapidly using the method of least squares; furthermore, jointly fitting to LTE and STE signal reduces total data (and thus scan time) requirements. When the paK method was compared with another μ FA technique in the white matter of four healthy volunteers, the measurements were found to correlate strongly albeit with a small bias. Additionally, the paK method showed good repeat measurement reliability in white matter.

One of the challenges of measuring μ FA outside of white matter is that gray matter regions tend to contain more free cerebrospinal fluid (CSF). The presence of free CSF in voxels reduces water diffusion anisotropy measurements, potentially confounding with microstructural features that also reduce anisotropy, such as axonal atrophy. In Chapter 3, a signal representation known as free water elimination powder average kurtosis (FWE-paK) was proposed to estimate tissue-specific dMRI indices by separating the tissue signal from the free CSF signal. Simulations revealed that the FWE-paK yielded measurements that were more accurate than measurements made with the paK technique in regions with significant CSF partial volumes. In four healthy volunteers, the FWE method was found to yield higher μ FA measurements than the paK technique in five regions-of-interest, and the difference between measurements correlated with the expected free CSF fraction of each region.

A preliminary study to assess the sensitivity of μ FA (estimated from paK) and other dMRI indices to hippocampal abnormalities in temporal lobe epilepsy (TLE) is described in Chapter 4. μ FA was found to be reduced in the ipsilateral side of the cornu ammonis 4 hippocampal subregion relative to the contralateral side in all nine patients with unilateral temporal lobe epilepsy, while little asymmetry was observed in nine healthy volunteers. No statistically significant asymmetries were observed in the more common fractional anisotropy metric, suggesting that μ FA has greater specificity to relevant disease-related microstructural abnormalities.

The rest of this chapter provides background information regarding brain tissue [3]–[5], MRI [6], [7], diffusion and dMRI [6], [8], and TLE.

1.3. Cell Types and Microstructure

There are two main classes of cells in the nervous system: neurons, or nerve cells, and glia, or glial cells.

The neuron is the functional unit of the nervous system, and it is estimated that there are about 100 billion neurons in the adult human brain, on average. The primary role of neurons is communication, and it is through the complicated architecture of neurons and sensory receptors throughout the central and peripheral nervous systems that functions such as cognition, movement, and sensation are possible. Externally, neurons communicate with each other via chemical signaling, in which specialized molecules known as neurotransmitters are released from one neuron and bind to another. Intraneuronal signals propagate as changes in membrane voltage known as action potentials.

Although vertebrate neurons can vary in shape, size, and complexity, they generally have four specialized and morphologically defined regions known as the cell body, axon, synapses (which are comprised of presynaptic and postsynaptic terminals), and dendrites

(Figure 1-1). The cell body, or soma, is the genetic and metabolic center of the cell and it contains the nucleus and other organelles critical to the neuron's survival and function. In most neurons, a single axon extends out of the cell body, which can then branch out to multiple synapses. The axon is a membrane-covered cylindrical tube that can range from 0.1 mm to 2 m in length and acts as a conductor to propagate action potentials generated at the initial segment, where the axon and soma meet. Additionally, microtubules inside the axon provide a framework for intracellular transport, allowing vesicles containing neurotransmitters to move between the soma and presynaptic terminals. When an action potential reaches a presynaptic terminal, it triggers the release of neurotransmitters, which can bind to receptors on postsynaptic terminals on the dendrites (or other areas) of other neurons. Dendrites are branched extensions of the cell that receive these transmitting molecules and then propagate electrical signals to the cell body. They also act as resistors, isolating the cell from extracellular electrical events. Both dendrites and axons are categorized as neurites because they are projections from the neuronal cell body.

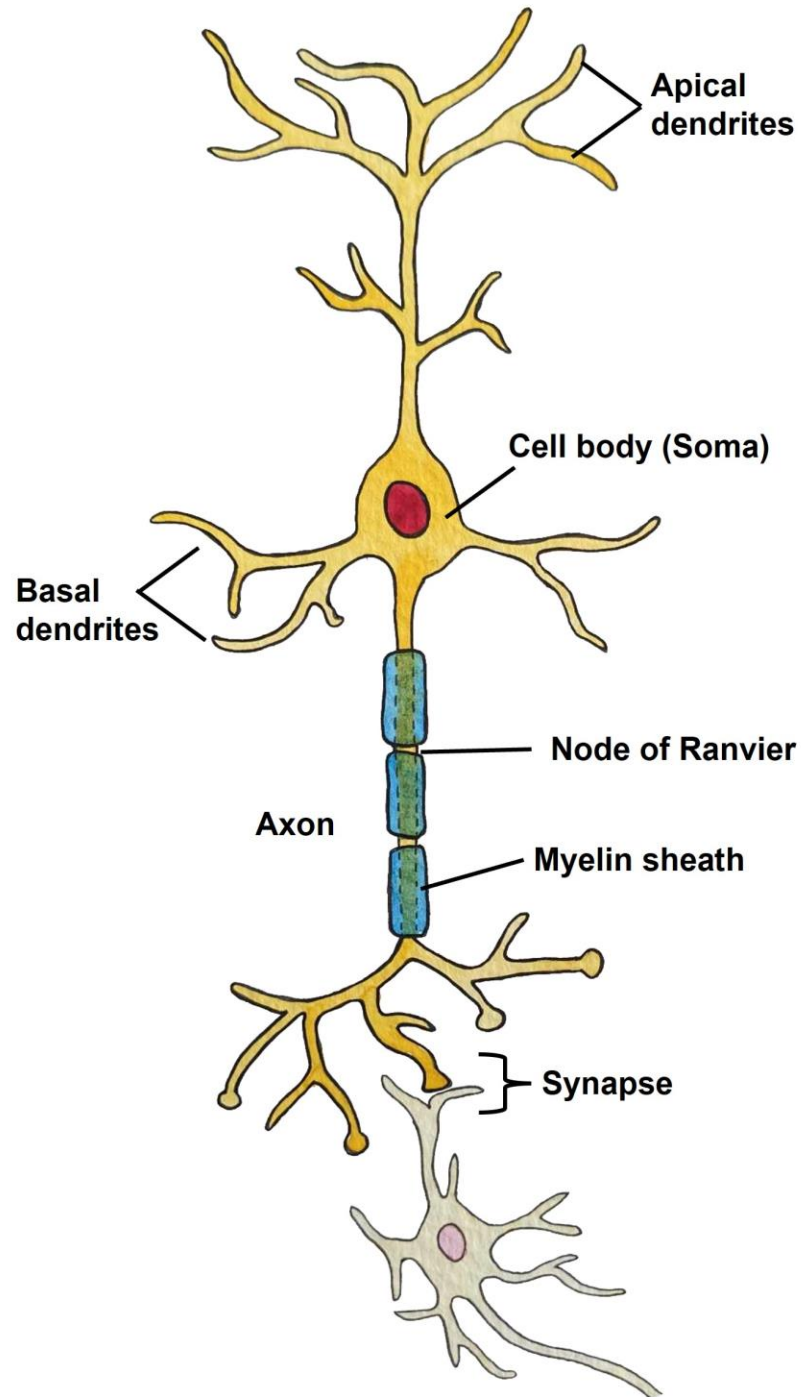


Figure 1-1. The structure of a typical neuron. The cell body, or soma, is the genetic and metabolic center of the cell and gives rise to dendrites, which receive chemical information from other neurons or from sensory receptors, and the axon, which transmits electrical signals to the synapses. Image was drawn and water painted by Kirsten Cardinell and full permission was granted for its use in this work.

Glial cells provide support and protection for neurons. It was previously believed that glia outnumber neurons by a factor of 10:1 in the human brain, but recent technological advances suggest that the ratio may be closer to 1:1 [9], [10]. Though there are many different types of glia, they can be divided into two major classes: microglia and macroglia.

Microglia are immune cells that act as scavengers and protectors in the nervous system, responding to infection, injury, and degenerative disease. They become “activated” in response to various physiological conditions (such as the presence of inflammatory cytokines or necrosis factors) and proceed to destroy invasive microorganisms, remove harmful debris, and promote tissue repair. When activated, microglia proliferate rapidly and undergo several morphological changes to respond to the injury or threat, then later undergo apoptosis to return cell numbers back to baseline [11]. Deteriorated and defective microglia have been detected in disorders such as schizophrenia and Alzheimer’s disease and likely play a significant role in neurodegeneration [12].

Macroglia have a variety of supportive functions and can be further classified into four distinct subtypes called astrocytes, ependymal cells, oligodendrocytes, and Schwann cells. Astrocytes are star-shaped cells that perform a variety of roles including separating neurons for electrical insulation, regulating ion concentrations in the extracellular spaces, and providing nourishment and growth factors, among other functions. Ependymal cells line fluid-filled cavities in the central nervous system and regulate the flow of chemicals between these cavities and the brain. Oligodendrocytes and Schwann cells are small cells that form the myelin sheaths that concentrically wrap around axons; the prior are found in the brain and spine and can each provide a myelin sheath for multiple neurons (Figure 1-2),

while the latter are found in the peripheral nervous system and each envelope a single segment on one axon.

Myelin is a lipid-rich material that acts as an insulator, much like the plastic covering on a standard electrical wire. However, myelin doesn't form a single long sheath that covers the full length of an axon and instead covers it in segments (Figure 1-1). Between each myelinated section is a short gap called a node of Ranvier. The main purpose of myelin is to facilitate a process known as saltatory conduction, which increases the velocity at which action potentials propagate along an axon fiber. In unmyelinated fibers, electrical impulses travel as continuous waves, while in myelinated fibers they “jump” between nodes of Ranvier; this process increases the propagation speed of action potentials by a factor of 15- to 30-fold [13].

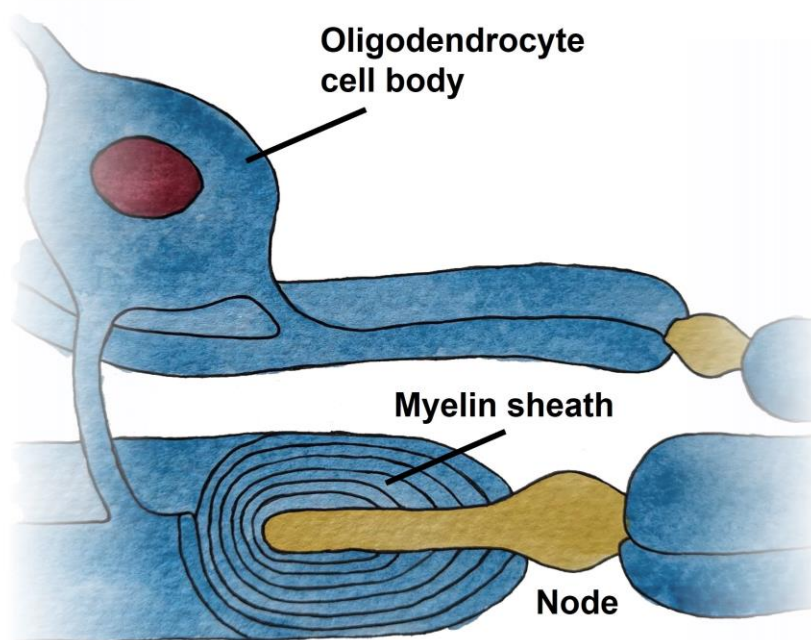


Figure 1-2. Oligodendrocytes form the myelin sheaths in the brain. Image was drawn and water painted by Kirsten Cardinell and full permission was granted for its use in this work.

1.3.1. Macrostructure

The three major macrostructural components of the brain are white matter (WM), gray matter (GM), and cerebrospinal fluid (CSF), as depicted in Figure 1-3. WM is primarily composed of myelinated axon fibers bundled together coherently to form tracts that connect various structures and regions of the brain, facilitating intra- and inter-regional communication. GM is primarily composed of neuronal cell bodies, dendrites, unmyelinated axons, and glial cells and includes most of the regions involved with motor control, cognition, and sensory perception. CSF is a clear, colorless fluid that is produced in cavities known as ventricles and can be found throughout the neurocranium. CSF cushions the brain from mechanical trauma, allows it to maintain its volume rather than collapse in on itself, helps maintain homeostasis by regulating chemical factors, and clears waste products [14].

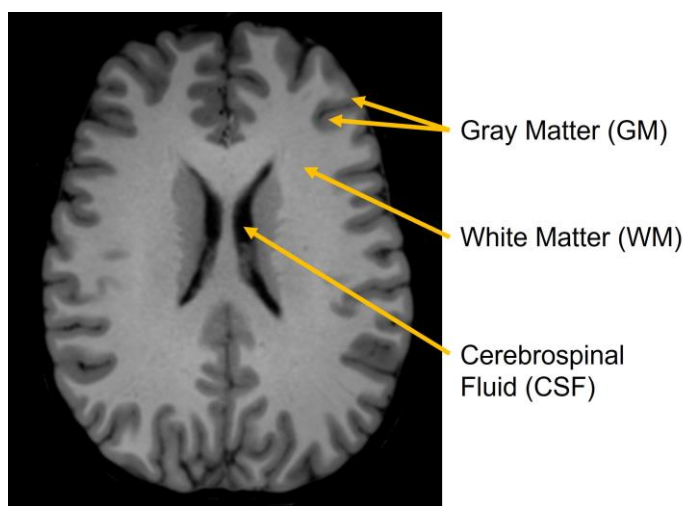


Figure 1-3. T₁-weighted MRI slice depicting clearly delineable gray matter (GM), white matter (WM), and cerebrospinal fluid (CSF) regions. In this contrast scheme, CSF appears black, WM is a bright gray, and GM is a darker gray. Note that the extra-cranial space, while also black, does not represent CSF. This image was acquired with appropriate Research and Ethics Board approval.

In addition to the components listed above, the brain can also be divided into major identifiable zones based on clear anatomical divisions and their unique cognitive and motor functions. Examples include the four main lobes of the brain (frontal, temporal, occipital, and parietal), the cerebellum, and the brain stem. These zones can often be further subdivided into smaller anatomical regions, such as deep GM regions like the hippocampus and its even smaller subfields, and WM tracts like the corpus callosum. Segmenting the brain into these subsections is useful for delineating pathological regions in disease or following injury.

1.3.2. Pathological Changes in the Brain

Neurological diseases and injuries often result in pathological cellular alterations that can affect cognition or motor function and it is these abnormalities that lead to reduced quality-of-life and increased mortality. Examples of microstructural changes are neuronal atrophy and death, demyelination and dysmyelination, changes in neurite shape, and gliosis. While some of these changes are generally irreparable, others can be partially or fully reversed if the necessary repair mechanisms are intact and functional. Some examples of neuronal changes/abnormalities are depicted in Figure 1-4.

Neuronal death respectively refers loss of neurons in the brain which can result in macrostructural deterioration. Many studies have observed age-related declines in GM and WM volume in healthy adults [15]–[17], suggesting that neuronal atrophy and death may be a normal consequence of aging. However, acute tissue loss can occur after traumatic injury [18] or stroke [19], and accelerated decline in brain volume is a hallmark of progressive diseases [20] like amyotrophic lateral sclerosis [21] and Alzheimer’s disease [22]. Decreases in brain tissue volume are generally accompanied by an increase in the volume of fluid in the extracellular space.

Demyelination is the loss of myelin that surrounds axons, and dysmyelination describes a dysfunction in the myelinogenesis process that results in delayed or arrested myelin production or the formation of abnormal myelin sheaths, though the terms are often used interchangeably. Since myelin plays crucial roles in saltatory conduction and insulation, demyelinated axons transmit electrical impulses ineffectively and can be influenced by the electrical activity of neighboring cells. Multiple sclerosis (MS) is the most common demyelinating disease and the most common non-traumatic disabling disease in young adults [23], but demyelination may also play a causal role in seizure generation in patients with focal epilepsies, as the loss of the electrically-insulating myelin coating may promote axonal hyperexcitability [24].

Changes to neurite shape can result from neurodegenerative disorders, stretch injuries and brain trauma [25], stroke [26], or neurotoxins or drugs [27]. The mechanisms behind these changes are not fully understood; the classical explanation is that swelling occurs when ion pumps on the surfaces of neurons are compromised, causing an increased intracellular ion concentration that drives osmosis [28], though some contend this theory [29]. Beading occurs when the fluid within neurites is distributed abnormally as some segments expand while others constrict [25]. Though neurite expansion, constriction, and beading are often reversible and neurites can return to their cylindrical shapes following an insult, irreversible damage and cell death are possible if the magnitude of the osmotic shock or the rate at which the cell expands or constricts is too high [30].

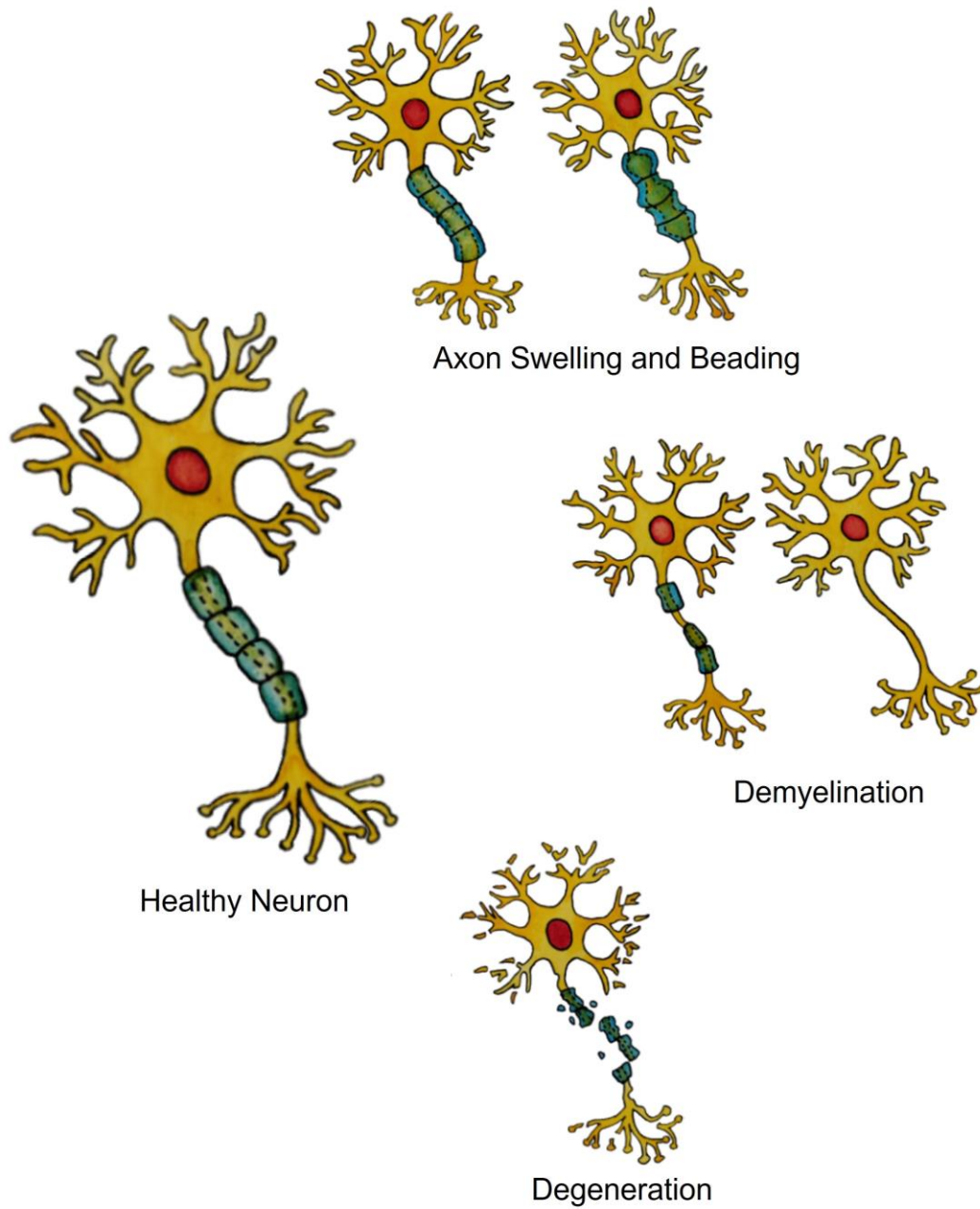


Figure 1-4. Examples of neuronal abnormalities that can result from injury or disease. Images were drawn and water painted by Kirsten Cardinell and full permission was granted for their use in this work.

Gliosis is an umbrella term that describes the non-specific changes that glial cells undergo in response to injury or disease. In most cases, gliosis involves glial cells undergoing hypertrophy and/or proliferation to respond to an injury. Microglial activation (as described in 1.3.2) is a form of gliosis, as are astrogliosis [31] and oligodendrocyte recruitment [32]. Though gliosis plays a protective and regenerative role in the brain, it can also lead to the formation of glial scars that inhibit axon regeneration [31].

1.4. Temporal Lobe Epilepsy

Epilepsy is a brain disorder that affects nearly 1% of people worldwide [33]. It is characterized by recurrent seizures, which are abnormal excessive bouts of electrical activity in the brain that can have significant and potentially life-threatening effects on patients such as temporary involuntary shaking and loss of consciousness [34]. In addition to these seizures, which typically last a few minutes, epilepsy patients are more likely than the general population to suffer from neuropsychiatric disorders like anxiety and depression, pain disorders like migraine and chronic pain, and even certain physical disorders like asthma [35].

For many patients, seizures can often be managed with anticonvulsant medications, though approximately 30% of adults with epilepsy progress to a drug-resistant or medically intractable form of the disease [36]. If the site of seizure onset is confined to one hemisphere of the brain (i.e., unilateral) and can be delineated using medical imaging and/or electroencephalography (EEG), surgery to remove the seizure focus may be a viable treatment option for patients with medically intractable epilepsy.

Temporal lobe epilepsy (TLE) is characterized by seizures that originate in the medial or lateral structures of the temporal lobe, and is one of the most common forms of focal epilepsy in both adults and children [37]. Approximately 70% of adults with

medically intractable TLE present with hippocampal sclerosis (HS) [38], which is defined as severe cell loss and gliosis in the hippocampus, a structure found in the medial temporal lobe. When HS is present in one hemisphere but not the other, a patient with medically intractable disease may be a candidate for surgery to remove the ipsilateral hippocampus (hippocampectomy).

1.4.1. Hippocampus Physiology

The hippocampus (also known as the hippocampal formation) is a bilaminar structure consisting of the cornu ammonis (CA) and the dentate gyrus (DG), folded into one another. The main functional cellular components of the CA are pyramidal neurons, which feature triangular soma with an axon emerging from the base and two distinct dendritic trees: a long branch of apical dendrites that can traverse the entire thickness of the CA emerging from the apex of the soma, and shorter radially-distributed basal dendrites emerging from the base [39]. In the DG, granular neurons are the main functional units, and they feature a monoconical branch of apical dendrites emerging from a small and round soma [39]. Figure 1-5 depicts a granular neuron and a pyramidal neuron. Glia and interneurons are also present in the hippocampus.

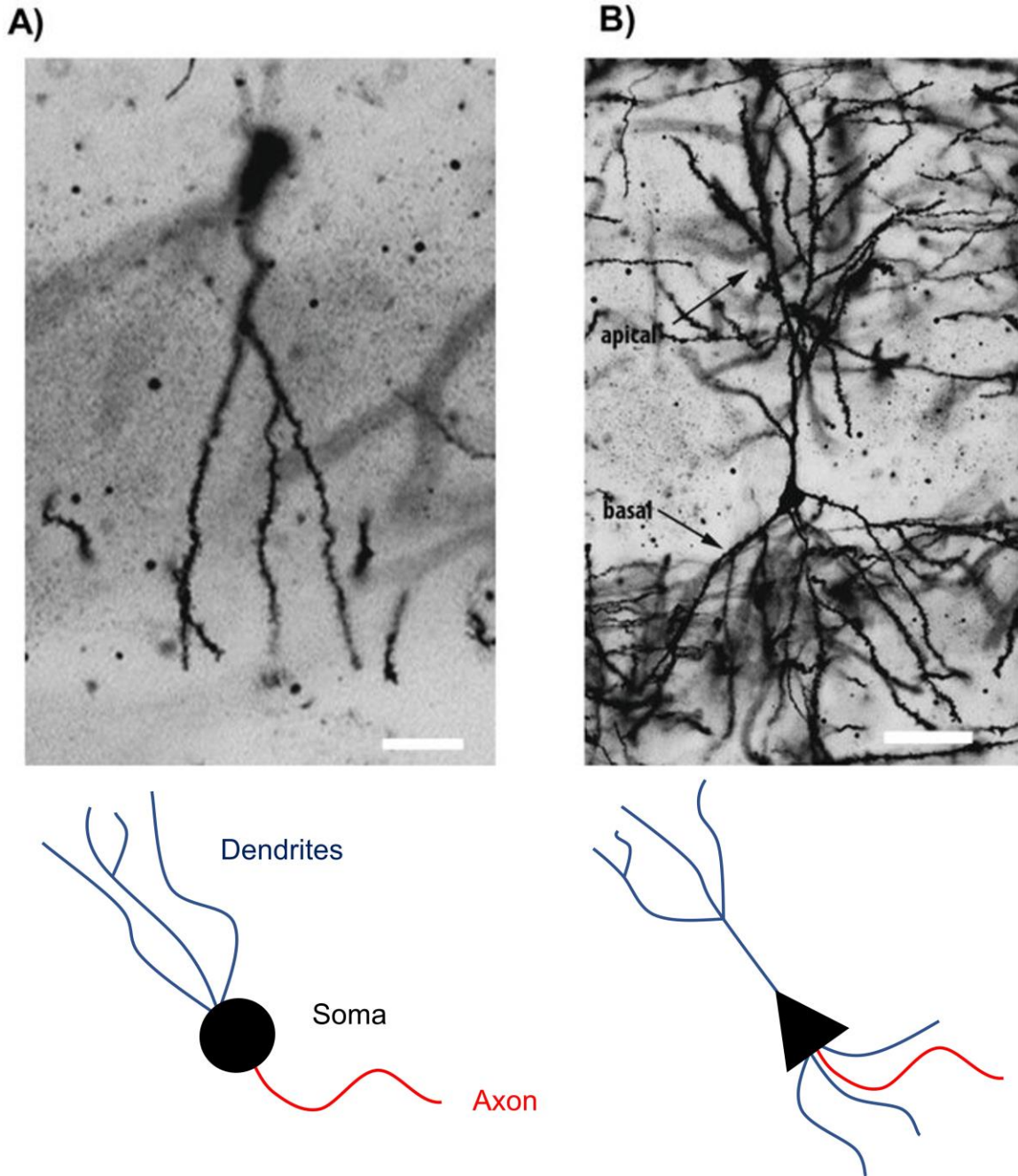


Figure 1-5. An isolated dentate gyrus granular neuron (left) and cornu ammonis 1 pyramidal neuron (right). The scale bar represents 50 μm . Image adapted from “Cranial Irradiation Alters Dendritic Spine Density and Morphology in the Hippocampus”, Chakraborti A. *et al*, *PLoS ONE*, 2012.

Functionally, the hippocampus plays a role in learning and memory, regulation of emotional behavior, and regulation of hormonal secretion [39]. Thus, in addition to seizures, TLE patients with HS may experience other cognitive symptoms such as long-term memory deficits [40].

1.5. Magnetic Resonance Imaging

1.5.1. Nuclear Magnetic Resonance

Any atomic nucleus with an odd number of protons or an odd number of neutrons possesses an intrinsic property known as spin angular momentum. Nuclei with this property can be visualized as spinning charged spheres that possess a nonzero magnetic moment and are often referred to as “spins”. When subjected to an external magnetic field, individual spins have a slight tendency to point along the direction of the field and exhibit precession about that direction in a process known as nuclear magnetic resonance (NMR). For a group of many protons, referred to as a spin isochromat, the net magnetization aligns along the direction of the external magnetic field and can be analyzed according to the laws of classical electromagnetism rather than by those of quantum mechanics.

In MRI, a static magnetic field $\mathbf{B}_0 = B_0 \hat{z}$ is employed to create a static net magnetization in the sample (M_0) along the direction of the unit vector \hat{z} . When time-dependent magnetic fields are applied in addition to the static field, the net magnetic field can be described as:

$$\mathbf{B}(t) = B_x(t)\hat{x} + B_y(t)\hat{y} + (B_0 + B_z(t))\hat{z} \quad (1.1)$$

where t is the time, and \hat{x} and \hat{y} are unit vectors in directions orthogonal to each other and to \hat{z} . The Bloch equation describes the effect of \mathbf{B} on the net magnetization (\mathbf{M}) in the sample and is given by [6], [7]:

$$\frac{d\mathbf{M}}{dt} = \gamma \mathbf{M} \times \mathbf{B} - \frac{M_x \hat{x} + M_y \hat{y}}{T_2} - \frac{(M_z - M_0) \hat{z}}{T_1} \quad (1.2)$$

where γ is the gyromagnetic ratio, which is a property of atomic nuclei that relates their spin angular momentum to the nuclear magnetic moment. T_1 is the spin-lattice relaxation constant characteristic of the time it takes for nuclei to recover to a less energetic state via thermal energy loss to surrounding molecules. T_2 is the spin-spin relaxation constant characteristic of the time it takes for individual spins to desynchronize due to interactions with the magnetic moments of surrounding atoms.

In the simplest case, we can consider a homogeneous sample in a static, uniform magnetic field (i.e. $\mathbf{B} = B_0 \hat{z}$). Here, the solutions to the Bloch equation are:

$$M_{xy}(t) = M_{xy}(0) e^{-i\gamma B_0 t} e^{-\frac{t}{T_2}} \quad (1.3)$$

$$M_z(t) = M_0 + (M_z(0) - M_0) e^{-\frac{t}{T_1}} \quad (1.4)$$

where $M_{xy} = M_x + iM_y$ is the complex representation of the net magnetization in the xy-plane, also known as the transverse magnetization, and M_z is the net longitudinal magnetization along \hat{z} . The exponential terms in equations (1.3) and (1.4) reveal three key properties that are fundamental to MRI:

- I) Per Euler's formula, the complex exponential $e^{-i\gamma B_0 t}$ reveals that the transverse magnetization vector undergoes precession at a frequency given by $\omega_0 = \gamma B_0$; this is referred to as the Larmor frequency.
- II) The term $e^{-\frac{t}{T_2}}$ reveals that the net transverse magnetization decays to 0 at a rate dictated by T_2 .

- III) The term $e^{-\frac{t}{T_1}}$ reveals that the net longitudinal magnetization recovers to the equilibrium value of M_0 at a rate dictated by T_1 .

1.5.2. Signal Acquisition

To generate a signal for MRI, the net magnetization within a sample is first tipped into the transverse plane to generate a nonzero M_{xy} . This is achieved by applying a radiofrequency (RF) magnetic field oscillating at the Larmor frequency, represented as $B_1(t) = B_1 e^{-i\omega_0 t}$. The B_1 field applies an “effective torque” to the magnetization vector, causing it to rotate, and the tip angle depends on the strength of the B_1 field and the duration of the RF pulse:

$$\theta(t) = \gamma \int B_1(t) dt \quad (1.5)$$

RF coils are used to detect the precessing transverse magnetization through Faraday’s Law of Induction, wherein a changing magnetic field generates an electric current in a conducting material. The net acquired signal, $S(t)$, is proportional to the transverse magnetization integrated through the entire sample volume:

$$S(t) \propto \iiint M_{xy}(x, y, z, t) dx dy dz \quad (1.6)$$

In practice, the static B_0 field is not completely homogeneous, as deviations can occur throughout the volume due to factors such as hardware limitations and magnetic susceptibility, the latter of which quantifies how magnetized a material will become in the presence of a magnetic field. Factoring in these inhomogeneities, the signal equation becomes:

$$S(t) \propto \iiint M_{xy}(x, y, z, t) e^{-i\phi(x,y,z,t)} dx dy dz \quad (1.7)$$

where ϕ is a nonzero and spatially varying phase that accumulates due to the magnetic field deviations, ΔB_0 , in the static B_0 field, given by:

$$\phi(x, y, z, t) = \gamma \int_0^t \Delta B_0(\tau) d\tau \quad (1.8)$$

This phase causes the net transverse magnetization to decrease due to destructive interference between spins. The net effect on M_{xy} (equation (1.3)) is that T_2 effectively decreases to become T_2^* :

$$T_2^* = \left(\frac{1}{T_2} + \frac{1}{T_2'} \right)^{-1} \quad (1.9)$$

where T_2' is the contribution to dephasing due to susceptibility.

The spin echo method is a technique that uses two RF pulses to reverse the effects of T_2' on the measured signal and limit transverse decay to the effects of T_2 . The first pulse is a 90° excitation that tips \mathbf{M} into the xy-plane, after which individual spins begin to rapidly dephase relative to each other due to field inhomogeneities. After some time, τ , a 180° refocusing pulse is applied to invert the phase accumulated in each of the individual spins (i.e. $-\phi$). The spins then begin to rephase and an echo forms at a time τ after the second pulse. The total time between the first RF pulse and the peak of the echo is known as the echo time (TE), and the net transverse magnetization at this point is given by equation (1.3) after substituting t with TE.

To acquire 2D images, a technique known as selective excitation is employed to ensure that only a thin slice of the sample is excited by the B1 RF pulse. Assuming the slices are to be orthogonal to the \hat{z} direction, a static gradient field (G_z) is applied along z to introduce a spatially varying Larmor frequency that linearly depends on z :

$$\omega_0(z) = \gamma(B_0 + G_z z) \quad (1.10)$$

The B1 field is then tuned to a particular frequency which determines the z -position of the slice to be excited (z_0) to produce a measurable signal. The thickness of the slice (Δz) is

related to the frequency and bandwidth (BW) of the RF pulse and the strength of the G_z gradient, per:

$$BW = \gamma G_z \Delta z \quad (1.11)$$

Figure 1-6 depicts how the B1 pulse frequency and bandwidth map to the slice position and thickness.

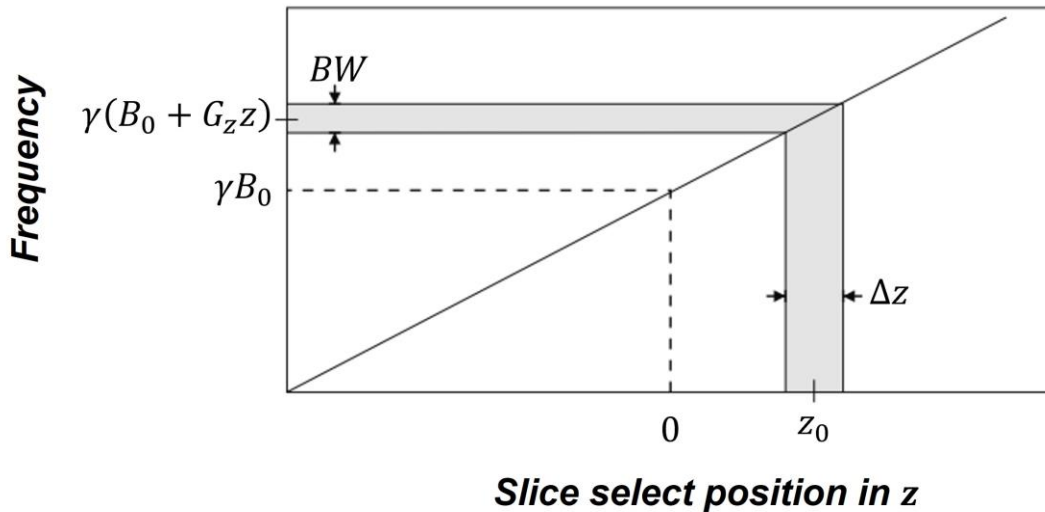


Figure 1-6. The precession frequency as a function of the position along the z -axis in the presence of a static gradient. The frequency bandwidth (shaded) determines the thickness of the excited slice. Image adapted from *Magnetic Resonance Imaging: Physical Principles and Sequence Design 2nd ed*, Brown, R.W. *et al*, 2014 and modified to maintain consistency with the symbols and terminology used in this work.

After selective excitation, time-varying gradients applied in the other base directions (here, \hat{x} and \hat{y}) induce spatially varying changes in the Larmor frequency:

$$\omega_0(x, y) = \gamma(B_0 + G_x(t)x + G_y(t)y) \quad (1.12)$$

Ignoring the phase introduced by B0 inhomogeneity and the T_2 decay exponential, the signal equation is given by:

$$S(t) \propto \iint M_{xy}(x, y, z) e^{-i(\gamma(\int_0^t G_x(\tau) d\tau)x + \gamma(\int_0^t G_y(\tau) d\tau)y)} dx dy \quad (1.13)$$

Equation (1.13) resembles the 2D Fourier transform of M_{xy} if the following substitutions are made:

$$\frac{\gamma}{2\pi} \int_0^t G_x(\tau) d\tau = k_x(t) \quad (1.14)$$

$$\frac{\gamma}{2\pi} \int_0^t G_y(\tau) d\tau = k_y(t)$$

where k_x and k_y represent the variables in the spatial frequency domain, also referred to as “k-space”. The measured signal at any point in time is therefore proportional to the transverse magnetization M_{xy} sampled at the spatial frequencies k_x and k_y :

$$S(t) = S(k_x, k_y) \propto \iint M_{xy}(x, y, z, t) e^{-i2\pi(xk_x + yk_y)} dx dy \quad (1.15)$$

By utilizing the G_x and G_y gradients to manipulate the k-space trajectory, and then measuring $S(t)$ at multiple time points, one can acquire enough samples of k-space to then reconstruct an image of the selected slice using the inverse 2D Fourier transform:

$$M_{xy}(x, y, z) = \iint S(k_x, k_y) e^{i2\pi(xk_x + yk_y)} dk_x dk_y \quad (1.16)$$

1.5.3. Imaging Considerations

In practice, the recorded signal is a discrete time series (rather than a continuous function) due to sampling limitations, and the resulting set of MRI data comprises a grid in k-space for each image slice. The recorded signal along either k_x or k_y can be represented as the multiplication of the continuous signal with a truncated comb function that introduces two significant limiting parameters: the total width of k-space acquired (w_{k_x} or w_{k_y}) and the sampling period (Δk_x or Δk_y).

The in-slice imaging resolution in 2D MRI is related to the size of the k-space grid per the following:

$$\Delta x = \frac{1}{W_{k_x}} \quad (1.17)$$

$$\Delta y = \frac{1}{W_{k_y}}$$

As revealed by equation (1.17), the spatial resolutions in the x and y directions are independent of each other, though in practice they are generally set to be equal.

The field-of-view (FOV) in 2D MRI is determined by the sampling periods Δk_x and Δk_y . This relationship is given by the following:

$$FOV_x = \frac{1}{\Delta k_x} \quad (1.18)$$

$$FOV_y = \frac{1}{\Delta k_y}$$

As with spatial resolution, the FOVs in the x and y directions are independent of each other, though it can be desirable to have different FOVs in each direction depending on the geometry of the object being imaged.

The truncation of the recorded signal due to sampling limitations introduces periodicity in the image domain because the Fourier transform of the k-space grid produces an infinite number of images. In practice, one such image is isolated and selected, while the rest are discarded. If the FOV in x or y is smaller than the width of the object being imaged, aliasing artifacts can occur, causing the images to overlap. The Nyquist criterion states that Δk should be less than or equal to FOV_{\min}^{-1} where FOV_{\min} is the width of the object being imaged along a particular direction.

1.5.4. Echo Planar Imaging

A consequence of sensitizing the MR signal to the motion of water molecules is that dMRI is inherently susceptible to patient movement. To reduce the confounding effects of gross head motion and physiological motion on signal measurements, dMRI often uses an acquisition technique called echo planar imaging (EPI) to acquire an entire 2D k-space grid after a single RF excitation [41]. With EPI, it's possible to obtain an MR slice in under 100 ms.

A typical single shot EPI sequence used in dMRI resembles a spin echo pulse sequence with the addition of diffusion-sensitizing gradients and a modified readout strategy for sampling the signal, as depicted in Figure 1-7. Time-varying gradients in the two perpendicular in-plane directions (here, x and y) are applied during readout to manipulate the k-space trajectory, ultimately resulting in the acquisition of an entire k-space grid after one excitation.

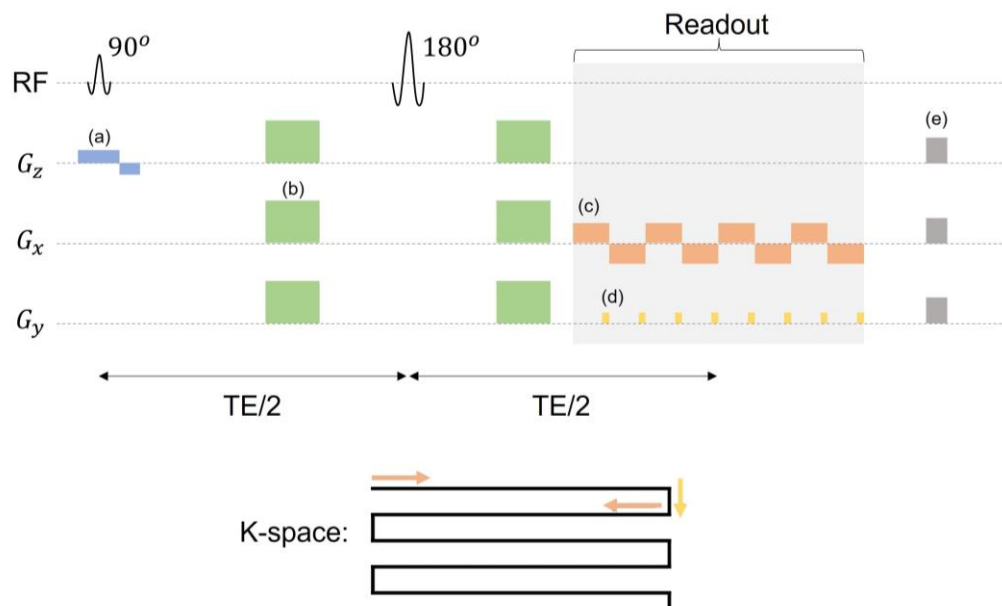


Figure 1-7. Simplified pulse sequence diagram for a diffusion-weighted echo planar imaging (EPI) acquisition. All waveforms are depicted as a function of time. Top: The slice selection gradient (blue, (a)) limits excitation from the initial 90° radiofrequency (RF) pulse to a single slice in the z-direction. On either side of the inverting 180° RF pulse are dephasing and rephasing diffusion-sensitizing gradients (green, (b)). The gradients applied during readout manipulate the k-space trajectory: each rectangular gradient in the x-direction (orange, (c)) moves the k-space sampling trajectory through a line in the k_x direction, while each “blip” gradient in the y-direction (yellow, (d)) shifts the sampling trajectory to a new line in k_y . The spoiler gradients at the end of the sequence (gray, (e)) remove any remaining transverse magnetization. Bottom: During readout, alternating lines of k-space are sampled in reverse directions.

1.6. Diffusion-weighted MRI

1.6.1. Physics of Diffusion

Diffusion refers to the thermal motion small molecules experience at temperatures above absolute zero. The process was first described by Robert Brown in 1827, who was observing pollen immersed in water through a microscope [42]; random self-diffusion is

thus commonly referred to as Brownian motion. However, it was Adolf Fick who first described how solute particles are distributed over time because of nonuniform concentration, via Fick's second law:

$$\frac{\partial \varphi(\mathbf{r}, t)}{\partial t} = D \nabla^2 \varphi(\mathbf{r}, t) \quad (1.19)$$

where φ is the concentration of a particular particle at time t and position \mathbf{r} , and D is the diffusivity or diffusion coefficient in units of $length^2 \ time^{-1}$. In the presence of a concentration gradient, equation (1.19) describes the net movement of particles from a region of higher concentration to lower concentration; for example, a pinch of salt added to a glass of water would disperse until the salt was uniformly distributed throughout the glass. Albert Einstein demonstrated that in the absence of a concentration gradient, the above equation can be used to describe the stochastic nature of Brownian motion and $\varphi(\mathbf{r}, t)$ can be interpreted as the probability density function of a particular individual particle's location, \mathbf{r} , after a time, t [43].

For a particle in a solution that isn't limited by any external barriers, the probability distribution of the particle's one-dimensional displacement (along x) after a diffusion time, t , resembles a Gaussian function:

$$\varphi(x, t) = \frac{1}{\sqrt{4\pi Dt}} e^{\left(-\frac{x^2}{4Dt}\right)} \quad (1.20)$$

An example probability distribution of a particle's displacement at three time points is depicted in Figure 1-8. The variance of this distribution expresses the mean squared displacement of the particle:

$$\overline{x^2} = 2Dt \quad (1.21)$$

Particles that adhere to equations (1.20) and (1.21) are said to be undergoing *free* or *Gaussian* diffusion.

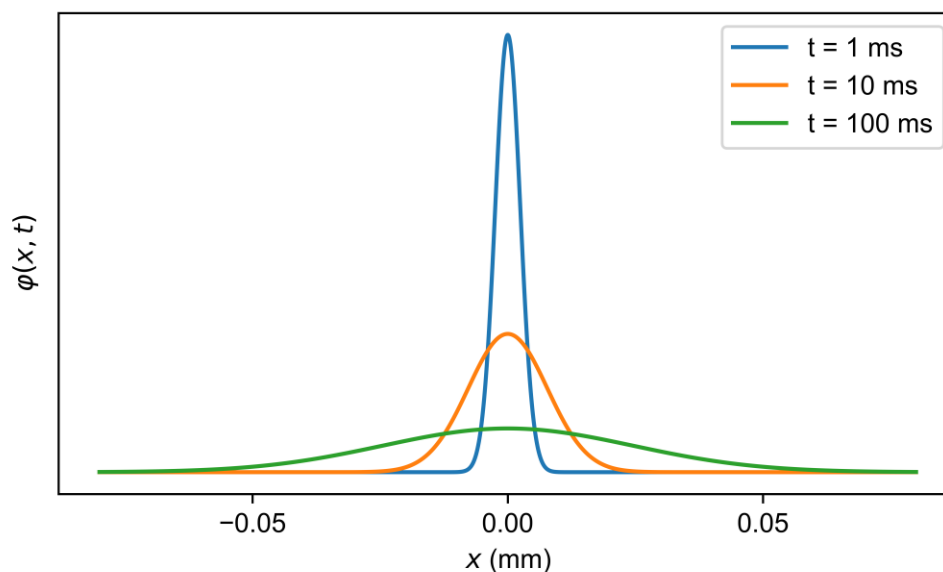


Figure 1-8. Probability distributions for the location of a particle experiencing Gaussian diffusion in the x-direction. Depicted curves were generated using a diffusion coefficient of $3.0 \times 10^{-3} \text{ mm}^2/\text{s}$.

In biological tissues, the assumptions of the Gaussian diffusion regime are violated because the movement of water molecules is impeded by the presence of membranes, boundaries, and various structures. When a molecule is constrained by the presence of an impermeable barrier, that molecule is said to be undergoing *restricted diffusion*, while a molecule that encounters a semi-permeable barrier or other obstacles that impede but don't completely prohibit movement is said to be undergoing *hindered diffusion*. Let us consider a group of neuronal axons aligned coherently, as depicted in Figure 1-9a. Assuming that either the myelin sheath or axonal membrane are impermeable, water molecules within the axons are experiencing restricted diffusion. Water molecules in the area extracellular space are impeded by the axons but can otherwise move around them and are thus experiencing

hindered diffusion. Water molecules in a distant free CSF pool, which are unimpeded by obstacles or boundaries, are undergoing free or Gaussian diffusion.

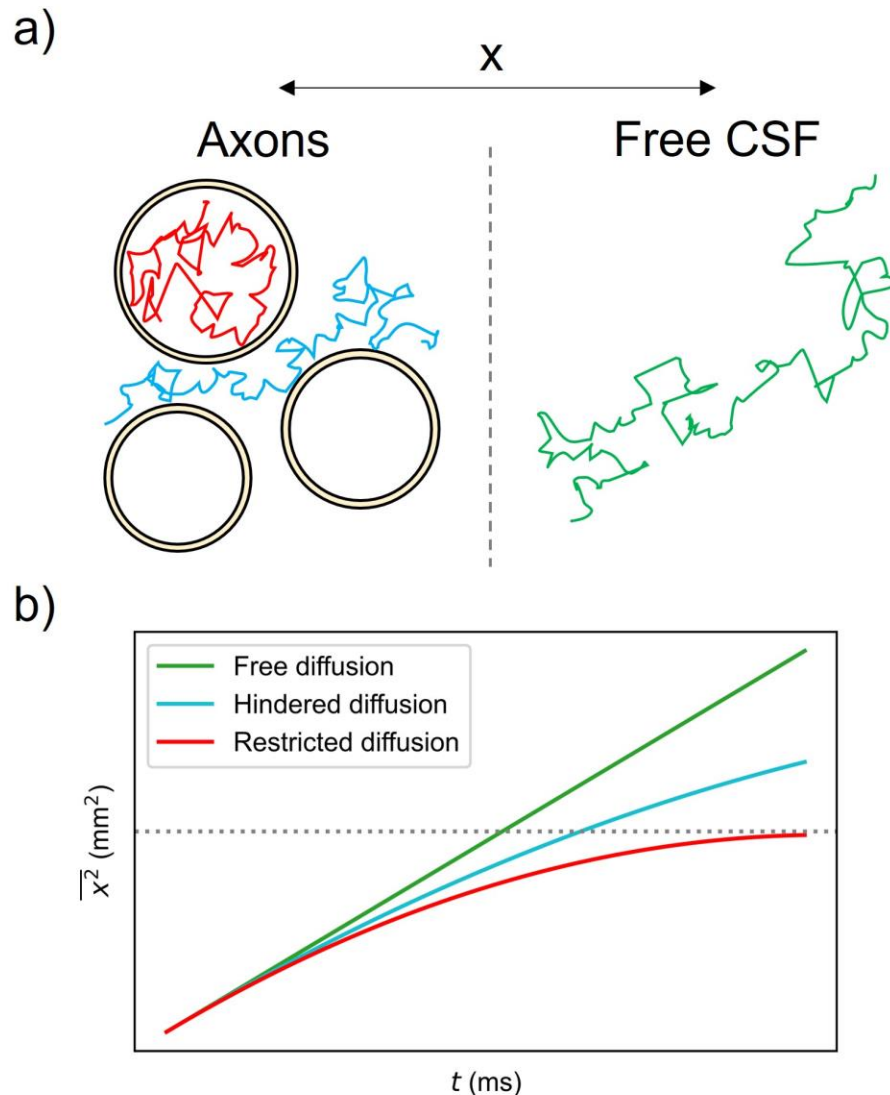


Figure 1-9. (a) Potential trajectories of water molecules experiencing restricted diffusion (red), hindered diffusion (blue), and free diffusion (green) along the x-direction. The circles represent cross-sections of neuronal axons with impermeable membranes. (b) Mean squared displacement of molecules along the x-direction ($\overline{x^2}$) as a function of diffusion time. The asymptotic dotted line depicts the maximum $\overline{x^2}$ of molecules undergoing restricted diffusion, resulting from the finite size of the impermeable axons.

1.6.2. Diffusion and the MRI Signal

The effects of molecular diffusion on NMR experiments are described by the Bloch-Torrey equation, in which an additional term is introduced to the Bloch equation (equation (1.2)) to account for diffusion [44]:

$$\frac{d\mathbf{M}}{dt} = \gamma\mathbf{M}\times\mathbf{B} - \frac{M_x\hat{x} + M_y\hat{y}}{T_2} - \frac{(M_z - M_0)\hat{z}}{T_1} + D\nabla^2\mathbf{M} \quad (1.22)$$

The net transverse magnetization can be described by the following:

$$\frac{dM_{xy}}{dt} = -i\gamma\mathbf{G}\cdot\mathbf{r} - \frac{M_{xy}}{T_2} + D\nabla^2M_{xy} \quad (1.23)$$

where \mathbf{G} is an applied gradient magnetic field. Ignoring the phase accumulated due to applied gradient and the T_2 relaxation decay to isolate the effects of diffusion on the MR signal, the solution to equation (1.23) is given by [45]:

$$S \propto e^{-D\gamma^2 \int_0^t \left(\int_0^{t'} \mathbf{G}(t'') dt'' \right)^2 dt'} \quad (1.24)$$

Equation (1.24) reveals that diffusion of spins causes attenuation of the MRI signal due to the phase incoherence that arises from motion, and that this attenuation is modulated by the diffusivity and the strength and duration of the applied gradients.

In 1965, Stejskal and Tanner demonstrated the first MRI pulse sequence for diffusion-weighted image contrast; the Stejskal-Tanner sequence is one variation of the pulsed gradient spin echo (PGSE) sequence and is depicted with rectangular gradients in Figure 1-10 [46]. PGSE resembles a spin echo sequence with the addition of two (usually) identical gradient waveforms inserted before and after the 180° RF pulse to dephase and then, after some time, rephase spins. If spins remain fixed in position, the net phase induced by the diffusion gradients will be zero. However, if spins move along the direction of the

diffusion gradients during the time between the dephasing and rephasing waveforms, they acquire a net phase that accelerates the decay of M_{xy} due to phase dispersion.

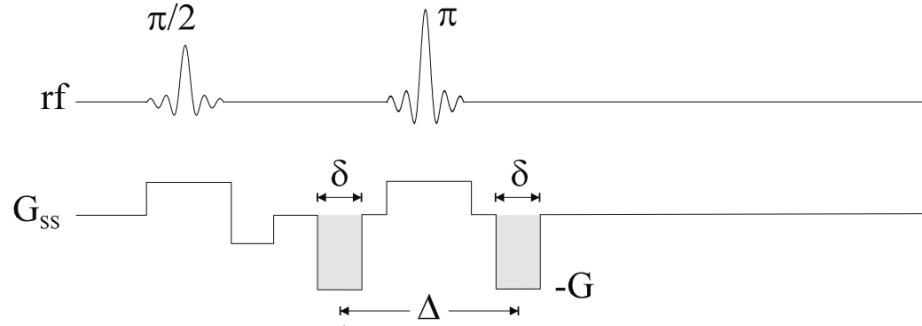


Figure 1-10. A conventional “Stejskal-Tanner” pulsed gradient spin echo sequence with rectangular gradients. The initial 90° radiofrequency (rf) pulse excites the slice of the sample that has a Larmor frequency matching the pulse frequency, which is determined by the slice selection gradient (G_{ss}). After a time, a 180° rf pulse is applied to invert the magnetization vectors, leading to the production of an echo. The diffusion-encoding gradients (shaded gray) are applied on either side of the second rf pulse to dephase and then rephase the individual spins. Note that the diffusion gradients are each applied for a duration of δ , are separated by a time of Δ (start to start), and have a gradient strength of G . Not depicted in this image are the gradients used to manipulate the k-space trajectory (G_x and G_y). Image adapted from *Magnetic Resonance Imaging: Physical Principles and Sequence Design 2nd ed*, Brown, R.W. *et al*, 2014.

The solution to equation (1.24) for a Stejskal-Tanner PGSE sequence, as depicted in Figure 1-10, is given by:

$$S \propto e^{-D\gamma^2 G^2 \delta^2 \left(\Delta - \frac{\delta}{3}\right)} \quad (1.25)$$

where G is the magnitude of the applied diffusion-sensitizing gradients, each of which has a duration δ , and with a delay of Δ between them. Equation (1.25) can be simplified by performing a substitution to replace all variables related to the diffusion gradients with a

single term that quantifies the degree of diffusion-weighting and is known as the b-value or simply b . The acquired signal can then be expressed as a function of the b-value, denoted S_b . When $b = 0$, there is no diffusion-weighting, and the measured signal depends only on other factors such as transverse and longitudinal relaxation. Expressing S_b in terms of the signal absent diffusion-weighting, S_0 , gives:

$$S_{\mathbf{g},b} = S_0 e^{-bADC} \quad (1.26)$$

where $\mathbf{g} = (g_1, g_2, g_3)$ is a unit vector denoting the direction of the applied diffusion-sensitizing gradients and ADC is the apparent diffusion coefficient along \mathbf{g} . An assumption of equation (1.26) is that all movement of water molecules within the voxel-of-interest arises from Gaussian diffusion, which is often untrue *in vivo* (1.6.1). Hence, the ADC is an approximation of diffusivity rather than a true diffusion coefficient.

1.6.3. Diffusion Tensor Imaging

Diffusion tensor imaging (DTI) is a technique that uses PGSE acquisitions to estimate a symmetric 3×3 matrix that characterizes the diffusion of water molecules within a voxel, known as the diffusion tensor, $\mathbf{D} = [D_{11}, D_{22}, D_{33}, D_{12}, D_{13}, D_{23}]$ [47]. Typically, PGSE signals are acquired at $b = 0$ and at a nonzero b-value (usually 1000 s/mm^2), and are then fitted to the DTI signal representation to solve for \mathbf{D} :

$$S_{\mathbf{g},b} = S_0 e^{-b \sum_{i,j=1}^3 g_i g_j D_{ij}} \quad (1.27)$$

A minimum of six directions at the nonzero b-value are needed to solve for the six unknown elements in the diffusion tensor, but acquiring more directions spread out evenly along a sphere can mitigate rotational biases and improve signal-to-noise ratio (SNR).

The most commonly used scalar quantities derived from DTI fall into two categories: measures of diffusion magnitude and measures of diffusion anisotropy [48].

The first step in estimating these metrics is to compute the eigenvalue/eigenvector pairs of the \mathbf{D} matrix; the eigenvalues (λ_1 , λ_2 , and λ_3) quantify the ADC along the three principal axes defined by the eigenvectors (\mathbf{v}_1 , \mathbf{v}_2 , and \mathbf{v}_3) and can be visualized as an ellipsoid, as depicted in Figure 1-11.

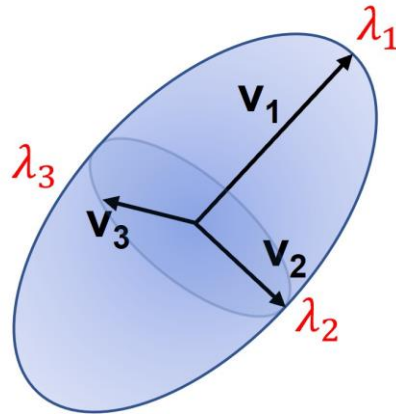


Figure 1-11. An ellipsoid depicting the eigenvalue/eigenvector pairs corresponding to the diffusion of water within a voxel. The black arrows portray the directions of the eigenvectors, while the eigenvalues (red) quantify the average diffusivity along those directions. In this example, the principal eigenvalue (λ_1) is greater than the other eigenvalues, implying that diffusion within this voxel is anisotropic and that diffusivity is greatest along \mathbf{v}_1 . In a voxel with isotropic diffusion, the ellipsoid would instead resemble a sphere with $\lambda_1 = \lambda_2 = \lambda_3$.

The mean diffusivity (MD) is a measure of the average diffusivity in the voxel across all directions and is estimated by computing the mean of the eigenvalues [49]:

$$MD = \frac{\lambda_1 + \lambda_2 + \lambda_3}{3} \quad (1.28)$$

At 37°C (the average human internal temperature) the diffusivity of free water is 3e-3 mm²/s; however, DTI measurements made in WM and GM regions yield lower diffusivity estimates (~0.7-1e-3 mm²/s [50]) because of hindered and restricted diffusion due to membranes and other obstacles inside cells and in the extracellular space. Other DTI

diffusivity measurements of interest are the axial or longitudinal diffusivity, which is the principal eigenvalue, λ_1 , and the radial or perpendicular diffusivity, which is the mean of the two smaller eigenvalues, $0.5(\lambda_2 + \lambda_3)$.

Fractional anisotropy (FA) is a normalized scalar measure of the variance in diffusivity across directions [49]. FA is 0 in a voxel in which diffusion is isotropic (i.e. equal in all directions), whereas FA is closer to 1 in a voxel in which the axial diffusivity is much greater than the radial diffusivity. FA is estimated using the following equation:

$$FA = \sqrt{1.5} \sqrt{\frac{(\lambda_1 - MD)^2 + (\lambda_2 - MD)^2 + (\lambda_3 - MD)^2}{\lambda_1^2 + \lambda_2^2 + \lambda_3^2}} \quad (1.29)$$

Example slices of FA, MD, axial diffusivity, and radial diffusivity are depicted in Figure 1-12.

In addition to producing scalar measurements that characterize diffusion *in vivo*, DTI can also be used to estimate and model nerve tracts in the brain via a process known as tractography [51].

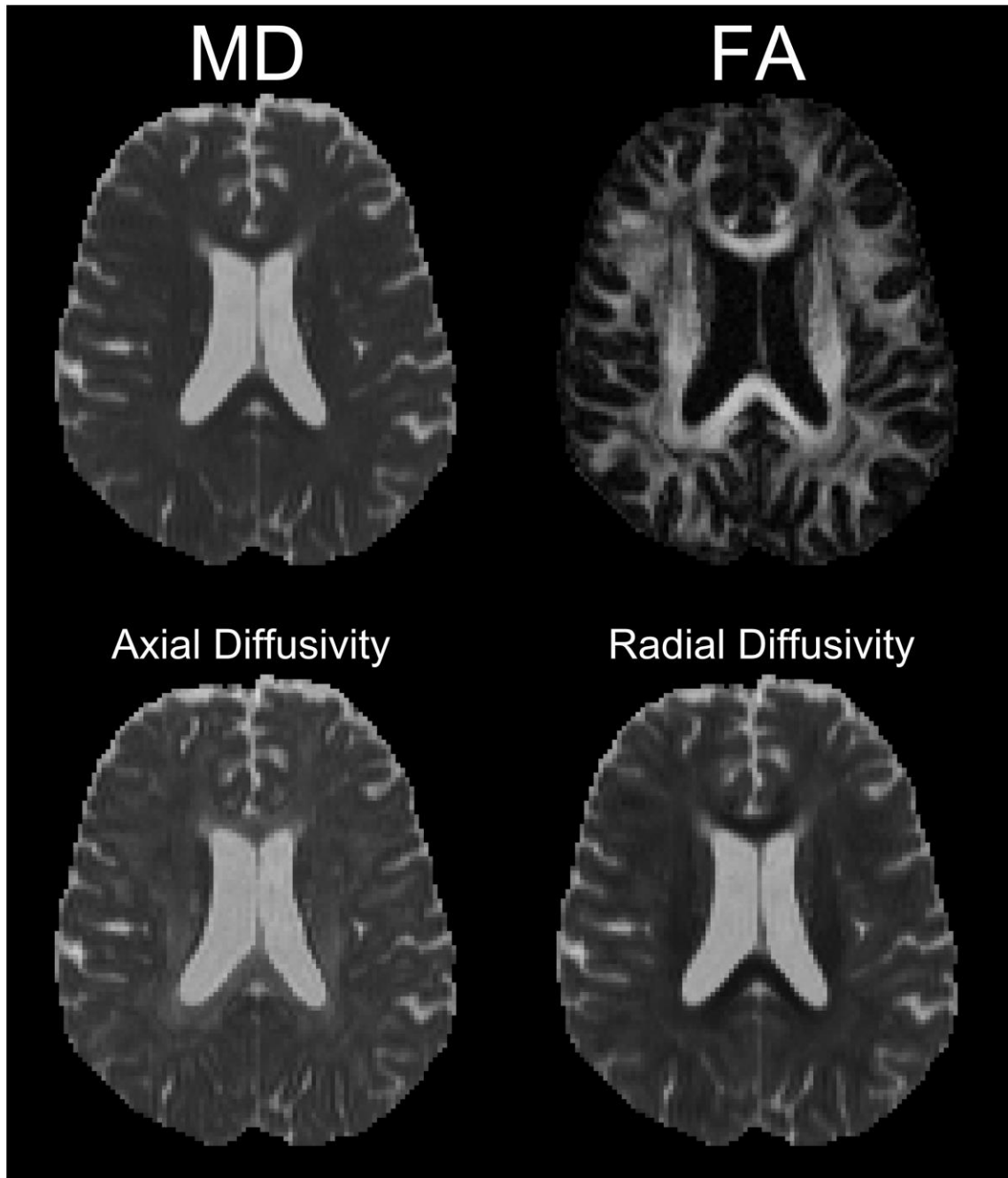


Figure 1-12. Examples of mean diffusivity (MD), fractional anisotropy (FA), axial diffusivity, and radial diffusivity maps from a patient with epilepsy, all normalized to pixel intensities ranging from 0 to 1. This image was acquired with appropriate Research and Ethics Board approval.

The usefulness of DTI measurements arises from the relationship between water diffusion and neuroanatomy. Pathological changes to brain anatomy, such as those described in Section 1.3.3, often affect MD and FA measurements. For example, a significant decrease in MD can indicate acute cellular swelling after stroke or injury [52], [53], while an increase can indicate an increased extracellular fluid volume caused by tissue loss or atrophy [54]. FA is often considered a surrogate measure of WM integrity [48], as water diffusion within neuronal axons tends to be highly anisotropic, and changes in FA can result from many factors including demyelination, neurodegeneration, and axonal atrophy. Because of its sensitivity to neuroanatomy, DTI has been applied to a large variety of studies including traumatic brain injury [55], MS [56], aging [57], and schizophrenia [58].

Despite its wide usage, the DTI signal representation has some major limitations, three of which are significant to this thesis: (I) the assumption that all diffusion arises from Gaussian sources, (II) the confounding effects of axon fiber orientation dispersion on voxel-wide measurements of anisotropy, and (III) free water partial volume effects.

Limitation I: Gaussian diffusion

In DTI, the signal acquired at each diffusion direction is modeled by equation (1.26) and is assumed to result from free diffusion along said direction. In the mono-Gaussian diffusion scheme the diffusivity should remain constant regardless of the diffusion time, but in real brain tissue the apparent diffusivity exhibits diffusion time-dependence. If the diffusion time is short enough that most water molecules do not reach any restricting or hindering boundaries within the tissue, the measured ADC will be equal to the diffusivity of free water [59]. However, if the diffusion time is long enough that most molecules will

encounter barriers, the measured ADC will decrease to an asymptotic value called the steady state ADC. For consistency across studies, standard DTI experiments aim to probe long diffusion times and acquire steady-state ADC measurements. Given that microstructural brain tissue compartments (i.e. cells) are typically on the order of $\sim 1 \mu\text{m}$ or less in size, equation (1.21) predicts that a diffusion time of ~ 20 ms or greater is needed to measure steady state ADC.

The mono-Gaussian diffusion assumption is an oversimplification even when steady state measurements are achieved via long diffusion times because the diffusivity within a voxel represents the sum of diffusivities of all water molecules from multiple water-containing compartments (i.e. axons, soma, extracellular water, etc.) and over multiple directions. Water molecules in different compartments within the voxel may be diffusing at different rates, and the signal would be better characterized by a multi-exponential decay function. Per equation (1.26), the logarithm of the dMRI signal should decrease linearly with increasing b-value, but in most tissue-containing voxels, the signal vs. b-value deviates from this straight line due to the variance in diffusivity (Figure 1-13). Though the signal deviation is not significant at the relatively low b-values used in DTI [60], more advanced signal representations that can quantify this deviation may provide more information about the underlying tissue [61], [62].

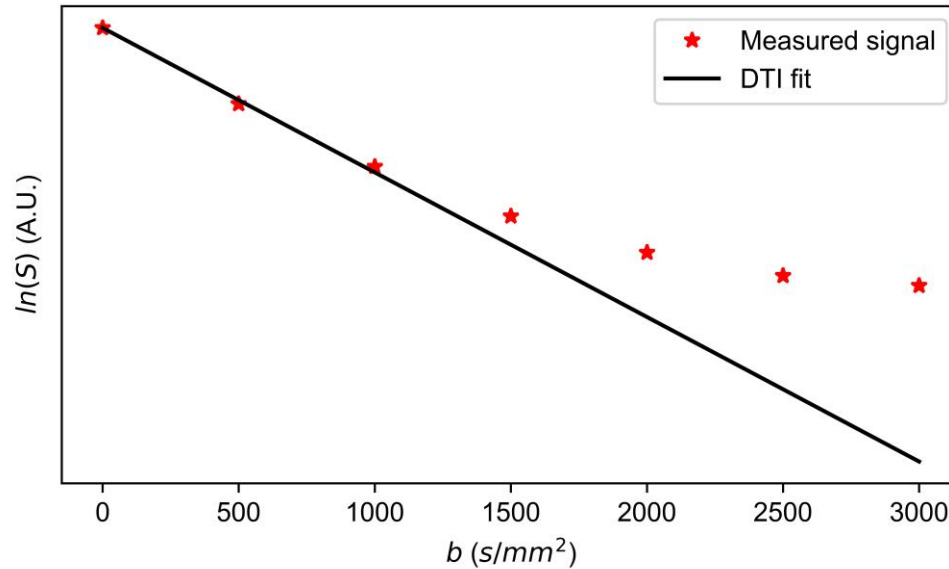


Figure 1-13. Logarithm of a typical diffusion MRI signal (S) from a tissue-containing voxel sampled at seven b -values. The low b -value signal fitted to the DTI signal representation (black), which assumes Gaussian diffusion within the voxel, resembles a straight line, while the measured signal (red) deviates from this representation at higher b -values. Plot generated using simulated data.

Limitation II: Fiber orientation dispersion

WM is a common target for DTI studies because it is primarily composed of neuronal axons bundled together to form tracts, and water within and around these structures exhibits restricted and anisotropic diffusion. When axons are aligned coherently within a voxel (i.e. parallel to one another), FA can reasonably act as a surrogate metric of neurodegeneration, but there are challenges associated with crossing or fanning axon alignments. First, the diffusion tensor exhibits a rounder shape and FA is in turn reduced, limiting the metric's specificity to true pathological abnormalities (Figure 1-14). Second, there are circumstances in which voxelwise anisotropy increases while cellular/microscopic anisotropy decreases [63]; for example, FA was found to increase in a region containing

crossing axons when axons along one direction were preferentially damaged compared to those in a perpendicular tract [64].

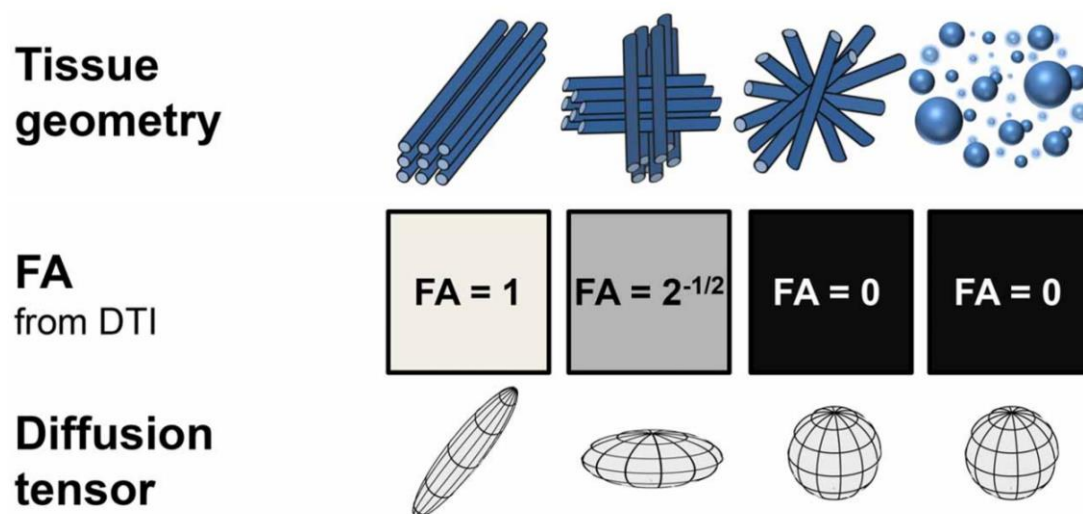


Figure 1-14. The effects of various tissue geometries on fractional anisotropy (FA). The cylinders can be said to approximate neuronal axons, while the spheres can represent non-neuronal, spherical cells. Though columns 1-3 all depict intact axons, the decreasing orientational coherence from left to right leads to decreasing values of FA. This confounding effect of axon orientation limits the specificity of FA to white matter neurodegeneration. The diffusion tensor signal representation cannot distinguish between incoherently arranged axons (column 3) and spherical cells (column 4), as diffusion appears isotropic in both cases. Image adapted from “Microanisotropy imaging: quantification of microscopic diffusion anisotropy and orientational order parameter by diffusion MRI with magic-angle spinning of the q-vector”, Lasic S. *et al*, *Frontiers in Physics*, 2014.

Limitation III: Free water partial volume effects

Free water partial volume effects occur in voxels that contain both tissue and free water, such as at the interface between brain tissue and a CSF-containing ventricle. The diffusivity and T_2 -weighted signal of free water are much greater than those of brain tissue, and free water diffusion is isotropic, so voxel-wide DTI measurements are biased by free water even

when the free water volume fraction is low [65]. Typically, MD and other diffusivity measurements are increased in voxels contaminated by free water, while FA is reduced.

1.6.4. Advanced Diffusion Imaging

Advanced diffusion techniques have been developed to overcome one or more of the shortcomings of DTI. To probe more information about tissue, these techniques utilize different signal representations, unique diffusion-encoding pulse sequences, or both. Generally, these advanced techniques have some trade-offs compared to DTI such as increased scan times, lower SNR, or reduced reproducibility/robustness resulting from the use of more complex signal representations.

The diffusion kurtosis imaging (DKI) signal representation is an extension of DTI that introduces a fourth order symmetric tensor, known as the kurtosis tensor or \mathbf{W} , to characterize non-Gaussian and/or multi-Gaussian diffusion by quantifying the variance in diffusivities within the voxel-of-interest. The DKI signal can be represented as [62], [66]:

$$S_{g,b} = S_0 e^{-b \sum_{i,j=1}^3 g_i g_j D_{ij} + \frac{1}{6} b^2 \sum_{i,j,k,l=1}^3 g_i g_j g_k g_l W_{ijkl} + O(b^3)} \quad (1.30)$$

where W_{ijkl} denotes the $ijkl^{th}$ element of the kurtosis tensor and $O(b^3)$ is a higher order term. DKI parameters have shown high specificity to WM and GM alterations in many diseases including Parkinson's [67], Alzheimer's [68], temporal lobe epilepsy [69], [70], and others. Figure 1-15 compares the DKI fit to DTI in a voxel with non-Gaussian or multi-Gaussian diffusivity.

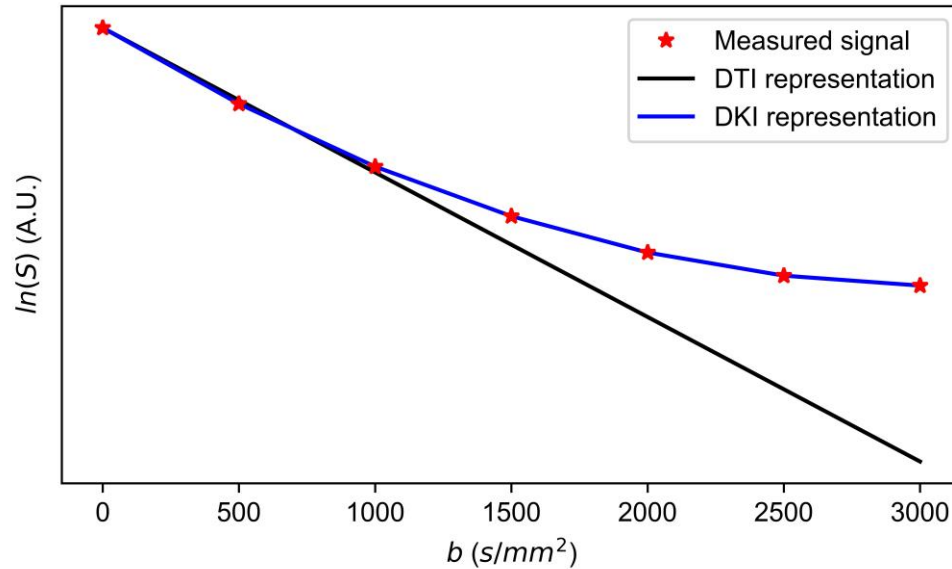


Figure 1-15. Diffusion tensor imaging (DTI) and diffusion kurtosis imaging (DKI) signal representations fitted to MRI signal (S) from a tissue-containing voxel sampled at seven b -values. By characterizing the variance of diffusivities, or kurtosis, the DKI representation (blue) better fits the acquired data (red) than the DTI representation (black). Plot generated using simulated data.

Microscopic fractional anisotropy (μ FA) imaging is a dMRI technique that quantifies water diffusion anisotropy independent of neuron fiber orientation dispersion [71], [72]. Compared to the FA metric estimated in DTI, μ FA is more specific to microstructural abnormalities in voxels containing crossing or fanning axons, as depicted in Figure 1-16. Some examples in which μ FA outperforms FA due to its increased specificity are in evaluating WM degeneration [73], detecting lesions in MS [74], and differentiating between brain cancer types [75]. There are several different methods to estimate μ FA, which are discussed in greater detail in Chapter 2. In this work, μ FA is estimated from data acquired in both the linear tensor encoding (LTE) domain (Figure 1-10), in which each acquisition probes diffusion in one linear direction, and the spherical

tensor encoding (STE) domain, in which diffusion is probed in all directions independently. While LTE acquisitions are affected by both the size dispersion of water-containing compartments within a voxel and diffusion anisotropy, STE acquisitions are only sensitive to size dispersion; thus by acquiring data in both schemes, anisotropy can be estimated [72]. An example of an STE gradient waveform is the qMAS technique described by Eriksson *et al* [76], though this work uses an alternative sequence that utilizes trapezoidal gradients.

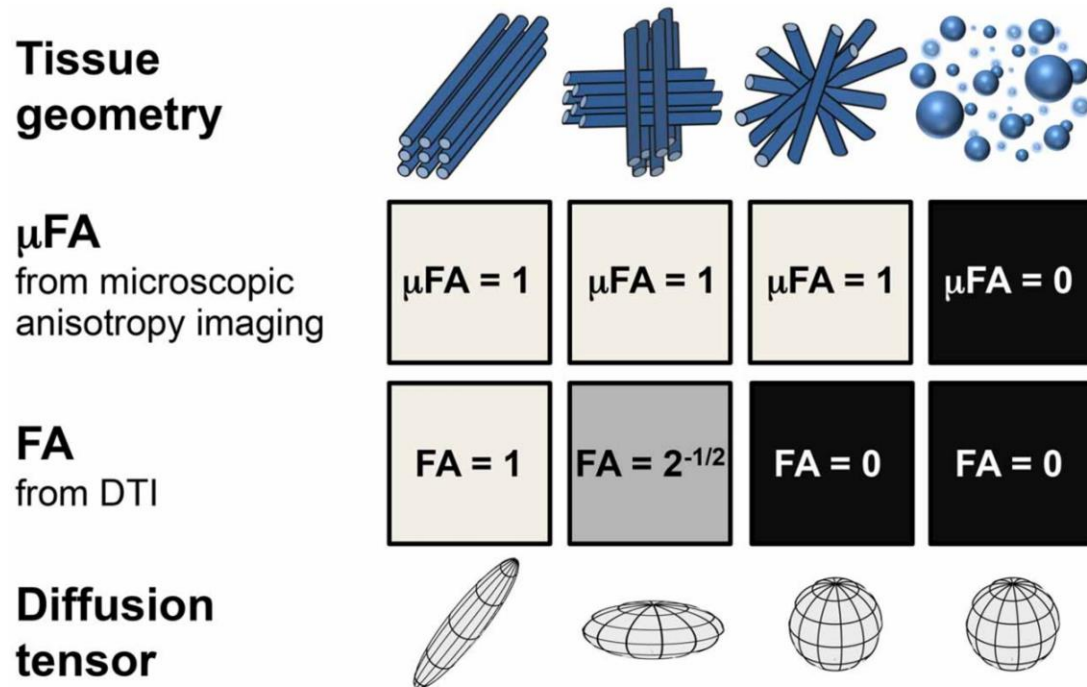


Figure 1-16. The effects of various tissue geometries on both fractional anisotropy (FA) and microscopic fractional anisotropy (μ FA). The cylinders can be said to approximate neuronal axons, while the spheres can represent non-neuronal, spherical cells. FA and μ FA are equivalent in voxels containing coherently aligned axons (column 1) and voxels containing only spherical cells (column 4), but when voxels contain crossing axons, as in columns 2-3, μ FA correctly detects anisotropic diffusion whereas FA reports reduced anisotropy due to the confounding effects of fiber orientation. Image retrieved from “Microanisotropy imaging: quantification of microscopic diffusion anisotropy and orientational order parameter by diffusion MRI with magic-angle spinning of the q-vector”, Lasic S. *et al*, *Frontiers in Physics*, 2014.

Techniques to eliminate or attenuate free water partial volume effects often utilize multi-compartment models that separate the dMRI signals arising from different sources. Free water elimination (FWE) signal representations decompose the signal into two

components: signal arising from water in and around tissue, and signal arising from free water sources [77]:

$$S_{Voxel} = fS_{Tissue} + (1 - f)S_{CSF} \quad (1.31)$$

where S_{Voxel} is the total signal recorded in the voxel-of-interest at a particular b-value and direction, S_{Tissue} and S_{CSF} are the respective tissue and free water signal components, and f is the tissue volume fraction. Much like DKI and μ FA, FWE techniques have demonstrated potentially greater specificity over DTI in diseases such as Parkinson's [78], Alzheimer's [79], and traumatic brain injury [80]. FWE techniques are discussed in greater detail in Chapter 3.

In addition to DKI, μ FA, and FWE techniques, numerous other advanced dMRI techniques have been developed, though a comprehensive review is beyond the scope of this work.

Chapter 2 focuses on the development and optimization of an imaging technique that can acquire full-brain μ FA image volumes within clinically viable scan times.

Chapter 2

2 Rapid Microscopic Fractional Anisotropy Imaging via an Optimized Linear Regression Formulation

2.1. Overview

This chapter was published in *Magnetic Resonance Imaging*, volume 80, Arezza *et al*, *Rapid Microscopic Fractional Anisotropy Imaging via an Optimized Linear Regression Formulation* [81], pages 132-143, Copyright Elsevier, 2021.

2.2. Introduction

Diffusion-weighted MRI (dMRI) can noninvasively acquire information about the microstructural characteristics of biological systems by probing the displacement of water molecules in tissue [46], [82]. Microstructural features that affect the apparent diffusion rate of water include cell size, shape, density, orientation, and the presence of membranes and barriers; thus, dMRI has found use in the study of neurological diseases that alter tissue microstructure [56], [83]–[85].

The most commonly used dMRI technique is diffusion tensor imaging (DTI) [86], in which dMRI data is fitted to the diffusion tensor signal representation to estimate metrics such as the mean diffusivity (MD) and fractional anisotropy (FA). DTI represents the dMRI signal as being entirely characterized by Gaussian diffusion [87], implicitly meaning the logarithm of the dMRI signal is assumed to depend on the b-value up to the first order in the cumulant expansion [88]. However, diffusion in tissues is too complex to be fully represented by Gaussian diffusion at high b-values [60], and characterizing the "non-Gaussian" signal provides more information about the underlying tissue [61], [89], [90]. Diffusion kurtosis imaging (DKI) was developed to capture the effects of non-Gaussian

diffusion by expanding the dMRI signal using cumulants up to second order in b-value [62]. Generally, DKI has been shown to be more sensitive than DTI towards quantifying microstructural changes that result from disease [67], [91], [92].

Non-Gaussian diffusion can be attributed to a number of sources including isotropic kurtosis from polydisperse diffusion tensors with different mean diffusivities, anisotropic kurtosis from diffusion tensors dispersed among multiple orientations, time-dependent diffusion [93], and microscopic kurtosis from restricted diffusion and microscopic structural disorder [89], [93]–[95]. Unfortunately, both DTI and DKI are unable to distinguish between true microstructural changes and neuron fiber orientation dispersion, reducing their specificity to disease in brain regions containing crossing or fanning axons [75], [96]. While DTI does not consider the effects of kurtosis at all, DKI cannot differentiate between any of the different sources of kurtosis without imposing assumptions about the underlying tissue [62], [97].

In recent years, efforts have been made to develop dMRI techniques that can quantify water diffusion anisotropy independent of orientation dispersion [71], [72]. Microscopic anisotropy (μA) is an anisotropy metric that is independent of both reference frame and orientation dispersion, and microscopic fractional anisotropy (μFA) is a normalized variation of μA that additionally aims to remove the dependence on compartment size [98]. There are multiple techniques to compute μFA , which can be categorized into: (1) methods that involve the use of linear tensor encoding (LTE) sequences [99]–[101], (2) methods that utilize double diffusion encoding (DDE) [102], and (3) methods that use nonconventional continuous gradient waveforms such as spherical tensor encoding (STE) [72], [75], [103]–[105].

LTE methods utilize models to decouple microstructural properties from mesoscopic tissue orientation [106]. These techniques require prior knowledge or estimates of tissue properties such as the axonal volume fraction or the intracellular radial diffusivity [106] but are highly accessible because LTE sequences are commonly used in both DTI and DKI. Generally, anisotropy can be estimated by acquiring LTE signals across multiple directions and b-shells and fitting the powder-averaged signals to a constrained model such as the spherical mean technique (SMT) model [100], [101]. Recently, Henriques *et al* showed that μ FA estimations using LTE are inaccurate compared to ground truth anisotropy, suggesting the techniques are not robust or do not sufficiently describe the underlying microstructure [106].

DDE techniques to estimate μ A and μ FA use two independent diffusion-encoding pulse vectors in succession to probe the correlation of water diffusion in different directions [71], [107]–[110]. DDE can distinguish between microstructural properties and orientation dispersion without imposing modeling constraints [102], [107], likely making the technique more robust and accurate than LTE techniques by eliminating the possibility of assumption misestimation. Furthermore, the clinical viability of DDE μ FA imaging was demonstrated in a preliminary study of multiple sclerosis (MS) patients at 3T with a 5 minute scan time and 3 mm isotropic resolution [74], and the minimalistic sampling scheme used in that work was further validated [111]. While DDE is a promising technique, it has some limitations. Due to the use of two consecutive diffusion-encoding pulses separated by a mixing time, DDE sequences require longer TEs than standard LTE sequences to achieve equal b-values. Furthermore, a twice-refocused implementation is required to avoid biases due to concomitant fields [112], [113], further increasing the TE.

A notable example of a DDE technique to estimate μ FA is correlation tensor imaging (CTI) [94].

Techniques that utilize nonconventional diffusion-encoding waveforms probe unique q -space trajectories that provide additional information about tissue microstructure beyond the capabilities of LTE. In STE-based methods, signal variance due to non-Gaussian diffusion is characterized into two sources: isotropic variance arising from polydispersity in mean diffusivity, and anisotropic variance arising from microscopic anisotropy [75]; a general assumption underlying these techniques is that LTE signal depends on both isotropic and anisotropic variance while STE signals depend only on isotropic variance (i.e., time dependent diffusion and microscopic kurtosis are ignored). STE-based μ FA protocols use unique waveforms to acquire single-shot STE diffusion weighted signals [72], [76]. Though more TE-efficient than DDE, STE waveforms can potentially introduce time-dependent effects due to varying spectral content over the different gradient channels [76]. Furthermore, STE-based techniques assume that the dMRI signal contains only Gaussian compartments, which is an approximation that more advanced techniques like CTI avoid [94]. Some examples of techniques that use STE acquisitions to estimate μ FA and other parameters are the gamma signal representation, in which the inverse Laplace transform of the gamma distribution is fitted to powder averaged dMRI signals from LTE acquisitions and STE acquisitions [75], [114], and direct linear regression of the cumulant expansion of the diffusion signal [104], [115], [116].

The application of μ FA imaging to clinical research is appealing due to the unique insight it may provide into brain microstructure; for example, preliminary studies have found that μ FA can better distinguish between different types of brain tumors than FA and

other MRI metrics [75] and that it provides improved delineation of MS lesions over FA as well as unique contrast compared to T_1 - and T_2 -weighted imaging [74]. The parameter's insensitivity to orientation dispersion is advantageous over FA in the study or diagnosis of neuropathology in brain regions containing crossing or fanning fibers. However, μ FA generally requires long scan times that are not clinically feasible, especially when used in conjunction with other imaging techniques that are required in the clinical workflow. Other demonstrations of μ FA that have achieved shorter scan times did so at the cost of resolution [74], [117], producing μ FA maps with poorer resolution than typical FA maps acquired with DTI. To maximize scan efficiency, it is essential to understand the optimal parameters required to measure μ FA and use this information to design rapid protocols. To our knowledge, no comprehensive assessment of the optimal choices of b-value and relative numbers of LTE and STE acquisitions have been performed.

The aims of this work were to optimize a protocol for acquiring μ FA within a clinically viable scan time of <5 mins using the linear regression approach, and to demonstrate the feasibility of this method by comparing it to the highly cited gamma signal representation. We investigated the optimal b-values and ratio of STE to LTE acquisitions for the estimation of μ FA in white matter and combined these findings with two implementations of direct linear regression to enable the acquisition of full-brain, 2 mm isotropic resolution μ A and μ FA maps *in vivo* within a 3.3 min scan time and a 2-minute computation time. Estimates of μ FA using direct approaches strongly correlated with the gamma signal representation in white matter regions ($\rho \geq 0.9$), and all approaches exhibited high test-retest reliability ($\rho \geq 0.77$).

2.3. Theory

2.3.1. μ FA Estimation

The normalized signal intensity of powder-averaged dMRI acquisitions of a multi-component system, assuming negligible time-dependent diffusion, can be represented by the cumulant expansion [72]:

$$\ln\left(\frac{S}{S_0}\right) = -Db + \frac{\mu_2}{2}b^2 - \dots \quad (2.1)$$

where S is the powder-averaged signal, S_0 is the mean signal with no diffusion encoding, b is the b-value, D is the effective mean diffusivity, and μ_2 is the second central moment or variance of diffusivity. Lasic *et al* [72] define the microscopic fractional anisotropy in terms of the scaled difference in variance between powder-average LTE and STE acquisitions:

$$\mu_{FA} = \sqrt{\frac{3}{2}} \left(1 + \frac{2}{5} \frac{1}{\Delta\widetilde{\mu}_2}\right)^{-\frac{1}{2}} \quad (2.2)$$

$$\Delta\widetilde{\mu}_2 = \frac{\mu_2^{LTE} - \mu_2^{STE}}{D^2} \quad (2.3)$$

where μ_2^{LTE} and μ_2^{STE} are the second terms in the cumulant expansions of powder-averaged LTE and STE acquisitions, respectively. Using equation (2.1) up to the second cumulant term, the powder-averaged LTE and mean STE signals can be represented as:

$$S_{LTE} = S_0 e^{-Db + \frac{\mu_2^{LTE}}{2}b^2} \quad (2.4)$$

$$S_{STE} = S_0 e^{-Db + \frac{\mu_2^{STE}}{2}b^2} \quad (2.5)$$

If it is assumed that the only sources of kurtosis are dispersion in size and orientation of diffusion tensors, then the diffusion coefficient, D , will be equal between LTE and STE [75]. By assuming D is the same between LTE and STE signals acquired at the same b-

value, equations (2.4) and (2.5) can be substituted into equation (2.3) to provide an estimate of the scaled difference in variance that notably does not depend on the non-diffusion weighted signal S_0 :

$$\Delta\widetilde{\mu}_2 = \frac{2\ln(S_{LTE}/S_{STE})}{D^2b^2} \quad (2.6)$$

Substituting equation (2.6) into equation (2.2) provides an estimate of the μ FA [116]:

$$\mu FA = \sqrt{\frac{3}{2}} \left(1 + \frac{D^2b^2}{5 \ln\left(\frac{S_{LTE}}{S_{STE}}\right)} \right)^{-\frac{1}{2}} \quad (2.7)$$

Microscopic anisotropy is defined here based on the difference in signal between LTE and STE dMRI acquisitions, similar to the equation used in DDE protocols [108]:

$$\mu A = \sqrt{\frac{\ln\left(\frac{S_{LTE}}{S_{STE}}\right)}{b^2}} \quad (2.8)$$

By ignoring the third and higher order cumulant terms in deriving equations (2.4) and (2.5), μA can be estimated from a single b-shell, reducing scan time; however, ignoring the higher cumulants comes with the cost of potentially introducing a bias to the measurement [118]. μ FA can then be expressed in terms of μA by substituting equation (2.8) into equation (2.7):

$$\mu FA = \sqrt{\frac{3}{2} \frac{\mu A^2}{\mu A^2 + 0.2D^2}} \quad (2.9)$$

2.3.2. Diffusion Coefficient Estimation Using the Powder Average Diffusion Kurtosis Signal Representation

Explicitly enforcing that the diffusion coefficient D is the same between LTE and STE acquisitions causes the minimum number of powder-averaged samples required to estimate the four unknowns in equations (2.4) and (2.5), S_0 , D , μ_2^{LTE} and μ_2^{STE} , in a joint least squares

estimation to be only four (with at least one non-zero b-value sampled for each of LTE and STE). For example, a protocol could contain LTE and STE acquisitions at a single high b-value (e.g., 2000 s/mm²), plus either STE or LTE acquisitions at two smaller b-values (e.g., STE at b = 0 and STE at b = 1000 s/mm²). Contrary to previously proposed approaches, both STE and LTE would *not* be required in each shell using this joint estimation approach. Then, $\Delta\widetilde{\mu}_2$ could be estimated from μ_2^{LTE} and μ_2^{STE} using equations (2.3), and μ_{FA} estimated from equation (2.2). This approach will be referred to as “joint linear regression”. Alternatively, μA^2 could be estimated directly from the STE and LTE acquisitions at the highest b-value (e.g., 2000 s/mm²) using equation (2.8) while D could be estimated using a linear fit over the low b-values (e.g., LTE at b = 0 and LTE at b = 1000 s/mm²). Ignoring kurtosis in the estimation of D may introduce a bias, but this approach is computationally efficient which may improve clinical relevance. This will be referred to as “simplified regression”.

2.3.3. μA Optimization

To optimize a protocol for μA and μ_{FA} , sequence parameters that maximize the ratio of the mean measurement to its standard deviation can be evaluated, similar to the approach used to determine optimal parameters for diffusivity measurements [119]. Using standard error propagation [120], the signal-to-noise ratio (SNR) of μ_{FA} estimated using equation (2.9) can be related to the variance in μA^2 and D , with μ_{FA} image quality increasing with reduced variance in μA^2 and D measurements. It is expected that μA^2 will generally have much higher variance than D because it depends only on the highest b-shell data (equation (2.8)), which has the lowest SNR. Thus, we will focus on the optimization of μA^2 as a surrogate for the optimization of μ_{FA} . The SNR of a μA^2 image can be expressed as (Appendix A):

$$\frac{\mu A^2}{\sigma_{\mu A^2}} = \frac{\ln\left(\frac{S_{LTE}}{S_{STE}}\right) \sqrt{n_{LTE} n_{STE}} S_{LTE} S_{STE}}{\sigma \sqrt{n_{LTE} S_{LTE}^2 + n_{STE} S_{STE}^2}} \quad (2.10)$$

where n_{LTE} is the number of LTE directions acquired, n_{STE} is the number of STE averages acquired, S_{LTE} and S_{STE} are the powder-averaged signals of the LTE and STE images, respectively, and σ is the mean image noise. Given that $\frac{\mu A^2}{\sigma_{\mu A^2}}$ is maximized when $\frac{n_{STE}}{n_{LTE}} = \frac{S_{LTE}}{S_{STE}}$ (see Appendix A), and that S_{LTE} and S_{STE} are dependent on b-value, the optimal protocol parameters (b and $\frac{n_{STE}}{n_{LTE}}$) can be determined using equation (2.10).

Equations (2.4) and (2.5) can be substituted into equation (2.10), and assuming all STE and LTE acquisitions are performed with the same TE:

$$\begin{aligned} & \frac{\mu A^2}{\sigma_{\mu A^2}} \quad (2.11) \\ & = e^{-\frac{2TE(b)}{T_2}} \frac{b^2 \sqrt{n_{LTE} n_{STE}} \left(\frac{\mu_2^{LTE} - \mu_2^{STE}}{2} \right) \left(e^{-2Db + b^2 \left(\frac{\mu_2^{LTE} + \mu_2^{STE}}{2} \right)} \right)}{\sigma \sqrt{\left(n_{LTE} \right) e^{-2Db + b^2 (\mu_2^{LTE})} + \left(n_{STE} \right) e^{-2Db + b^2 (\mu_2^{STE})}} \end{aligned}$$

Equation (2.11) reveals that the SNR depends on TE(b) by an exponential prefactor. Note that the TE is a function of the b-value, as higher b-value acquisitions will require longer TEs.

2.4. Methods

Two sets of MRI scans were performed on two sets of volunteers for this work. The study was approved by the Institutional Review Board at Western University and informed consent was obtained from each volunteer prior to scanning. The first set of scans consisted of LTE and STE acquisitions over a wide range of b-values and was acquired to provide the signal data needed to optimize μA using equation (2.10). The second set of scans

performed test-retest measurements with a comprehensive sequence that allowed for μ FA mapping using the gamma signal representation, joint linear regression, and simplified linear regression. The various dMRI sequences and data subsets are summarized in Table 2.1 and are described in detail below.

Table 2-1: Summary of MRI sequences and data subsets for in vivo acquisitions.

	Sequence optimization	Comprehensive
TE/TR (ms)	125/8700	94/4500
Slices	45 axial	48 axial
Parallel Imaging	R = 2 in-plane	R = 2 in-plane, 2 SMS (4 total)
Resolution (mm ³)	2 x 2 x 2	2 x 2 x 2
Diffusion scheme	0 s/mm ² (6 LTE)	0 s/mm ² (5 LTE)
	500 s/mm ² (6 LTE + 6 STE)	100 s/mm ² (3 LTE + 6 STE)
	1000 s/mm ² (6 LTE + 6 STE)	700 s/mm ² (3 LTE + 6 STE)
	1500 s/mm ² (6 LTE + 6 STE)	1000 s/mm ² (15 LTE + 10 STE)
	2000 s/mm ² (6 LTE + 6 STE)	
	2500 s/mm ² (6 LTE + 6 STE)	1400 s/mm ² (6 LTE + 10 STE)
	3000 s/mm ² (6 LTE + 6 STE)	2000 s/mm ² (22 LTE + 27 STE)
	3500 s/mm ² (6 LTE + 6 STE)	
Data subsets		
Optimization validation (no denoising)	-	<p>Suboptimal subset</p> <p>100 s/mm² (3 LTE + 6 STE)</p> <p>700 s/mm² (3 LTE + 6 STE)</p> <p>1400 s/mm² (6 LTE + 10 STE)</p> <p>2000 s/mm² (16 LTE + 6 STE)</p> <p>Standard subset</p> <p>100 s/mm² (3 LTE + 6 STE)</p> <p>700 s/mm² (3 LTE + 6 STE)</p> <p>1400 s/mm² (6 LTE + 10 STE)</p> <p>2000 s/mm² (6 LTE + 16 STE)</p>
Model comparisons (denoised)	-	<p>Standard subset</p> <p><i>*Same as standard subset above</i></p> <p>Simplified subset</p> <p>100 s/mm² (3 LTE)</p> <p>1000 s/mm² (15 LTE)</p> <p>2000 s/mm² (16 LTE + 22 STE)</p>

Minimalistic sequence (denoised)	-	100 s/mm ² (3 STE) 1000 s/mm ² (6 STE) 2000 s/mm ² (16 LTE + 18 STE)
-------------------------------------	---	--

2.4.1. Sequence Optimization

MRI scans were performed in 4 healthy volunteers (2 female and 2 male, mean age 22.4 ± 1.7 years) on a 3T Prisma whole-body MR system (Siemens Healthineers) with 80 mT/m strength and 200 T/m/s slew rate. Multiple b-shell diffusion data were acquired in a single scan using LTE and STE sequences: 6 image volumes were acquired at $b = 0$ s/mm², and 6 LTE directions and 6 STE averages were acquired at b-values between 500 and 3500 s/mm², in increments of 500 s/mm². The STE sequence was designed to avoid net phase accumulation from concomitant fields by using trapezoidal gradient schemes that are symmetric about a 180° pulse (Figure 2-1) [112], while a standard pulsed gradient spin echo sequence was used for LTE acquisitions [46]. The other parameters were TE/TR = 125/8700 ms, FOV = 192x192 mm², 2 mm isotropic resolution, 45 slices, rate 2 GRAPPA, 2 averages, and total scan time = 29 minutes. Images were processed using Gibbs ringing correction and Eddy current correction with FSL *eddy* [121].

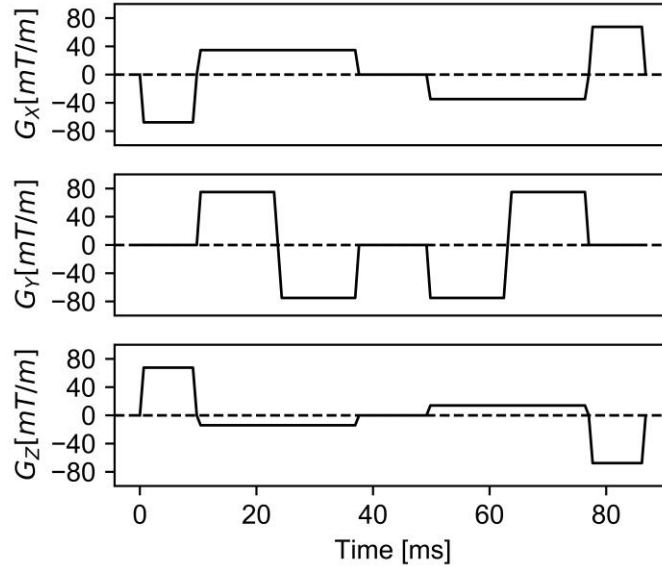


Figure 2-1. Schematic representation of the spherical tensor encoding gradient waveforms. Diffusion encoding blocks have been inserted on both sides of a 180° pulse in all three gradient directions to acquire an STE diffusion MRI signal. Implicit gradient reversal due to the 180° pulse has been applied.

A region of interest (ROI) across multiple slices was manually selected in the frontal WM for each patient and used to measure the mean LTE signal and mean STE signal at each b-value. A joint regression was performed on the mean LTE and STE signal data to fit the curves to equation (2.1) up to the third cumulant, with the assumption that D is the same in LTE and STE acquisitions. The best-fit cumulant expansions for each of the 4 volunteers were averaged and used together with equation (2.10) to determine the optimal b-value and optimal ratio of LTE to STE acquisitions in a μ A protocol. In evaluation of equation (2.10), the T_2 decay constant was assumed to be 80 ms to approximate WM at 3T [122]. These SNR calculations assume the same total number of acquisitions at each b-value, with only the ratio of $\frac{n_{STE}}{n_{LTE}}$ acquisitions changing.

2.4.2. Comprehensive Acquisitions

A comprehensive 113 acquisition dMRI protocol was used to acquire the data to compare μ F_A volumes generated with different methods. 4 healthy volunteers (2 female and 2 male, mean age 28.0 ± 6.6 years) were imaged at 3T with a 9-minute dMRI scan with TE/TR = 94/4500 ms. The scan consisted of 3, 3, 15, 6, and 22 LTE directions and 6, 6, 10, 10, and 27 STE averages at $b = 100, 700, 1000, 1400,$ and 2000 s/mm^2 , respectively, as well as 5 averages at $b = 0 \text{ s/mm}^2$. These directions were chosen to enable retrospective splitting of the data into the subsets described below. The other parameters were FOV = 220x220 mm², 2 mm isotropic resolution, 48 slices, and rate 2 in-plane parallel imaging combined with rate 2 simultaneous multislice (SMS). Volunteers were also scanned using T_1 -weighted MPRAGE with 1 mm isotropic resolution. After removing each volunteer from the MR scanner for a period of 5-10 minutes, a repeat measurement was performed using only the dMRI protocol. Data from these acquisitions is available online [dataset] [123].

Two separate post-processing pipelines were performed on the data to acquire two different data sets: a “noisy” data set that omitted denoising to test the effects of using an optimized vs. suboptimal ratio of STE to LTE scans to compute μ A, since denoising is a non-linear operation that invalidates the assumptions used in the derivation of equation (2.10), and a denoised data set to compare the μ F_A approaches described in this work to the gamma representation. All the diffusion MRI data was processed using Gibbs ringing correction and FSL *eddy* [121], and PCA denoising [124] was performed prior to these corrections for the denoised data set.

The T_1 -weighted anatomical volumes were segmented into WM and gray matter (GM) masks using FMRIB’s Automated Segmentation Tool (*fast*) [125] and were registered to the denoised dMRI volumes using symmetric diffeomorphic and affine

transforms with ANTS software (<https://github.com/ANTsX/ANTs>) [126]. The retest noisy and denoised volumes were also registered to the respective test volumes using a rigid transform with ANTS.

To validate equation (2.10), the noisy dMRI data was split into two 56-acquisition subsets to represent a standard protocol that approximately complies with our optimization results and a suboptimal protocol that does not comply. The standard protocol was based on a rapid sequence proposed by Nilsson *et al* [117] and included 3, 3, 6, and 6 LTE directions and 6, 6, 10, and 16 STE averages at $b = 100, 700, 1400, \text{ and } 2000 \text{ s/mm}^2$. The suboptimal protocol consisted of the same acquisitions with one exception: the ratio $\frac{n_{STE}}{n_{LTE}}$ at the $b = 2000 \text{ s/mm}^2$ shell was 6/16 instead of 16/6, a suboptimal ratio. The 6 direction subset of LTE acquisitions used an icosahedral sampling scheme [117], and the 16 direction subset was distributed using electrostatic repulsion [127]. Notably, no denoising was applied to these data subsets.

To compare linear regression to the gamma representation, the denoised dMRI data was split into two subsets with each containing 56 acquisitions. The standard subset, to be used to compare the gamma signal representation versus joint linear regression, used the rapid sequence by Nilsson *et al* described above [117]. An additional subset, referred to herein as the “simplified subset”, included 22 STE averages at $b = 2000 \text{ s/mm}^2$ and 3, 15, and 16 LTE directions at $b = 100, 1000, \text{ and } 2000 \text{ s/mm}^2$ (56 total acquisitions), and was designed to investigate whether a single b-shell to compute μA^2 ($b = 2000 \text{ s/mm}^2$) can be added to a DTI acquisition ($b = 100, 1000 \text{ s/mm}^2$) to enable μFA imaging using the simplified regression approach. The $b = 1000$ and 2000 s/mm^2 LTE shells were determined separately from each other using electrostatic repulsion.

An additional subset of the comprehensive scan containing 43 acquisitions was used to demonstrate the potential scan time advantage of the linear regression technique. This “minimalistic subset” contained 16 LTE directions at $b = 2000 \text{ s/mm}^2$ and 3, 6, and 18 STE averages at $b = 100, 1000, \text{ and } 2000 \text{ s/mm}^2$, respectively, and would have required only 3.3 minutes of scan time.

2.4.3. Analysis

To validate equation (2.10), the SNR of μA^2 was compared between the standard and suboptimal subsets of the noisy dMRI data by first estimating μA^2 at $b = 2000 \text{ s/mm}^2$ in both the test and retest volumes for each volunteer. Then, the test-retest coefficients of variance (CoVs) of the standard and suboptimal volumes across all volunteers were compared as a surrogate of SNR.

For signal representation comparisons with the denoised data, the powder-averaged STE and LTE signals vs. b-value were fitted to the diffusion kurtosis signal representation using a joint non-negative least squares method assuming consistent D between STE and LTE, and μFA was computed using equation (2.2) ($\mu \text{FA}_{\text{joint}}$). μFA was also estimated using Nilsson *et al*'s Multidimensional diffusion MRI software [128] (<https://github.com/markus-nilsson/md-dmri>) to fit the diffusion-weighted signals to the gamma representation ($\mu \text{FA}_{\text{gamma}}$). μFA maps were generated for each volunteer using these two methods in the standard subset of data.

Additionally, μFA was estimated using equation (2.9) in the simplified subset by decoupling μA^2 and D ($\mu \text{FA}_{\text{simp}}$): μA^2 was estimated at $b = 2000 \text{ s/mm}^2$ using the direct cumulant method (equation (2.8)) while D was estimated by fitting the $b = 100$ and 1000 s/mm^2 LTE data to the DTI signal representation using FMRIB's DTIFIT tool.

The μ FA maps from the different methods and subsets were then compared in WM using Bland-Altman plots and voxelwise scatter plots, and Pearson correlation coefficients were computed between each technique. To test the repeatability of the measurement techniques, Bland-Altman plots were generated for each patient to compare the initial and repeat μ FA volumes and Pearson correlation coefficients were computed between initial and repeat μ FA maps.

The minimalistic subsets were used to generate full-brain μ FA maps using the joint regression approach, and the repeatability of this measurement technique was assessed using the methods described above. The maps generated using these subsets were not compared to the gamma representation as they contained too few b-shells for gamma fitting.

2.5. Results

2.5.1. Sequence Optimization

The logarithm of the powder-averaged WM dMRI signal as a function of b-value, averaged across all volunteers, is shown in Figure 2-2. As expected [75], the departure from monoexponential signal decay was greater in the LTE than STE signal curve due to the mesoscopic orientation of tensors. Figure 2-3 shows the variation in $\mu A^2/\sigma_{\mu A^2}$ with b-value and the ratio of $\frac{n_{STE}}{n_{LTE}}$ assuming a fixed total number of acquisitions ($n_{STE} + n_{LTE}$). For any given b-value, the optimal $\frac{n_{STE}}{n_{LTE}}$ was computed to be equal to the ratio of the powder averaged signals, $\frac{S_{LTE}}{S_{STE}}$, at said b-shell. The highest $\frac{\mu A^2}{\sigma_{\mu A^2}}$ occurred when the b-value was 2000 s/mm², for which the optimal $\frac{n_{STE}}{n_{LTE}}$ was approximately 1.7. However, a wide range of dMRI parameter configurations yielded an SNR above 95% of the optimal parameters for μA^2 SNR.

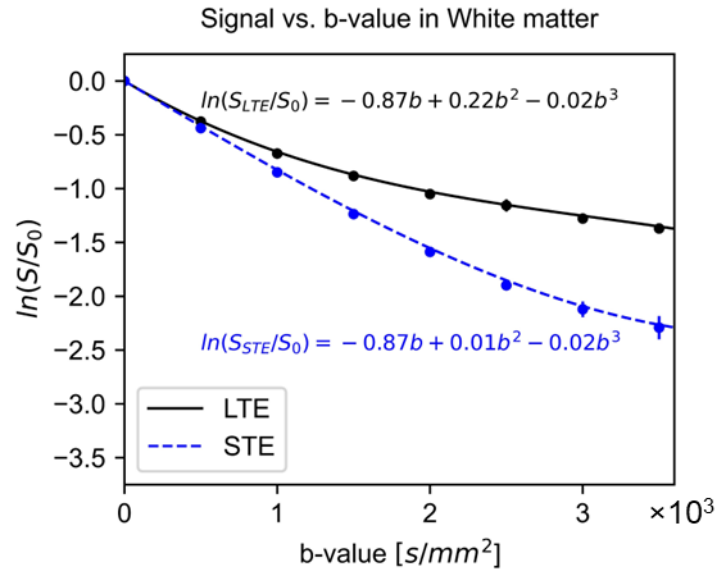


Figure 2-2. Logarithm of the diffusion MRI signal vs. b-value in frontal white matter. The plot shows the powder-averaged signal from a manually prescribed region of interest across four volunteers as measured with linear tensor encoding and spherical tensor encoding (black and blue circles, respectively), while the dashed lines show the third order cumulant fit. Also depicted are the standard deviations across the volunteers.

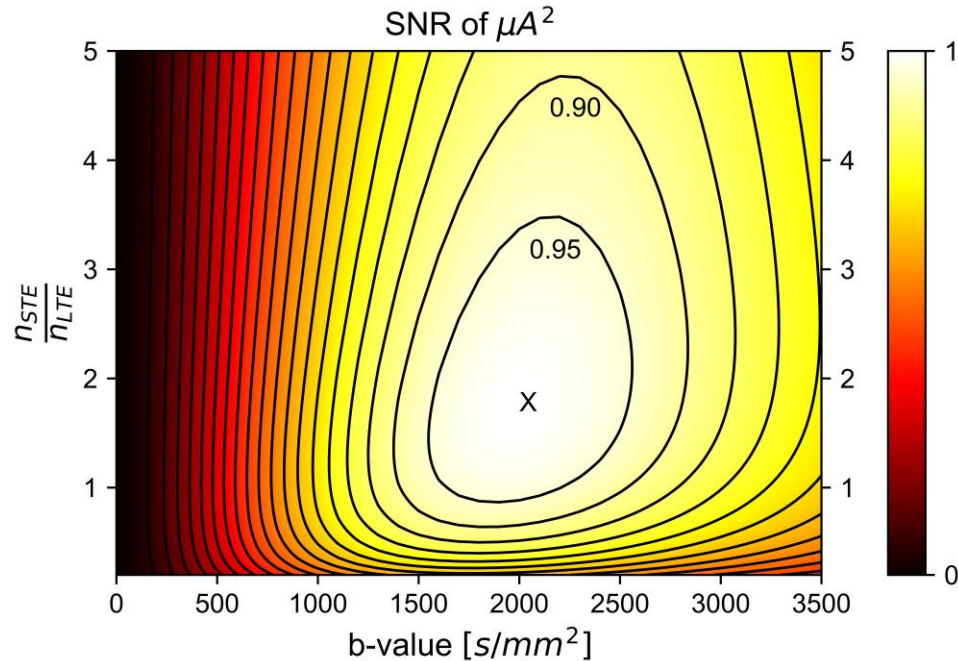


Figure 2-3. Simulated μA^2 SNR in white matter as a function of the b-value and the ratio of STE to LTE acquisitions (n_{STE}/n_{LTE}). Though the maximum SNR occurred when $b = 2000$ s/mm^2 and $n_{STE}/n_{LTE} = 1.7$ (marked by an 'X'), a wide range of parameters yielded SNRs greater than 95% of the maximum SNR, suggesting that there is flexibility in parameter choice when designing a protocol. Notably, a significant drop off in SNR occurred for $n_{STE}/n_{LTE} < 1$, suggesting that image quality is maximized when the number of STE acquisitions is greater than or equal to the number of LTE acquisitions.

A significant drop off in SNR occurred for $\frac{n_{STE}}{n_{LTE}} < 1$, suggesting that image quality is maximized when the number of STE acquisitions is greater than or equal to the number of LTE acquisitions. The suboptimal dataset is located in this region where the SNR sharply decreases, while the standard data set is in the high SNR region that varies slowly. Using the powder averaged STE and LTE WM signal data from the noisy data subset at $b = 2000$ s/mm^2 across all volunteers along with equation (2.10), the SNR of μA^2 in the suboptimal subset was predicted to be 87% of the SNR of μA^2 in the standard subset. Analysis of the test and retest μA^2 volumes revealed a CoV of 22.94% in the standard measurement and a

CoV of 25.78% in the suboptimal measurement, yielding an experimentally acquired SNR ratio of approximately 89% (since CoV is analogous to SNR^{-1}) which is comparable to the value of 87% predicted by equation (2.10). Example μA^2 images estimated using the standard and suboptimal subsets are depicted in Figure 2-4.

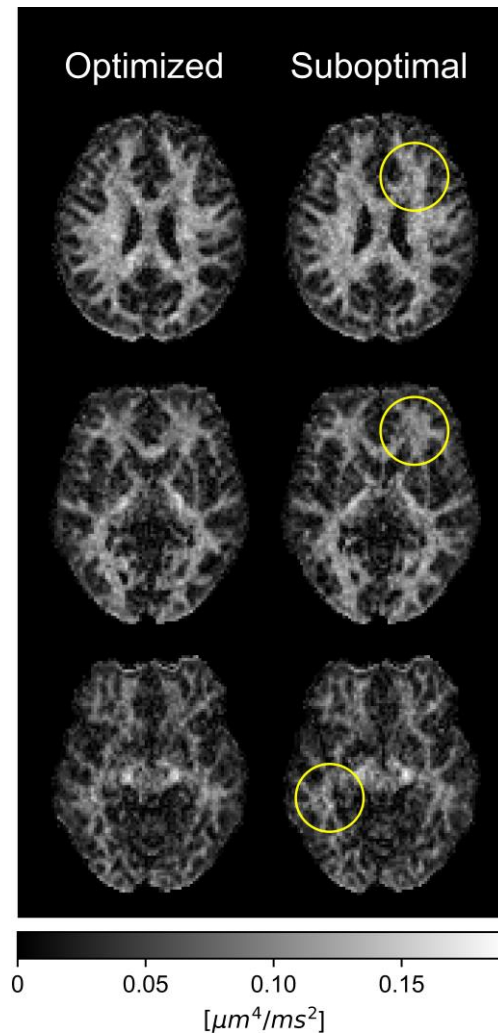


Figure 2-4. Example μA^2 images acquired with the standard (left) and suboptimal (right) subsets of the data without denoising. Lower image quality is observed in the right case, with some irregular features highlighted by the yellow circles. Images were acquired with rate 2 in-plane parallel imaging combined with rate 2 simultaneous multislice.

2.5.2. Comparison Between Different μ FA Techniques

Example μ FA_{gamma} and μ FA_{joint} maps computed from the standard subset, as well as μ FA_{simp} maps computed from the DTI subset, are depicted in Figure 2-5. μ FA was observed to be qualitatively consistent across the different techniques and data subsets and image quality was comparable between them. Notably, μ FA and μ A were observed to be negligible in regions containing only CSF, such as in the lateral ventricles, where diffusion is expected to be isotropic.

Scatter plots and Bland-Altman plots comparing WM μ FA using the three different estimation approaches in all volunteers are presented in Figure 2-6. Strong linear correlations were observed in the scatter plots comparing each volume, with respective Pearson correlation coefficients of 0.97 (μ FA_{gamma} vs. μ FA_{joint}), 0.90 (μ FA_{gamma} vs. μ FA_{simp}), and 0.90 (μ FA_{joint} vs. μ FA_{simp}). Relative to μ FA_{gamma}, the mean WM biases in the other volumes were -0.11 (μ FA_{joint}) and -0.02 (μ FA_{simp}).

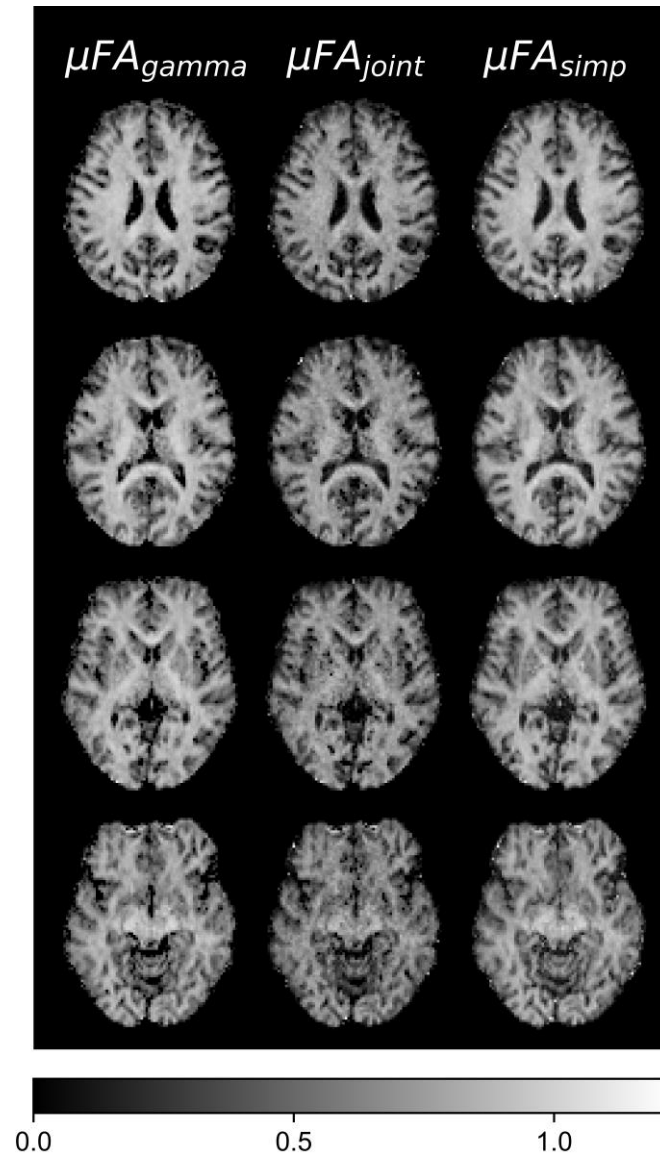


Figure 2-5. Example μFA images from one volunteer. Images were acquired using the gamma signal representation with the standard subset (left), joint linear regression with the standard subset (center), and simplified linear regression (i.e., D computed from DTI using only b-values of 100 and 1000 s/mm^2) (right). Comparable image quality is observed for the three methods. Images were acquired with rate 2 in-plane parallel imaging combined with rate 2 simultaneous multislice.

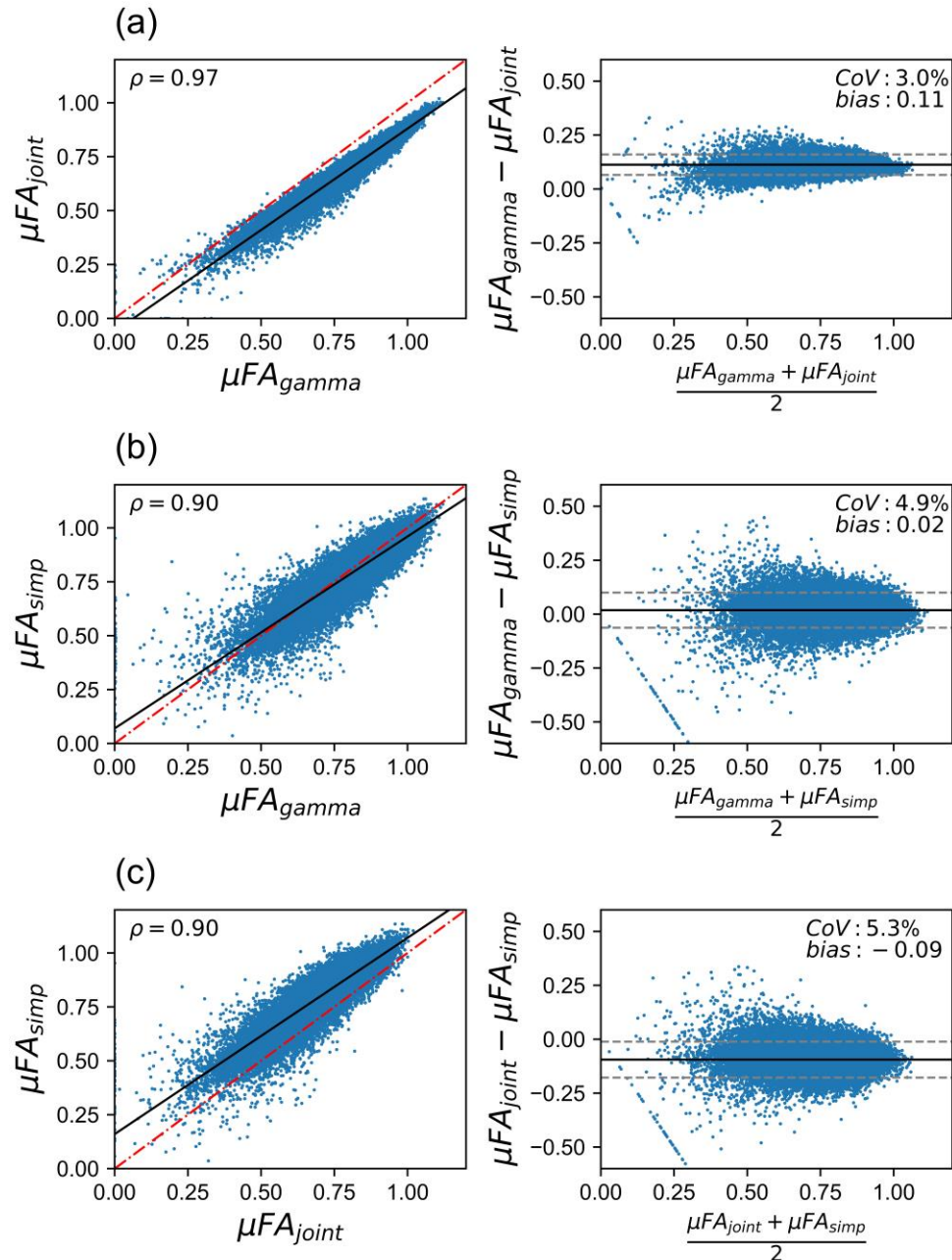


Figure 2-6. Voxelwise correlations between μFA estimates acquired using different techniques in white matter (left) and Bland-Altman plots depicting biases between the methods in white matter (right): (a) $\mu\text{FA}_{\text{gamma}}$ vs. $\mu\text{FA}_{\text{joint}}$, (b) $\mu\text{FA}_{\text{gamma}}$ vs. $\mu\text{FA}_{\text{simp}}$, and (c) $\mu\text{FA}_{\text{joint}}$ vs. $\mu\text{FA}_{\text{simp}}$. The dashed red line and solid black line in each of the scatter plots represent the identity and regression lines, respectively. The solid black line in the Bland-Altman plots represents the mean bias, and the dashed grey lines represent the ± 1.96 standard deviation lines.

2.5.3. Analysis of Repeatability

Bland-Altman plots comparing the test and retest μ FA volumes across all volunteers revealed no biases in repeat measurements (Figure 2-7). The Pearson correlation coefficients between the test and retest μ FA maps were 0.83 (μ FA_{gamma}), 0.79 (μ FA_{joint}), and 0.84 (μ FA_{simp}).

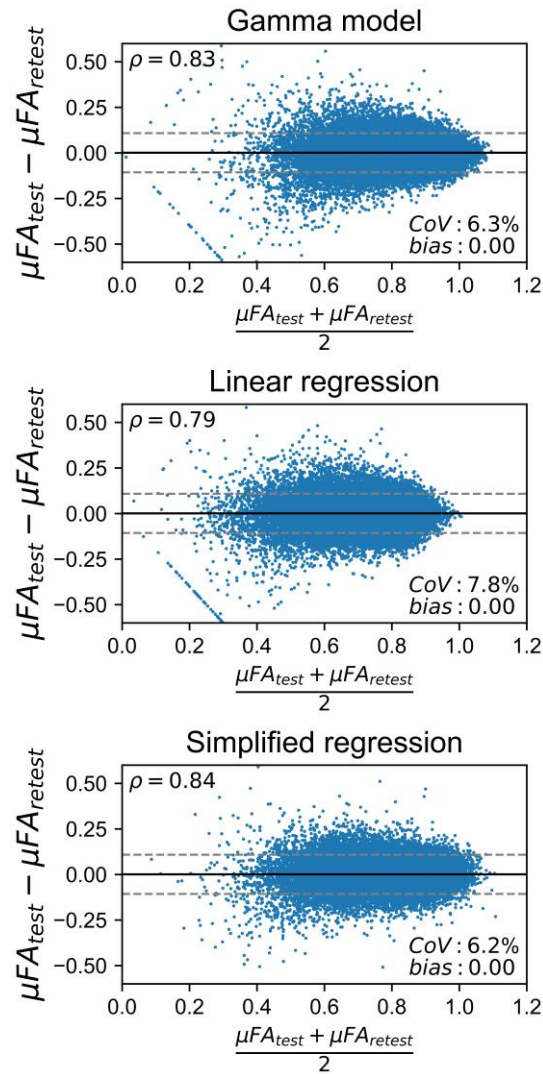


Figure 2-7. Bland-Altman plots assessing the test-retest reliability of μ FA estimates acquired using different techniques in white matter. The solid black line represents the mean bias, and the dashed grey lines represent the ± 1.96 standard deviation lines.

2.5.4. Minimalistic Sequence

Sample μ FA, μA^2 , and LTE and STE variance maps generated using the minimalistic data subsets are depicted in Figure 2-8. Bland-Altman plots comparing the test and retest volumes (not depicted) revealed no biases between the measurements, a CoV of 5%, and a Pearson correlation coefficient of 0.77, demonstrating strong evidence of repeat measurement reliability.

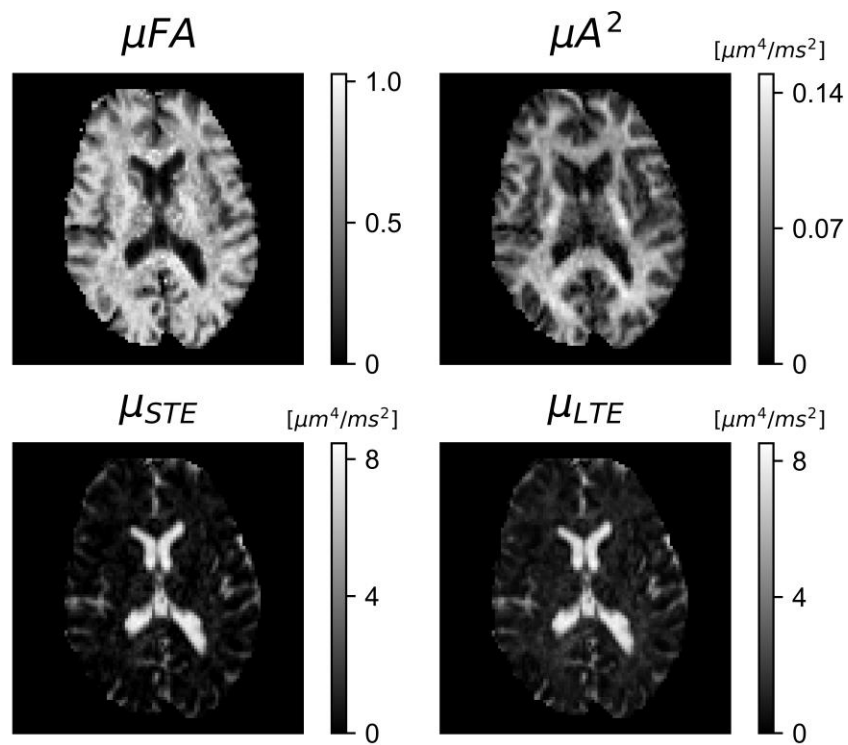


Figure 2-8. Example μ FA, μA^2 , and LTE and STE variance maps acquired using equation 2.2 in a subsampled data set: The acquisition comprised of 16 LTE directions at $b = 2000 \text{ s/mm}^2$ and 3, 6, and 18 STE directions at $b = 100, 1000, \text{ and } 2000 \text{ s/mm}^2$, respectively. This direction scheme corresponds to a total scan time of approximately 3.3 min with $220 \text{ mm} \times 220 \text{ mm} \times 96 \text{ mm}$ coverage at an isotropic 2 mm resolution. All images were normalized to a maximum pixel value of 1. Images were acquired with rate 2 in-plane parallel imaging combined with rate 2 simultaneous multislice.

2.6. Discussion

Microscopic anisotropy mapping has been gaining popularity in neuroimaging studies because it provides a marker of tissue microstructure independent of orientation dispersion. The aims of this work were two-fold: (1) to determine the optimal dMRI parameters (b-value and $\frac{n_{STE}}{n_{LTE}}$) needed to maximize image quality for a given scan time or number of acquisitions and use this information to design a rapid protocol with <5 minute scan time, and (2) to compare the linear regression-based μ FA techniques described in this work against the gamma signal representation. The first aim was achieved by directly estimating μA^2 from the cumulant expansion of powder-averaged LTE and STE acquisitions and then estimating the SNR of μA^2 using standard error propagation theory. The optimal b-value of 2000 s/mm² falls within the optimal range for DDE methods; Ianus *et al* found that b-values between 2000 and 3000 s/mm² are optimal for single-shell DDE estimations of μA because lower b-values result in noisy images while higher b-values result in large biases [108]. The optimal $\frac{n_{STE}}{n_{LTE}}$ is somewhat intuitive as STE images typically have lower SNR than LTE images due to the more rapid signal decrease with b-value. Notably, a steep drop-off in SNR with $\frac{n_{STE}}{n_{LTE}}$ ratios below 1 was observed. These optimization findings were validated by the test-retest CoV ratio between the standard and suboptimal data sets agreeing with the SNR ratio predicted by equation (2.10). Notably, these findings are complementary to recommendations for the minimal number of LTE directions to avoid rotational variance [129] and for optimized STE waveforms to minimize the TE [130]. The second aim was achieved by acquiring all the data necessary for all the different μ FA volumes in a single acquisition, mapping μ FA from different subsets of data, and performing voxelwise comparisons on the maps. Notably, the linear regression approaches

yielded comparable reliability and strong correspondence with the gamma method when a maximum b-value of 2000 s/mm² was used.

The μ FA imaging techniques proposed in this work are suitable for use in clinical research due to the relatively minimalistic acquisition protocols needed to estimate μA^2 and μ FA. Furthermore, μ FA computation time in the standard subset only took approximately 2 minutes per volume using joint regression (on a standard personal computer) and was virtually instantaneous for simplified regression. When designing a rapid protocol to acquire μ FA images using linear regression, the authors recommend using the following steps: (1) acquire enough LTE acquisitions at the highest b-value (e.g. 2000 s/mm²) to ensure rotational invariance in the powder-averaged signal [129], (2) acquire as many STE acquisitions as possible within the scan time limitation to bring the ratio of $\frac{n_{STE}}{n_{LTE}}$ as close to the optimal value (1.7 in this work) as possible, without going below $\frac{n_{STE}}{n_{LTE}} = 1$ to avoid sharply decreasing SNR (Figure 2-3), and (3) acquire STE acquisitions at 2-3 lower b-shells for curve fitting. The minimalistic sequence serves as an example of how this procedure can be used to develop a rapid imaging protocol. In designing this protocol, we first decided to include 16 LTE acquisitions at $b = 2000$ s/mm² to ensure rotational invariance. Next, we opted for 18 STE acquisitions at $b = 2000$ s/mm² to achieve an $\frac{n_{STE}}{n_{LTE}}$ ratio of 1.125. Finally, we included 3 and 6 STE acquisitions at $b = 100$ and 1000 s/mm², respectively, for curve fitting, which resulted in a total acquisition time under 3.3 minutes. Note that post-processing was performed on this subset after separating it from the rest of the data. Notably, if the number of slices, resolution, and use of parallel imaging for this protocol was set to be the same as the rapid protocol proposed by Nilsson *et al* that required 3 minutes [117], the scan time would have been 2.3 min. Additionally, the joint regression

approach requires fewer low b-value acquisitions, which allows for more LTE directions at the highest b-value and potentially results in less error from rotational variance [129]. Nevertheless, this protocol demonstrates that the LTE variance can be estimated from a set of data containing only one LTE shell and three STE shells when D is assumed to be the same between LTE and STE acquisitions.

In this study, biases were observed in the μFA WM maps relative to the measurements produced by the gamma signal representation. The $\mu\text{FA}_{\text{joint}}$ metric had a mean bias of -0.11 compared to $\mu\text{FA}_{\text{gamma}}$, while the $\mu\text{FA}_{\text{simp}}$ metric was biased against $\mu\text{FA}_{\text{gamma}}$ by a modest -0.02. We suspect that the most likely causes of this discrepancy between the techniques are the differences between the signal representations used to fit the data: the implementation of the gamma signal representation used in this work utilizes a soft Heaviside function to constrain the fit to use the lower b-values more heavily, similar to the DTI fit for D in $\mu\text{FA}_{\text{simp}}$. Accordingly, strong correspondence was observed between $\mu\text{FA}_{\text{gamma}}$ and $\mu\text{FA}_{\text{simp}}$. Using a joint cumulant fit to estimate D resulted in lower μFA values in the $\mu\text{FA}_{\text{joint}}$ volume, which reveals a potential bias in the other two methods that results in physically implausible μFA values that are greater than 1 (see Figure 2-7). That said, μFA computed from the equation (2.2) approach could also be biased to lower values because the cumulant expansions of the powder-averaged signals were limited to the second order (equations (2.4) and (2.5)), ignoring the effects of higher order terms. Using the mean WM signal data across all volunteers from the sequence optimization dataset (Table 2-1, Figure 2-2) revealed that the second order cumulant fit using b-values up to 2000 s/mm² underestimated μFA by up to 9.3% compared to a third order fit using b-values up to 3500 s/mm². A previous study that used DDE to estimate μA at a single b-value in

six different microstructural models [108] reported an underestimation of the metric when acquired at a single b-shell; to remove this bias, the use of a multiple b-shell approach utilizing a higher order cumulant expansion of the dMRI signal can be considered.

Qualitatively, the biases between the different volumes did not have a significant impact on the images as contrast between structures or regions and image quality appeared similar in all the maps. Additionally, voxelwise comparisons between the maps showed strong linear relationships in WM regions, evidence that the biases between the different techniques are likely scalar or constant. We propose that each of the techniques described in this work may be suitable for use in clinical research under the caveat that studies assessing multiple patients or assessing patients longitudinally should use the same protocol and technique to avoid biases.

There are several limitations potentially affecting the accuracy of this study. The STE sequence used in this work utilizes different gradient waveforms in each diffusion-encoding direction, probing each at slightly different diffusion times and over different trajectories in q-space and potentially giving rise to orientational biases [93]. Given the small microstructural length scales in WM ($<10\ \mu\text{m}$), the long diffusion time regime is likely an appropriate assumption for all 3 waveforms, though future studies may still wish to powder average STE data acquired using different gradient directions. This potential bias is not expected to have impacted our optimization findings or comparisons between regression and the gamma signal representation because they all used identical waveforms. Also, a slightly reduced minimum TE could likely have been achieved with optimized STE waveforms [130], but we implemented a simpler version that can be easily computed online

on the scanner. While this may have a slight impact on the optimal b-value, the optimal ratio of STE to LTE acquisitions had no dependence on TE.

A relatively low number of LTE directions were acquired at $b = 2000 \text{ s/mm}^2$ in the standard data subsets, which may have slightly reduced the accuracy of the measurements by introducing a directional dependence to the powder-averaged signal [117]. This would not have affected comparisons between $\mu\text{FA}_{\text{joint}}$ and $\mu\text{FA}_{\text{gamma}}$, but the $\mu\text{FA}_{\text{simp}}$ volume was computed with more acquisitions at $b = 2000 \text{ s/mm}^2$, which may have slightly advantaged measurements of reliability from that volume against the others.

The regression technique described herein makes the assumption that the dMRI signal arises only from multiple Gaussian components, which is violated when time-dependent diffusion is not negligible or when microscopic kurtosis is non-vanishing [93]. This potential confound may warrant the use of advanced techniques such as CTI, even at the expense of a longer TE, to yield μFA estimations without these assumptions [94].

2.7. Conclusions

In conclusion, we have demonstrated an optimized linear regression technique based on the diffusion kurtosis signal representation that enabled full-brain mapping of μFA in a clinically relevant 3.3 min scan time at 3T. Two implementations of the proposed direct approach were validated against the gamma signal representation, and an approach to determine the optimal maximum b-value and ratio of STE to LTE acquisitions was proposed and validated. Though additional work is necessary to establish the roles of μA and μFA imaging in clinical research settings, the ability to rapidly probe these measurements *in vivo* opens the door for exploration into their abilities to assess neurodegeneration and other pathologies.

In Chapter 2, a technique to estimate μ FA was developed and optimized, then tested to ensure good repeat measurement reliability. Though μ FA solves the issue of neurite fiber orientation confounding dMRI measurements, it remains susceptible to free water partial volume effects. Chapter 3 presents a technique to mitigate these effects to acquire tissue-specific measurements using a two-compartment signal representation known as the free water elimination powder kurtosis representation.

Chapter 3

3 Estimation of Free Water-Corrected Microscopic Fractional Anisotropy

3.1. Overview

This chapter was published in *Frontiers in Neuroscience*, volume 17, *Estimation of Free Water-Corrected Microscopic Fractional Anisotropy* [131], 2023.

3.2. Introduction

Diffusion-weighted MRI (dMRI) is a non-invasive imaging modality that uses specialized pulse sequences to sensitize the MRI signal to the random molecular motion of water [46], [82]. On MRI-relevant time frames, water molecules traverse microscopic length scales in tissue, and their diffusion is dictated by the presence of restricting boundaries such as cell membranes and other structures. By exploiting the known relationships between dMRI signal and tissue properties, dMRI measurements can act as surrogate indicators of physical properties of neural tissue, and this capability has led to dMRI finding use in the study of neurological disorders like multiple sclerosis [56], [83], Alzheimer's disease [84], and stroke [85], among others.

The most widely used dMRI technique is diffusion tensor imaging (DTI). DTI is based on the first order cumulant expansion of the logarithm of the dMRI signal as a function of diffusion weighting or b-value [86], [88], which can be represented by the equation:

$$S_{g,b} = S_0 e^{-b \sum_{i,j=1}^3 g_i g_j D_{ij}} \quad (3.1)$$

where $S_{g,b}$ is the dMRI signal of a particular acquisition acquired with diffusion-weighting applied in the direction of the unit vector $\mathbf{g} = (g_1, g_2, g_3)$, S_0 is the MRI signal in the

absence of diffusion weighting, b is the b-value, which describes the strength of the diffusion weighting, and D_{ij} is ij^{th} element of the fully symmetric second order diffusion tensor, \mathbf{D} . DTI requires linear tensor encoding (LTE) acquisitions in different diffusion directions at a single b-value plus one or more acquisitions with no diffusion weighting and can report metrics such as the mean diffusivity (MD) and fractional anisotropy (FA) of water diffusion. However, the DTI representation assumes that diffusion follows a mono-Gaussian distribution, which is a reasonable assumption only at low b-values [132]. The diffusion kurtosis imaging (DKI) representation further expands the cumulant expansion of the logarithm of the dMRI signal to the second order to account for non-Gaussian diffusion but requires the acquisition of dMRI data at two or more b-values. The DKI signal representation can be represented as [62], [66]:

$$S_{\mathbf{g},b} = S_0 e^{-b \sum_{i,j=1}^3 g_i g_j D_{ij} + \frac{1}{6} b^2 \sum_{i,j,k,l=1}^3 g_i g_j g_k g_l W_{ijkl} + O(b^3)} \quad (3.2)$$

where W_{ijkl} denotes the $ijkl^{th}$ element of the fully symmetric fourth order diffusion kurtosis tensor, \mathbf{W} , and $O(b^3)$ is a higher order term that is negligible in brain tissue at b-values lower than 3000s/mm^2 [133]. The powder kurtosis signal representation (paK), in which data acquired from many diffusion directions are arithmetically averaged into a single image volume known as the powder average, can be represented as:

$$S_b = S_0 e^{-b D_{eff} + \frac{1}{6} b^2 D_{eff}^2 K + O(b^3)} \quad (3.3)$$

where S_b is the dMRI signal of the powder averaged data at a particular b-value, D_{eff} is the effective diffusivity estimated from the powder average signals, and K is the effective diffusion kurtosis [62], [66]. Note that diffusion metrics acquired from the powder

representation (e.g. D_{eff}) differ from similarly-named metrics acquired from the tensor representation (e.g. MD) [134].

The DTI and DKI representations are limited by two major factors that affect their specificity to neuronal microstructure: (1) the tensors used to estimate anisotropy are sensitive to neuron fiber orientation dispersion within the voxel, causing FA to be reduced in brain regions containing crossing or fanning axons [75], [96], and (2) the presence of cerebrospinal fluid and other free water pools (e.g., cysts) biases diffusion measurements in both the tensor and powder representations, potentially confounding or masking true microstructural changes within the tissue [135]–[138]. Typically, a voxel with these free water partial volume effects will have elevated MD and reduced FA due to the high diffusivity and negligible anisotropy of free water.

To overcome the first limitation, techniques such as microscopic fractional anisotropy (μ FA) imaging, which reports water diffusion anisotropy independent of the neuron fiber orientation dispersion, were developed [71], [72], [98]. μ FA can be estimated by fitting traditional LTE dMRI data to various signal representations using a priori knowledge of the underlying tissue [99]–[101] or by using advanced dMRI pulse sequences like double diffusion encoding [94], [102] or spherical tensor encoding (STE) [72], [75], [104]. Previous studies have demonstrated that μ FA may be more suitable than FA for a number of applications such as in evaluating white matter degeneration in Parkinson's disease [73], delineating lesions and detecting abnormalities in multiple sclerosis [74], [139], and differentiating between different types of brain tumors [75].

The bias caused by free water partial volume effects on DTI and DKI measurements results from the fact that indices quantified using both representations represent the

weighted average of all water diffusion within a voxel rather than markers of a specific tissue. The diffusivity of free or unhindered water at 37°C is isotropic and approximately 3-4 times higher than that of brain tissue, so it has a significant effect on the voxel-level dMRI parameters, even at low volume fractions [65]. Moreover, the free water signal is typically a factor of 2-3 times higher than brain-tissue for the T_2 -weighted scans used for dMRI, which further exacerbates these partial volume effects. Accordingly, dMRI measurements made in brain regions with significant free water partial volumes (Figure 3-1), such as the fornix and other ventricle-adjacent regions, are greatly affected [140], [141].

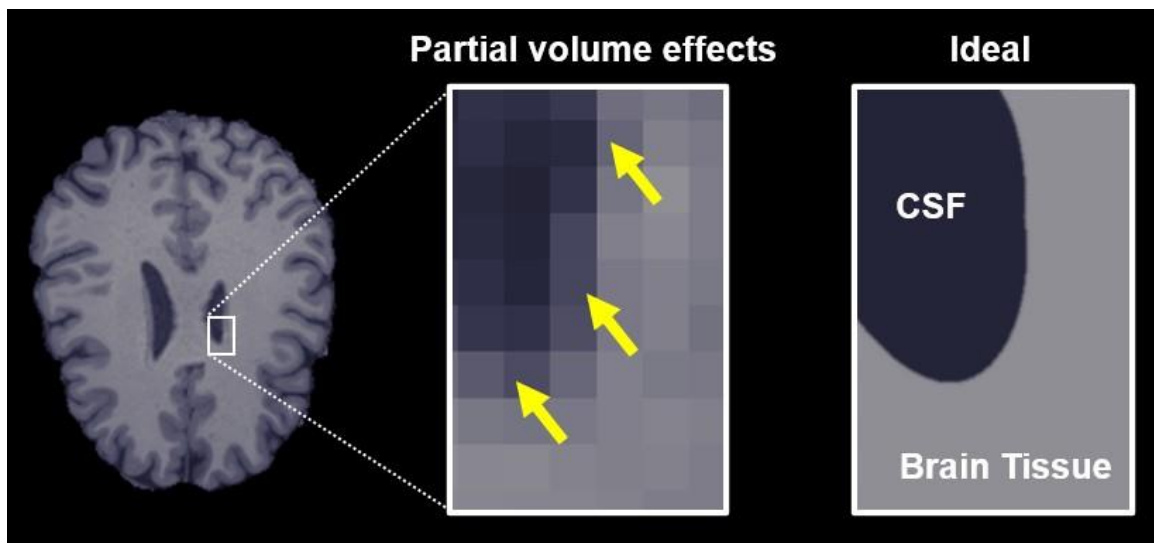


Figure 3-1. Free water partial volume effects at the interface between brain tissue and a ventricle containing cerebrospinal fluid (CSF). The image on the right depicts an ideal slice in which the brain tissue and CSF are clearly delineated, while the center image depicts partial volume effects in voxels that contain both CSF and tissue, highlighted by yellow arrows. The goal of the proposed algorithm is to obtain parameter estimates specific to the tissue in these voxels.

The effects of free water partial volumes can be attenuated by using non-zero minimum diffusion weighting [138] and by implementing fluid-attenuated inversion recovery dMRI sequences [142], [143], but both techniques decrease signal-to-noise ratio (SNR), the former affects DTI metrics in tissue with minimal free water, and the latter increases specific absorption rate and scan time [77]. Alternatively, modifications to the DTI and DKI representations can be used to distinguish between dMRI signal from free water and dMRI signal from functional brain tissue. The free water elimination DTI (FWE-DTI) representation separates the dMRI signal into two macroscopic components: one representing free water and one representing brain tissue [77], and can be expressed as:

$$S_i = S_0 \left(f e^{-b \sum_{i,j=1}^3 g_i g_j D_{T,ij}} + (1-f) e^{-b(3e-3)} \right) \quad (3.4)$$

where f is the apparent volume fraction of tissue (weighted by differences in S_0 between free water and tissue) within the voxel of interest and $D_{T,ij}$ is the ij^{th} element of the diffusion tensor corresponding to the tissue component (\mathbf{D}_T). The $(3e-3)$ term represents the diffusivity of free water at 37°C in mm²/s. Note that signal arising from extracellular water that is hindered, such as the water between neuronal axons, will primarily contribute to the tissue component and not the free water component. This representation enables more accurate estimation of tissue-specific indices than traditional DTI and has attracted interest for use in studying neurodegeneration in Alzheimer's disease [79], Parkinson's disease [78], and traumatic brain injury [80], among others. Additionally, the volume fraction metric is a potential surrogate marker for edema [77], [144]. While traditional DTI can be performed using single b-shell data, FWE-DTI should be performed with data collected at multiple b-values to reduce fitting degeneracies at the expense of increased scan time [145].

Recently, the FWE-DTI representation was expanded to account for non-Gaussian diffusion in the tissue compartment by expanding the cumulant expansion to the second order; this modification to FWE-DTI is referred to as the free water elimination DKI representation [146].

In this article, we propose a technique to measure water diffusion anisotropy that combines the STE-based μ FA acquisition protocol to achieve insensitivity to neurite orientation [72], [75] with the free water elimination representations' ability to distinguish between free water partial volume effects and true tissue properties.

3.3. Materials and Methods

Previously, we demonstrated that μ FA can be estimated by jointly fitting multi-shell LTE and STE dMRI data to the powder average diffusion kurtosis representation, as per the following equations (Arezza, Tse, and Baron 2021):

$$S_{b,LTE} = S_0 e^{-bD_{eff} + \frac{b^2 D_{eff}^2 K_{LTE}}{6}} \quad (3.5)$$

$$S_{b,STE} = S_0 e^{-bD_{eff} + \frac{b^2 D_{eff}^2 K_{STE}}{6}} \quad (3.6)$$

$$\mu FA = \sqrt{\frac{3}{2}} \left(1 + \frac{6}{5(K_{LTE} - K_{STE})} \right)^{-\frac{1}{2}} \quad (3.7)$$

where the subscripts *LTE* and *STE* denote the encoding scheme. By combining equations (3.5) and (3.6) with a FWE representation, the powder average free water elimination kurtosis representation (FWE-paK) can be defined in the LTE and STE encoding schemes via the following equations:

$$S_{b,LTE} = S_0 \left(f e^{-bD_T + \frac{b^2 D_T^2 K_{LTE}}{6}} + (1 - f) e^{-b(3e-3)} \right) \quad (3.8)$$

$$S_{b,STE} = S_0 \left(f e^{-bD_T + \frac{b^2 D_T^2 K_{STE}}{6}} + (1 - f) e^{-b(3e-3)} \right) \quad (3.9)$$

where D_T is the effective diffusivity in the tissue compartment, K_{LTE} is the effective diffusion kurtosis in the tissue compartment in the LTE scheme, and K_{STE} is the effective diffusion kurtosis in the tissue compartment in the STE scheme. The D_T , K_{LTE} , and K_{STE} terms obtained using equations (3.8) and (3.9) characterize water diffusion in brain tissue independent of free water. Accordingly, μ FA estimated from equation (3.7) using these corrected indices should characterize water diffusion anisotropy in tissue free of the bias caused by free water partial volumes. This imaging strategy which combines the FWE-paK signal representation with μ FA imaging acquisition will be referred to herein as the FWE imaging method, whereas the technique that involves fitting the data to the powder kurtosis representation will be referred to as the conventional method.

3.3.1. Fitting Algorithm

In this work, a two-part algorithm (denoted Part I and Part II) was used to obtain a solution to the joint fitting of STE and LTE data. In the first part of the algorithm, low b-value ($b \leq 1000 \text{ s/mm}^2$) powder average STE data were fitted to a FWE representation for effective powder average diffusivity (FWE-paD) to obtain estimates of f and D_T . The equation was derived from equation (3.9) by setting $K_{STE} = 0$:

$$S_{b,STE} = S_0 (f e^{-bD_T} + (1 - f) e^{-b(3e-3)}) \quad (3.10)$$

The indices computed with equation (3.10) were used as initial guesses in the second part of the algorithm, in which powder average STE and powder average LTE data across all b-values were jointly fitted to equations (3.8) and (3.9).

Part I of the algorithm exploits the FWE-paD representation's lower complexity relative to the FWE-paK representation, reducing the number of unknown variables to be

solved for by omitting the effective kurtosis term. The effects of non-Gaussian diffusion on dMRI, while deleterious to signal representations based on the first order cumulant expansion of the dMRI signal, are minimal at low b-values; thus, f and D_T can be initially estimated despite omitting the second order term in the cumulant expansion. Using only the STE data as input further reduces the effects of non-Gaussian diffusion on the fit because it typically has minimal kurtosis. More specifically, LTE introduces a variance to the powder average signal due to the different diffusion encoding directions used for each acquisition; STE signals are free of this variance and deviate less from the mono-Gaussian diffusion assumption inherent to the FWE-paD signal representation in tissue-containing voxels [72], [94]. In this work, an iterative method was used to solve the FWE-paD equation. In each iteration, the low b-value STE data were first fitted to the FWE-paD representation (equation (3.10)) using the least squares method with a fixed estimate of $D_T = 7e - 4 \text{ mm}^2/\text{s}$ used as an initial guess in the first iteration. Then, a correction was implemented to constrain f and $(1 - f)$ to be positive. The D_T estimate was then updated by again fitting the data to equation (3.10) using the least squares method, this time with f and $(1 - f)$ as fixed inputs. A correction was implemented at the end of each iteration to set D_T to 0 in voxels with very small tissue compartments ($f < 0.1$). The FWE-paD fit performed in Part I could be replaced by other techniques to obtain initial estimates of f and D_T depending on data availability; for example, if low b-value STE data is not available, LTE data can be fitted to the FWE-DTI signal representation depicted in equation (3.4).

In Part II of the algorithm, the LTE and STE data across all b-values were jointly fitted to the FWE-paK representation using the f and D_T indices from Part I as initial

estimates. Again, an iterative method was employed that was similar to that of Part I. In each iteration, the data were first fitted to the equations (3.8) and (3.9) to solve for D_T , K_{LTE} and K_{STE} using a fixed f value (the first iteration used the value of f that was obtained from Part 1). Corrections were performed to constrain K_{LTE} to be positive and K_{STE} to be greater than or equal to -0.1. Then, the data were jointly fitted to equations (3.8) and (3.9), this time using fixed estimates of D_T , K_{LTE} and K_{STE} to obtain an updated estimate of f . A final correction was performed at the end of each iteration to constrain f and $(1 - f)$ to be positive.

Part I and Part II were each performed for 100 iterations for all simulated and *in vivo* implementations of FWE- μ FA investigated in this article. For all cases, adding more iterations caused negligible changes in the output parameters. The fitting code is openly available at gitlab.com/coreybaron/fwe_ufa.

3.3.2. Synthetic dMRI Simulations

To investigate the differences between the FWE- μ FA method proposed herein and standard fitting, equations (3.8) and (3.9) were used to generate synthetic LTE and STE powder average signals to simulate white matter (WM) and gray matter (GM) voxels. These simulations were designed to also probe the performance of the non-convex fitting algorithm under the influence of noise and incorrect estimates for the free water diffusivity. For each voxel, signals were generated for b-values of 0, 700, 1000, 1400, and 2000 s/mm². To simulate a typical WM configuration, μ FA was measured from publicly available dMRI data [123] using the conventional μ FA method [81], and typical parameter values were extracted from frontal WM voxels in which free water contamination is expected to be minimal relative to tissue in other brain regions. The corresponding parameters are $D_T = 8e - 4mm^2/s$, $K_{LTE} = 1.2$, and $K_{STE} = 0.1$, which corresponds to a μ FA of 0.85 as per

equation (3.7). These parameters were used to simulate the signal acquired in voxels with simulated tissue volume fractions (f_{sim}) of 0.2, 0.4, 0.6, 0.8, and 1 via equations (3.8) and (3.9). Rician noise was simulated by adding random Gaussian noise to the real and imaginary components of the signal and then computing the magnitude of the noisy signal. The standard deviation of the noise added to the signals was scaled by $1/\sqrt{N_{acq}(b)}$, where $N_{acq}(b)$ is the number of acquisitions used experimentally for each b-value, to account for averaging from multiple acquisitions when the powder average is computed. Note that the noise standard deviation was chosen to achieve a specific SNR for the case in which $f_{sim} = 1$ and the b-value is 0. WM voxels were simulated at SNR values of 10, 20, and 40 (before scaling noise based on the number of acquisitions) with a fixed free water diffusivity of $3e^{-3} \text{ mm}^2/s$ to assess the effects of noise on the measurements. Also, WM voxels were simulated with free water diffusivities of $2.85e^{-3}$ and $3.15e^{-3} \text{ mm}^2/s$ at the SNR of 20 to assess how deviations in free water diffusivity affect the measurements. Notably, PCA denoising [124] is typically used for *in vivo* data prior to parameter fitting and, accordingly, the simulations likely explore a more challenging fitting scenario than *in vivo*.

Due to the presence of free water in cortical GM voxels, as well as the heterogeneity between different deep GM regions of the brain, a typical GM configuration is difficult to assess. For this work, GM μFA was set to 0.55 as this is within the range of values found in the hippocampus [147] and other deep GM regions [148]; using the same D_T as the WM simulations, the K_{LTE} and K_{STE} values were set to 0.9 and 0.6, which yields the desired $\mu\text{FA} = 0.55$ via equation (3.7). GM simulations were performed over the same tissue volume fractions, SNRs, and free water diffusivities as the WM simulations.

1000 realizations of random noise were generated for each simulation configuration. The FWE and conventional methods of estimating μFA were performed on the simulated voxels, and the mean and standard deviation of the following indices were computed across all setups for both methods: D_T , effective anisotropic kurtosis (K_{aniso}), effective isotropic kurtosis (K_{iso}), and μFA . The effective kurtosis terms were computed as follows:

$$K_{aniso} = K_{LTE} - K_{STE} \quad (3.11)$$

$$K_{iso} = K_{STE} \quad (3.12)$$

The relative error against the known ground truth was computed for each measurement using the following equation:

$$Rel. Error = \frac{X_{meas} - X_{GT}}{X_{GT}} \quad (3.13)$$

where X is the metric of interest and the subscripts *meas* and *GT* denote the measured value and known ground truth, respectively.

3.3.3. Monte Carlo Simulations

The synthetic powder average signals simulated in the previous section were derived using the same equation as is used in Part II of the fitting algorithm, which may glamorize the FWE technique. To validate those results, Monte Carlo random walk simulations were performed using Camino [149] to compare FWE with the conventional signal representation in a scenario in which the ground truth was known. The simulation geometry was set to be infinitely long cylinders to represent neuronal axons with a 1 μm radius, 0.7 intra-tube volume fraction, and water diffusivity of $2e - 3 \text{ mm}^2/\text{s}$ [150]; note that this case is assumed to represent a tissue volume fraction of $f_{sim} = 1$ as the extra-tube water is restricted and thought to contribute to D_T . A free water compartment was simulated

using a diffusivity of $3e - 3 \text{ mm}^2/\text{s}$ and was added to the tissue to achieve f_{sim} values of 0.2, 0.4, 0.6, 0.8, and 1. LTE and STE signals were simulated at b-values of 0, 700, 1000, 1400, and 2000 s/mm^2 , with 15 diffusion directions acquired at each b-value in the LTE scheme.

LTE and STE data were powder averaged and the following metrics were estimated using the conventional and FWE methods: D_T , K_{aniso} , K_{iso} , and μFA . The metrics computed using the conventional paK method at $f_{sim} = 1$ were assumed to be the ground truth and were used to compute the relative error for all other measurements.

3.3.4. In Vivo

To assess the FWE μFA algorithm in real dMRI data, 4 healthy volunteers (2 female and 2 male, mean age 28.0 ± 6.6 years) were scanned on a 3T Prisma whole body MRI system (Siemens Healthineers) located in the Centre for Functional and Metabolic Mapping at Western University with 80 mT/m strength and 200 T/m/s slew rate. Volunteers first underwent T_1 -weighted MPRAGE acquisitions with 1 mm isotropic resolution to provide structural image volumes for segmenting regions-of-interest (ROIs). Then each subject underwent dMRI scans consisting of 5 acquisitions with no diffusion-weighting ($b = 0 \text{ s}/\text{mm}^2$), and 3, 15, 6, and 22 LTE acquisitions plus 6, 10, 10, and 27 STE acquisitions at b-values of 700, 1000, 1400, and 2000 s/mm^2 , respectively. The STE pulse sequence used is described in Arezza *et al* [81]. The other parameters for the dMRI acquisitions were: TE/TR = 94/4500 ms, field-of-view = 220 x 200 mm^2 , resolution = 2 mm (isotropic), 48 slices, and rate 2 in-plane parallel imaging combined with rate 2 simultaneous multislice. Note that the b-values acquired in the dMRI acquisitions match those of the synthetic dMRI and Monte Carlo simulations.

Post-processing for the dMRI data included PCA denoising [124] and Gibbs ringing correction using MRtrix3 [151], [152], and eddy current artifact correction using FSL *eddy* [121]. Powder average signals were then computed from the LTE and STE data at each b-value and were then fitted to equations (3.8) and (3.9) to obtain μFA via the FWE method and fitted to equations (3.5) and (3.6) using ordinary least squares to obtain μFA via the conventional method.

The T_1 -weighted image volumes were used to obtain masks for ROIs because of their superior resolution and soft-tissue contrast compared to the dMRI image volumes. WM ROI masks were generated using the *fast* tool from FSL [125] using a probability threshold of 99% and limiting the masks to the region of the brain superior to the thalamus. Masks for the hippocampus, putamen, and thalamus were generated using the *first* tool from FSL [153]. ROI masks for the fornix were manually drawn. The T_1 volumes were then registered to the powder averaged $b=0$ s/mm² volumes using symmetric diffeomorphic and affine transformations with ANTS software (<https://github.com/ANTsX/ANTs>); these transformations were then applied to each of the ROI masks to register them to dMRI space.

The ROIs were selected to test several specific hypotheses. The WM and putamen are generally less contaminated by free cerebrospinal fluid than other regions, so it was expected that measurements made with the FWE and kurtosis μFA methods would be similar. The thalamus and hippocampus ROIs represent deep GM structures adjacent to free water, in which it was expected that the D_T would be reduced and μFA would be elevated when using the FWE technique due to mitigation of free water signal. The fornix, which is both adjacent to the lateral ventricles and small relative to the image resolution, represents an ROI that is likely to have significant free water contamination; thus, much

lower D_T and much higher μFA were expected in this region when the FWE technique was used.

Mean and standard deviation of the following indices were computed in each of the ROIs to compare the FWE and conventional μFA techniques: D_T , K_{aniso} , K_{iso} , and μFA . Voxels with $f < 0.25$ after fitting were excluded from this analysis because there is very little tissue signal for which the diffusion parameters correspond to, which leads to unstable estimations of the parameters.

3.4. Results

3.4.1. Synthetic dMRI Simulations

The relative errors of measurements made with the FWE and conventional techniques at different SNR levels are depicted in Figure 3-2. Note that for the conventional method, only the 20 SNR case is displayed because relative errors did not differ by more than the plot line thickness at the various SNR levels. For all volume fractions except $f_{sim}=1$, and at all three SNR levels, the FWE μFA method yielded more accurate mean measurements of D_T and μFA than the conventional method in both the WM and GM configurations. At $f_{sim} = 0.2$, the FWE method substantially overestimated f in both the WM and GM simulations; however, resulting D_T and μFA estimates were closer to the ground truth than measurements produced by the conventional method. FWE estimates of K_{aniso} were higher than estimates produced by the conventional method across all f_{sim} , while estimates of K_{iso} were lower. The variance of parameter estimations over the 1000 repetitions increased for decreasing f_{sim} .

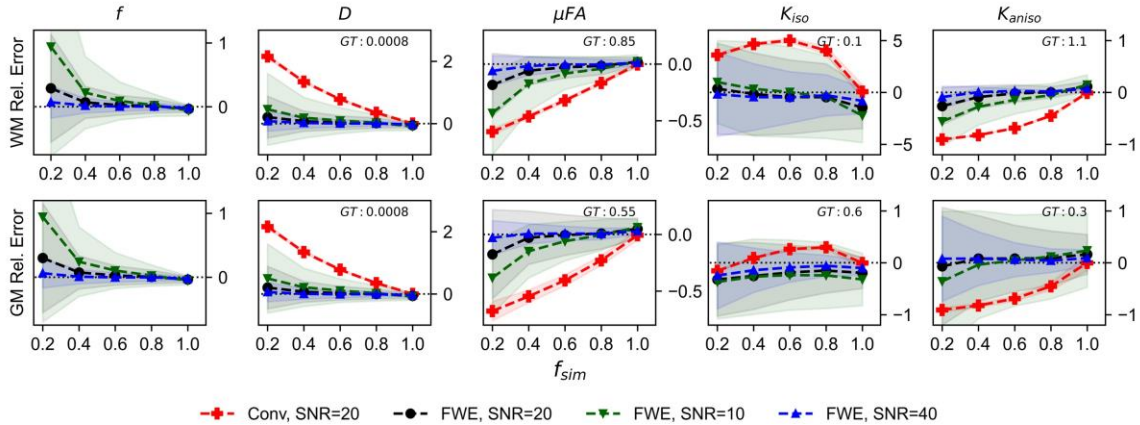


Figure 3-2. Relative error in diffusion MRI indices measured in synthetic white matter (WM) and gray matter (GM) voxels at various SNR levels and a free water diffusivity of $3e - 3mm^2/s$. The x-axis depicts the simulated volume fraction (f_{sim}), while the ground truth value for each metric is denoted as GT. The red line with crosses indicates the mean measurements made using the conventional (Conv) method at SNR=20, the black line with circles depicts the FWE method at SNR=20, the green line with inverted triangles depicts the FWE method at SNR=10, and the blue line with triangles depicts the FWE method at SNR=40.

The relative errors of measurements made with the FWE and conventional techniques using different free water diffusivities are depicted in Figure 3-3. Note that for the conventional method, only the $3e - 3mm^2/s$ case is displayed because relative errors did not differ considerably regardless of free water diffusivity. The FWE μFA method again yielded more accurate mean measurements of D_T and μFA than the conventional method in both WM and GM configurations for all free water diffusivity values and across all volume fractions except $f_{sim} = 1$. f was again overestimated at $f_{sim} = 0.2$, with the greatest relative error being observed in the signal with a simulated free water diffusivity of $2.85e - 3mm^2/s$. FWE estimates of K_{aniso} were again higher than estimates produced by the conventional method across all f_{sim} , while estimates of K_{iso} were lower.

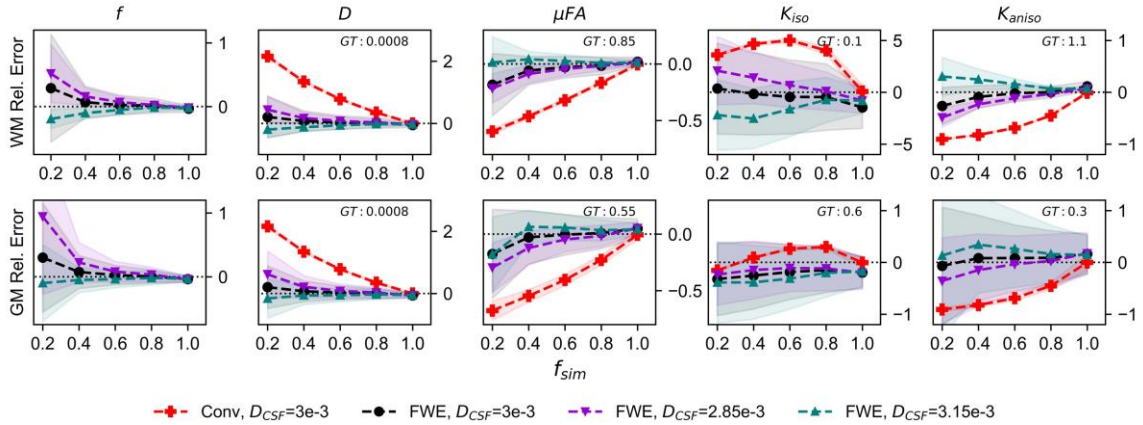


Figure 3-3. Relative error in diffusion MRI indices measured in synthetic white matter (WM) and gray matter (GM) voxels with various free water diffusivities (D_{CSF}) and an SNR of 20. The x-axis depicts the simulated volume fraction (f_{sim}), while the ground truth value for each metric is denoted as GT. The red line with crosses indicates the mean measurements made using the conventional (Conv) method with $D_{CSF} = 3e - 3mm^2/s$, the black line with circles depicts the FWE method with $D_{CSF} = 3e - 3mm^2/s$, the purple line with inverted triangles depicts the FWE method with $D_{CSF} = 2.85e - 3mm^2/s$, and the teal line with triangles depicts the FWE method with $D_{CSF} = 3.15e - 3mm^2/s$.

3.4.2. Monte Carlo Simulations

The relative errors of measurements made with the FWE and conventional techniques in the Monte Carlo simulations are depicted in Figure 3-4. Across all f_{sim} , the FWE method underestimated f by approximately 3%. At $f_{sim} = 1$, measurements of D_T and K_{iso} made using the FWE method were underestimated by approximately 4.8% and 35%, respectively, relative to measurements made using the conventional method, while measurements of μFA and K_{aniso} were overestimated by 2.8% and 10.5%, respectively. Measurements made with the FWE technique were consistent across all f_{sim} , while the relative error in all measurements made with the conventional technique increased with decreasing f_{sim} (except K_{iso} error, which appeared to peak at a volume fraction in the range

of $0.4 < f_{sim} < 0.6$). All metrics measured with the FWE method were much closer to the ground truth than those measured with the conventional method at $f_{sim} < 1$.

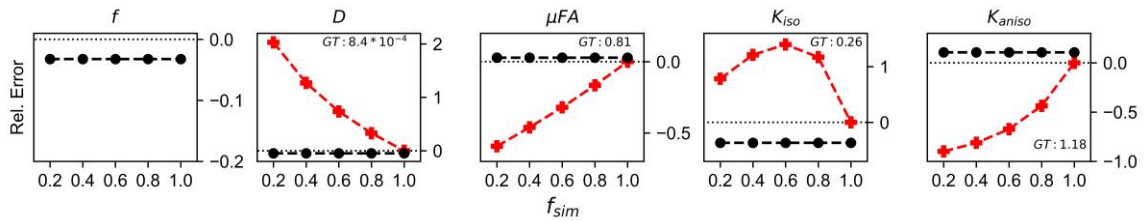


Figure 3-4. Relative error in diffusion MRI indices measured using the conventional (Conv) and FWE methods on signals simulated using a Monte Carlo technique. The geometry consisted of infinitely long cylinders with a $1 \mu\text{m}$ radius and 0.7 intra-tube fraction. The x-axis depicts the simulated volume fraction (f_{sim}), while the ground truth value for each metric is denoted as GT. The red line with crosses indicates the measurements made using the conventional (Conv) method while the black line with circles indicates measurements made using the FWE method.

3.4.3. In Vivo

Example slices of D_T , K_{aniso} , K_{iso} , and μFA generated with the FWE and conventional methods are depicted in Figure 3-5, as well as a sample slice depicting voxels with $f < 0.25$. Zoom-ins of a cortical region are depicted in Figure 3-6, where decreases in K_{iso} and D_T , and increases in μFA and K_{aniso} , are observed for FWE relative to the conventional method throughout the cortex, which agrees with expectations from the simulations. The ROIs are depicted in T_1 -weighted images in Figure 3-7, as well as the mean and standard deviations of relevant diffusion indices generated using the two methods. Mean volume fractions in the WM, putamen, hippocampus, thalamus, and fornix regions were 0.96, 0.96, 0.82, 0.82, and 0.64, respectively. Differences in D_T and μFA between the two methods were smallest in the WM and putamen ROIs. When the FWE method was employed, D_T was reduced by 6.4% and 7.5% in the WM and putamen,

respectively, compared to measures made using the conventional method, while μFA was increased by 3.5% and 5.3%. Greater differences between methods were observed in the deep GM regions: D_T was reduced by 37.1% in the hippocampus and 42.8% in the thalamus when FWE was used, while μFA was increased by 22.0% and 16.8% in those regions. The most significant differences between methods were observed in the fornix, in which D_T was reduced by 59.2% and μFA was increased by 30.5% when FWE was applied. In all ROIs, mean K_{aniso} was reduced while mean K_{iso} was increased when FWE was used.

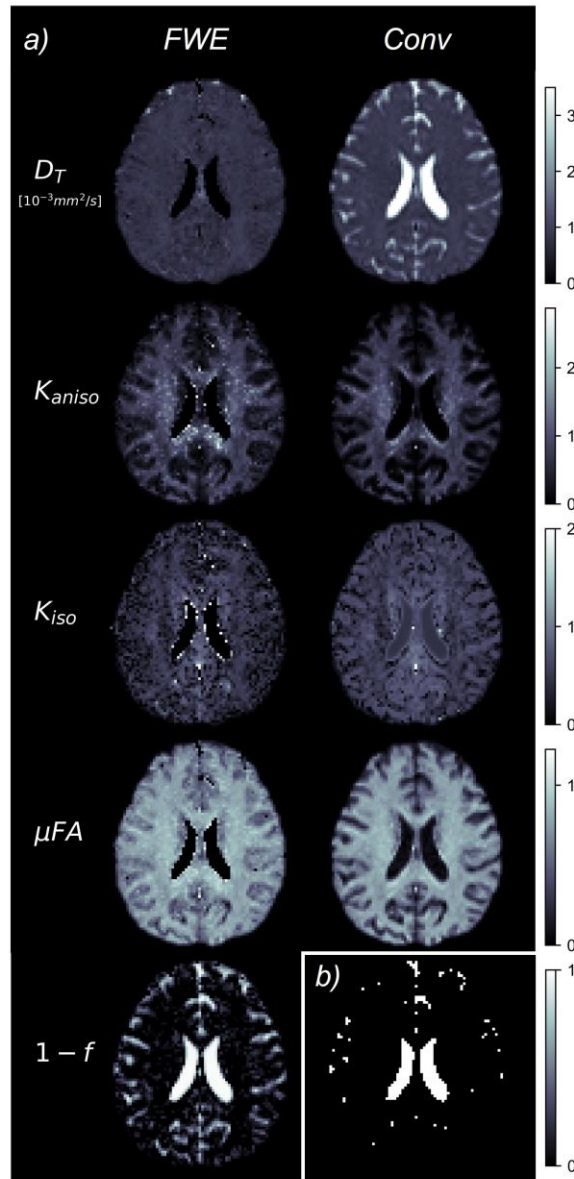


Figure 3-5. (a) Example slices of tissue diffusivity (D_T), anisotropic kurtosis (K_{aniso}), isotropic kurtosis (K_{iso}), microscopic fractional anisotropy (μFA), and fluid volume fraction ($1-f$) measured in one of the healthy volunteers. The images on the left were computed using the free water elimination (FWE) method while those on the right were computed using the conventional (Conv) method. Note that D_T is used interchangeably with D for the conventional method. (b) Sample slice depicting a binary map showing voxels with tissue volume fractions less than 0.25, which were omitted in region-of-interest analyses.

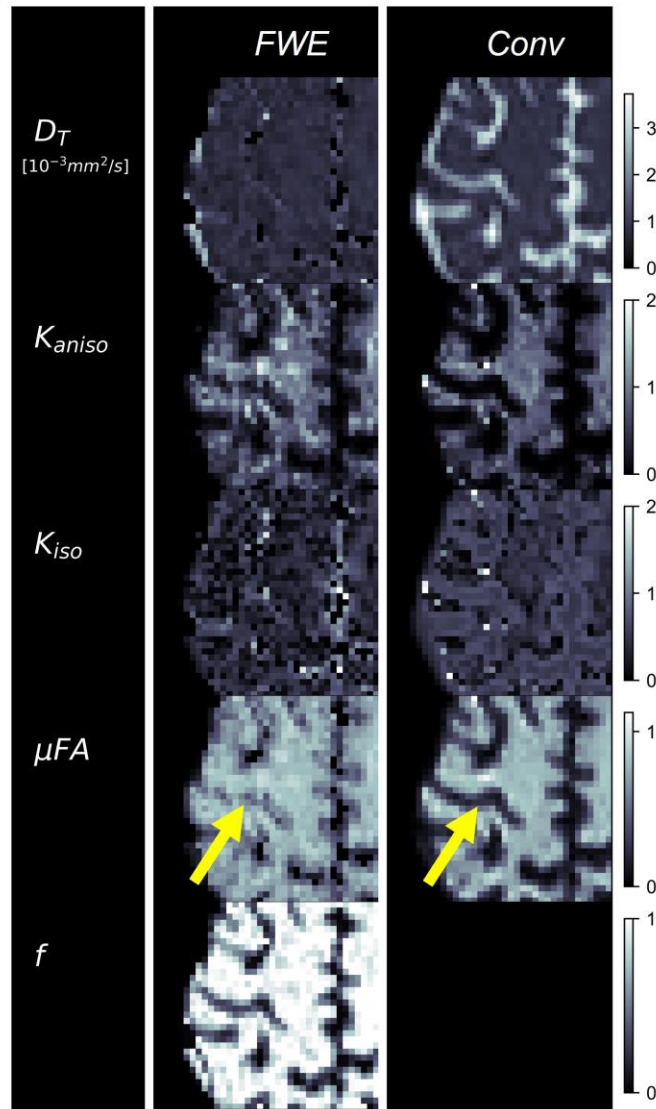


Figure 3-6. Example cerebral cortex images of tissue diffusivity (D_T), anisotropic kurtosis (K_{aniso}), isotropic kurtosis (K_{iso}), microscopic fractional anisotropy (μFA), and tissue volume fraction (f) measured in one of the healthy volunteers. The images on the left were computed using the free water elimination (FWE) method while those on the right were computed using the conventional (Conv) method. Note that D_T is used interchangeably with D for the conventional method. The yellow arrow highlights a region in which a significant difference is observed between the FWE and conventional μFA measurements due to high free water contamination.

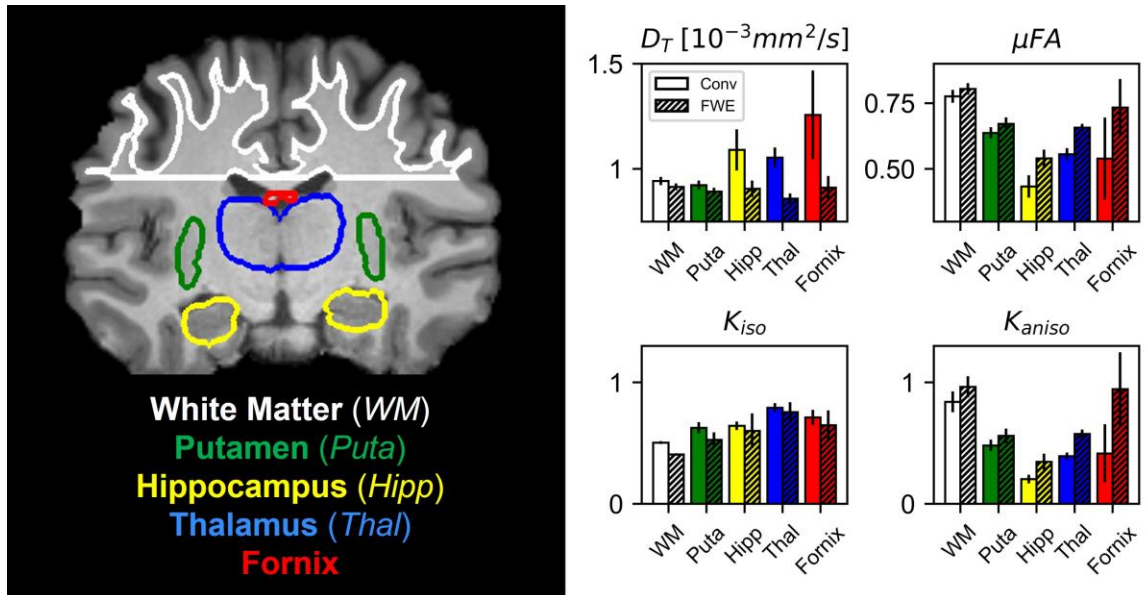


Figure 3-7. Comparison between the conventional (Conv) and free water elimination (FWE) methods in four healthy volunteers. Depicted on the left is a coronal T₁-weighted MPRAGE slice from one of the volunteers highlighting the five regions-of-interest (ROIs). Note that volumetric ROIs were used, despite the single slice depiction. On the right are plots comparing the mean diffusivity (D_T), microscopic fractional anisotropy (μFA), isotropic kurtosis (K_{iso}), and anisotropic kurtosis (K_{aniso}) produced by the Conv and FWE methods. In all ROIs, D_T and K_{iso} were reduced when FWE was applied, while μFA and K_{aniso} were elevated, though the magnitude of this difference varied by region. Note that D_T is used interchangeably with D for the conventional method.

3.5. Discussion

The FWE method presented herein allows for rapid computation of free water-corrected μFA because it uses alternating least squares estimations for f and the various diffusion parameters, which are individually rapid. The total processing time was <1 min for each subject on a common personal desktop computer. In this work, 100 iterations were performed for each step, but computation time could be further reduced by setting termination criteria for instances in which 100 iterations would be excessive. One such

example would be to use the estimate of f from Part 1 to omit voxels with very high CSF contamination (e.g. $f < 0.25$) from Part 2.

In synthetic dMRI simulations, the FWE method produced more accurate measurements of D_T and μFA than the conventional method across all volume fractions except $f_{sim}=1$. At $f_{sim}=1$, the simulated signal vs. b-value curve has no free water component and resembles the paK signal representation (equations (3.5) and (3.6)), so the two-compartment representation is redundant and falsely detects a small free water compartment due to the added noise. In simulations with no added noise (data not shown), the FWE and conventional methods both correctly measure D_T and μFA at $f_{sim}=1$, though only the FWE method yields correct indices at lower f_{sim} .

The increase in K_{aniso} when the FWE method was employed can be explained by the fact that K_{aniso} arises solely from the tissue compartment. K_{aniso} describes the variance in the dMRI powder average signal due to the eccentric shape of neuron fibers and other compartments [96]; for example, a dMRI acquisition in the direction parallel to neuronal axons will yield a lower signal than one perpendicular to the axons. By removing the isotropic free water compartment, the effect of K_{aniso} on the remaining signal component is amplified. The reduction in K_{iso} when the FWE method was used can be attributed to the fact that K_{iso} describes the variance in diffusivity across compartments; thus, removing the free water compartment, which contains a significantly higher mean diffusivity than neural tissue, attenuates this metric.

Comparisons between measurements made at different SNR values revealed that the FWE technique is susceptible to noise, as mean measurements accuracy decreased and standard deviation across 1000 voxels increased with decreasing SNR. Despite its

sensitivity to noise, the FWE technique still produced more accurate mean measurements at the low SNR of 10 than the conventional method did at any SNR level in regions with reduced f_{sim} . These results suggest that the effects of free water partial volume contamination can be more deleterious to dMRI measurements than noise at the SNR levels typically achieved *in vivo*.

Synthetic dMRI simulations assessing the effects of deviations in the assumed free water diffusivity revealed that measurements made with the FWE technique are generally less accurate when the diffusivity of free water is not exactly $3e - 3mm^2/s$. In real tissue, deviations from the assumed temperature of 37°C and biases due to differences in T_1 and T_2 can alter the free water diffusivity and affect the accuracy of the signal fitting algorithm [77], [144]. However, this limitation is shared by all multi-compartment signal representations that use fixed estimates of free water diffusivity and can only be overcome by determining the value prior to the fitting or by attempting to solve for the free water diffusivity in each voxel as an additional variable at the expense of computation time and potential misestimation. Note that despite this limitation, the FWE method still yielded more accurate mean measurements than the conventional method at lower f_{sim} .

In the Monte Carlo simulations, the FWE method underestimated f by a relatively constant 3% for all simulated tissue volume fractions. At $f_{sim} = 1$, the water-containing cylinders comprise of 70% of the simulated volume, but the extra-tube water is restricted by their presence and likely contributes to D_T . This bias likely resulted from kurtosis arising from the simulation geometry being partially misattributed to a free water compartment. Nevertheless, the bias is small and consistent for different volume fractions, which mitigates deleterious effects when comparing different regions or subjects. Note that

repeating the Monte Carlo simulation with 60 directions at each b-value instead of 15 did not reduce the bias in f , which suggests that an inadequate number of directions in the powder average was not the cause.

The FWE method also showed promising results when used to measure D_T and μFA in healthy volunteers as differences between the two methods in the various ROIs agreed with expectations. In all ROIs, D_T was reduced and μFA was elevated when the FWE method was used (Figure 3-7); these changes are intuitive as removing an isotropic signal compartment with high diffusivity from the overall signal, which also contains anisotropic signal components from neurites and other eccentric compartments, will raise the measured diffusion anisotropy and lower the mean diffusivity. The results of the *in vivo* imaging analysis agreed with the hypotheses that the effects would be smallest in the WM and putamen regions and greatest in the free water-adjacent fornix ROI (Figure 3-7). Furthermore, the f parameter allowed for the removal of voxels with high CSF contamination from the ROI analysis, improving mean measurements. However, one drawback of the technique is that there are no ground truth measurements to validate the measured indices against. Comparing measured tissue volume fractions against known values from the literature can act as a pseudo-validation of the FWE method, though it should be noted that the measured f index represents the T_2 -weighted signal fraction of the tissue compartment rather than the true volume fraction. To convert f to the true volume fraction of tissue, f_T , a correction can be made as per the following equation [154]:

$$f = \frac{f_T e^{-TE/T^2_{Tissue}}}{f_T e^{-TE/T^2_{Tissue}} + (1 - f_T) e^{-TE/T^2_{CSF}}} \quad (3.14)$$

Literature reports free water volume fractions of <2% for WM and 7-9% for GM with high standard deviations [155], [156], which correspond to f_T values of >0.98 for WM and 0.91-

0.93 for GM. Assuming $T2_{CSF} = 1250$ ms [157], $T2_{WM} = 70$ ms [158], and $T2_{Putamen} = T2_{Hippocampus} = T2_{Thalamus} = 95$ ms [158], [159] at 3T, the approximate mean f_T values for the WM, putamen, hippocampus, and thalamus regions were 0.99, 0.98, 0.92, and 0.92 in the healthy volunteers imaged in this work. As expected, the volume fraction in the fornix was measured to be much lower than the other ROIs ($f = 0.64$); no correction was performed for this region because many voxels contained large volumes of pure CSF, which violates the assumptions of equation (3.14). While previous studies have found evidence that brain tissue volume fraction decreases with age due to increased interstitial space [160], such effects are not expected to have impacted the results of this work due to the young age of the participant cohort.

There are several limitations potentially affecting this study. Diffusion time discrepancies between the LTE and STE sequences, and between the three gradient channels in the STE sequence, were not taken into consideration in this work. Different diffusion times in the LTE and STE acquisitions could lead to slight differences between the respective powder average signals that are misattributed to be differences between K_{LTE} and K_{STE} , while different diffusion times in the different gradient channels for the STE acquisitions could give rise to orientational biases [93]. These potential biases are not expected to have had a significant effect on the results of this work since both the FWE method and conventional method were applied to the same data, and any biases caused by time-dependent diffusion would affect both approaches. However, future studies should consider using optimized STE sequences to ensure that the diffusion time of the STE and LTE sequences match and that there are no orientational biases in the STE sequence.

Another limitation is that the time required for an acquisition protocol to acquire powder average signals at 4 b-values in both LTE and STE schema could be prohibitively long for some applications (our *in vivo* scan required 9 min).

Both the conventional and FWE approaches used herein assume that any deviation from mono-Gaussian diffusion in the tissue arises exclusively from two distinct sources: K_{aniso} and K_{iso} . However, restricted diffusion inside compartments, exchange between compartments, and microstructural disorder can also contribute to the overall kurtosis and are often categorized together in a term known as microscopic kurtosis (μK) [93], [94]. Though most μ FA imaging techniques do not consider μK , recent studies have found that it is non-negligible in the human brain and that ignoring it can lead to biases [161]. Despite this limitation, μ FA techniques that do not distinguish μK from other kurtosis sources have shown promising diagnostic and research capabilities and still represent a significant advance over the widely used DTI metrics.

The images produced by the FWE method (Figure 3-5 and Figure 3-6) appear grainier than those produced by the conventional method and higher standard deviations were measured in all metrics when the FWE method was used, both in simulations (Figure 3-2 and Figure 3-3) and *in vivo* (Figure 3-7). This increased variance is expected due to the increased complexity of the FWE-pAK representation relative to the paK representation. Studies that use the FWE technique should design MRI protocols that sample more b-shells to improve the data fit and acquire more LTE and STE scans at each b-value to raise the SNR of the powder average signals. A minimalistic protocol, such as those described in the literature [81], [117], may be insufficient for FWE imaging. Also, regularization

enforcing spatial smoothness, similar to that applied in other applications of FWE, could likely help mitigate this issue [77], [145].

The conventional and FWE methods used in this work both derive μ FA and other metrics using orientationally-averaged signals in the LTE scheme, which can introduce biases into measurements due to the positively-skewed distribution of Rician noise [162], [163] and due to non-uniform or insufficient sampling of the diffusion sphere in the LTE regime [164]. While measures were taken to denoise and preprocess the *in vivo* dMRI data used in this work, some of the LTE b-shells were minimalistic (e.g. only 6 directions were acquired at 1400 s/mm²). The simple arithmetic averaging method used in this work to compute powder average signals may be suboptimal given the minimalistic LTE acquisition protocol used, and more advanced algorithms to compute the powder average signal could potentially reduce biases [164].

In conclusion, the two-compartment μ FA imaging technique presented in this work represents an extension to a conventional μ FA imaging technique that integrates a free water compartment to extract tissue-specific indices of D , K_{aniso} , K_{iso} , and μ FA. This approach requires only modest assumptions about the content of the voxel and makes no assumptions about the tissue microstructure – it could be described as a “macrostructural model”. To solve the ill-conditioned fit of the data to equations (3.8) and (3.9), a two-part algorithm was employed to first determine initial guesses of key parameters and then to perform the joint fit. Any dMRI protocol designed to estimate μ FA via the FWE method proposed in this work will be versatile due to the need for multiple b-shells in both LTE and STE schema and can also be fitted to the conventional μ FA method and the DKI signal representation; furthermore, if a significant number of LTE directions are acquired at $b =$

1000 s/mm², the data can be fitted to the widely adopted DTI signal representation as well. Both simulation and real data experiments indicated that the FWE method may be a feasible technique for measuring μ FA and other dMRI indices with greater specificity to neural tissue characteristics by removing free water partial volume effects. It should also be noted that other μ FA approaches, such as the STE techniques that use the gamma signal representation, DDE techniques, and techniques that exclusively derive the metrics from LTE acquisitions, could likely also be modified to include a free water compartment.

While Chapters 2 and 3 focused on the development of μ FA imaging protocols, Chapter 4 introduces a potential clinical application for the technique: the detection of hippocampal abnormalities in patients with unilateral temporal lobe epilepsy.

Chapter 4

4 Microscopic Fractional Anisotropy Asymmetry in Unilateral Temporal Lobe Epilepsy

4.1. Overview

This chapter is adapted from a manuscript currently in preparation titled *Microscopic Fractional Anisotropy Asymmetry in Unilateral Temporal Lobe Epilepsy* [165], which is posted as a preprint on *medRxiv*.

4.2. Introduction

Temporal lobe epilepsy (TLE) is the most common form of focal epilepsy in adults, with as many as two-thirds of seizure foci being localized to the temporal lobe [34], [37], [166]. Though TLE can often be managed with anticonvulsant medications, approximately 30% of adults with epilepsy eventually develop medically intractable epilepsy despite appropriate drug therapy [36], [37]. Surgical resection of the seizure focus has been shown to be superior to medical treatment and is the method of choice for managing medically intractable TLE [167], [168]. In most of these patients, the epileptic focus lies within the mesial region of the temporal lobe and can be identified by the presence of mesial temporal sclerosis (MTS), which manifests as scarring and atrophy that can often be detected by MRI [169]. Seizure freedom following surgical resection is achieved in 75% of patients with clearly delineated MTS in MRI (i.e. MR-positive or MR+ patients), but in only 51% of MR-negative (MR-) patients [170], perhaps because the seizure focus has not been adequately localized and the resection is incomplete. This demonstrates the need for highly sensitive imaging techniques to complement the current gold standard MRI, EEG, and nuclear medicine techniques, and improve seizure focus localization.

Diffusion-weighted MRI (dMRI) is a promising technique for visualizing pathological abnormalities in TLE due to its sensitivity to neuron microstructure. The diffusion tensor imaging (DTI) parameters fractional anisotropy (FA) and mean diffusivity (MD) are of particular interest because demyelination, reduced axon density, and widened extracellular spaces due to gliosis reduce FA and increase MD [171]. Previous studies have shown that increased MD and reduced FA are present in various brain regions in TLE patients [170]–[172], and that increased MD is present in the ipsilateral side of the hippocampus in patients with unilateral TLE [173], [174]. Despite these promising results, the DTI signal representation is inadequate for quantifying regions with crossing or fanning neuron fibers because of its sensitivity to intra-voxel fiber orientation dispersion [96], [175]. FA, in particular, significantly underestimates water diffusion anisotropy in regions with complex fiber orientations [176]; this limits its specificity to abnormalities in TLE because the most common pathology in medically intractable TLE is hippocampal sclerosis (HS) [177], [178] but the hippocampus contains crossing fiber regions [179].

Microscopic fractional anisotropy (μ FA) is a recently developed dMRI metric that quantifies water diffusion anisotropy independent of both neuron fiber orientation dispersion and compartment size [72]. Generally, μ FA imaging techniques distinguish between anisotropy resulting from microstructure and anisotropy resulting from axon orientation by exploiting the contrast between two different dMRI acquisitions [72], [75], [98], [102]: (1) acquisitions that each probe diffusion in a single direction (i.e. encoding that is typically used in dMRI), and (2) acquisitions that probe diffusion in multiple orthogonal directions simultaneously. Previous studies have demonstrated that μ FA outperforms FA for delineating lesions in multiple sclerosis [74], for evaluating white

matter degeneration in Parkinson's disease [73], and for distinguishing between different types of brain tumors [75], among other potential applications. In the TLE clinical workflow, μ FA may provide a complementary metric to the current imaging and EEG techniques due to its sensitivity to microstructure and insensitivity to fiber orientation, particularly in brain regions containing crossing fibers, such as the hippocampus [147]. However, the benefits of μ FA imaging in TLE have not yet been assessed.

This preliminary work aims to evaluate the sensitivities of μ FA, FA, MD, and regional volume to detect abnormalities in four hippocampal subregions in patients with unilateral TLE. Asymmetries in measurements of anisotropy, diffusivity, and volume between the ipsilateral and contralateral hemispheres may indicate unilateral abnormalities that can lateralize the epileptic focus. We hypothesize that μ FA may be more sensitive to hippocampal abnormalities than FA due to its independence from neuron fiber orientation and may usefully complement the current standard-of-care for diagnostic or pre-surgical imaging in TLE.

4.3. Methods

4.3.1. Participants

Nine TLE patients (four female and five male, mean age \pm standard deviation = 33 ± 12 years) and nine healthy volunteers (four female and five male, mean age \pm standard deviation = 26 ± 6 years) were recruited for this study, which was approved by the health sciences research ethics board at Western University. Informed consent was obtained from all participants prior to their recruitment. The following inclusion criteria were used to determine eligibility for the TLE cohort: all patients (a) had a history of epilepsy, (b) underwent radiological and/or comprehensive EEG assessments to identify and lateralize the epileptogenic region, and (c) were suspected to have a unilateral seizure focus in the

temporal lobe. Three patients in the TLE cohort underwent unilateral temporal lobectomy after imaging and post-surgical pathology confirmed the presence of MTS; they are herein referred to as the “confirmed MTS” subgroup, while the other six patients are referred to as the “MR-negative” subgroup. Clinical and demographic information for the patient participants is shown in Table 4-1.

Table 4-1: Clinical characteristics of patients with left and right temporal lobe epilepsy.

ID	Age	Sex	Handedness	Scalp EEG	Intracranial EEG	Ipsilateral Side	1.5T MRI Radiological Findings (T ₁ and T ₂)	Post-Surgical Pathology
1	42	M	R	L TLE	N/A	L	MTS	MTS+
2	30	F	R	L TLE	N/A	L	MTS	MTS+
3	22	M	R	L TLE	N/A	L	MTS	MTS+
4	59	M	R	L TLE	N/A	L	Smaller left hippocampus compared to right	N/A
5	23	F	R	L TLE	L TLE	L	N/A	N/A
6	31	F	R	L TLE	L TLE	L	1.2 cm possible polyp in nasal cavity	N/A
7	38	F	R	R TLE	R TLE	R	Chronic mucosal thickening in the paranasal sinuses	N/A
8	26	M	L	R TLE	N/A	R	Apparent cyst near right lateral ventricle with stable appearance	N/A
9	28	M	R	L TLE	N/A	L	Slightly thicker cortex and less myelination in left temporal pole compared to right	N/A

EEG-Electroencephalogram, **L**-Left, **R**-Right, **TLE**-Temporal Lobe Epilepsy, **N/A**-Not

Available, **MTS**-MTS Detected, **MTS+**-MTS Confirmed Surgically

4.3.2. MRI Acquisition and Processing

Participants were scanned using a 3T full-body MRI system (Siemens Prisma) with a 32-channel head coil. The protocol consisted of two anatomical MRI scans followed by two dMRI scans for separate DTI and μ FA acquisitions. The first anatomical scan was a T_1 -

weighted magnetization-prepared rapid acquisition with gradient echo (MPRAGE) sequence with repetition time/echo time (TE/TR) = 2.3/2400ms and inversion time = 1.06s, and the second anatomical scan was a T_2 -weighted sequence with TE/TR = 564/3200ms. Both the T_1 - and T_2 -weighted scans had a field-of-view (FOV) = 240x256mm², 0.8mm isotropic voxel size, and used rate 2 generalized auto-calibrating partially parallel acquisitions (GRAPPA). The DTI scan used a multiband echo-planar imaging (EPI) sequence with TE/TR = 99/5500ms, rate 2 GRAPPA, FOV = 222x222mm², and 1.6mm isotropic voxel size to acquire 6, 36, and 60 linear tensor-encoded (LTE) volumes at b-values of 0, 1000, and 2000s/mm², respectively, with a total scan time of 9 minutes. The μ FA scan used a multiband EPI sequence with TE/TR = 92/4900ms, rate 2 GRAPPA, FOV = 229x229mm², and 1.8mm isotropic voxel size to acquire 8 LTE volumes at b=2000s/mm² and 3, 6, and 16 spherical tensor-encoded (STE) volumes at b=100, 1000, and 2000s/mm², respectively, with a total scan time of 3 minutes. The μ FA scan was performed twice, first with anterior-to-posterior and then with posterior-to-anterior phase encoding directions, doubling the scan time to approximately 6 minutes. Principal component analysis denoising and Gibbs' ringing artifact correction were performed on the dMRI volumes with the *dwidenoise* [124], [180] and *mrdegibbs* [151] toolboxes from Mrtrix3 [152] and the data were then corrected for EPI readout and eddy current distortions using *topup* [181] and *eddy* [121] from FSL [182].

4.3.3. Hippocampus Segmentation

A deep-learning surface-based hippocampus unfolding pipeline (*Hippunfold v0.5.1* [183]) was used to segment the hippocampus into subiculum (SB), cornu ammonis (CA) 1-4, and dentate gyrus (DG) subfields, using the T_2 -weighted volume as input. To reduce the

number of comparisons during analysis, some of the subfields were combined to form distinct subregions based on the following three International League Against Epilepsy (ILAE) histopathological HS classifications: HS ILAE Type 1 is defined as severe neuron loss and gliosis primarily in CA1 and CA4; in Type 2 loss and gliosis predominate in CA1; and in Type 3 they predominate in CA4 [178]. Although significant cell loss is observed in CA2 and/or CA3 in some TLE patients, these findings are not consistent across any of the HS ILAE types [178] so these adjacent regions were combined into one subregion. The CA4 subfield was combined with the adjacent DG since cell loss scores in the DG tend to be higher in CA4-predominant HS type 1 and type 3 than in type 2 [178]. The CA1 subfield was not merged with any others as it is of interest in HS type 1 and type 3.

4.3.4. Estimation of dMRI Parameters

To ensure that all dMRI metrics were mapped to the same coordinate system, the DTI volumes were registered to the μ FA image space using the linear registration tool FLIRT [184] from FSL. MD and FA maps were computed by fitting the dMRI data with $b \leq 1000 \text{ s/mm}^2$ from the DTI scan to the DTI signal representation using a weighted linear least-squares method [47], [185]. μ FA maps were computed by performing a joint fit between the entire set of LTE and STE data from the μ FA scan to the second order cumulant signal representation as described by Arezza *et al* [81]. The T_1 -weighted image volumes were registered to the μ FA space and then the inverse transformations were used to register the MD, FA, and μ FA maps to the anatomical space. To ensure good registration quality, outlines of the hippocampal subregions were overlaid on top of the registered MD, FA, and μ FA maps and were visually inspected.

4.3.5. Statistical Analysis

For each TLE patient, the mean MD, FA, and μ FA were measured in the ipsilateral and contralateral sides of each of the four hippocampal subregions and full hippocampus, and the volume of each subregion was measured by computing the sum of the number of voxels in the region. The mean and standard deviation of each of the four measurements of interest, across all patients, were computed for the ipsilateral and contralateral sides. In the healthy volunteer cohort, the same measurements were made in the left and right sides for each subfield, as well as average measurements spanning both sides of the brain. For each metric in each subregion, a paired t-test was performed to test for significant differences between the ipsilateral and contralateral sides in the TLE cohort, and an unpaired t-test was performed to test for significant differences between the ipsilateral side of the TLE group and the average of the left and right sides in the healthy group. The Bonferroni correction was applied to account for multiple comparisons; since four metrics were compared, the significance threshold was reduced from 0.05 to 0.0125.

To quantify asymmetries between the two hemispheres, the percentage differences between the ipsilateral and contralateral measurements in the TLE group were computed in each subregion and in the whole hippocampus for each patient using the following equation:

$$2(X_{ipsilateral} - X_{contralateral}) / (X_{ipsilateral} + X_{contralateral}) * 100\% \quad (4.1)$$

where X is the measurement of interest. It was hypothesized that volume, FA, and μ FA may be reduced, and MD may be elevated, in some ipsilateral regions compared to their respective contralateral counterparts due to tissue atrophy, gliosis, and changes to microstructure. Notably, asymmetries may be more likely to be observed in the CA1 and CA4/DG subregions that are predominantly affected in HS than in the SB and highly

variable CA2/3 subregions. For the healthy group, asymmetry was measured within subregions and in the whole hippocampus by comparing the left and right sides.

4.4. Results

Example sagittal and coronal T_1 - and T_2 -weighted images from one of the healthy volunteers are depicted in Figure 4-1 with the four hippocampal subregions outlined. All hippocampal segmentations were manually inspected for accuracy in delineating the hippocampal tissue and subfields. Coronal slices of T_1 -weighted MRI, MD, FA, and μ FA from a TLE patient with confirmed MTS are depicted in Figure 4-2 for comparison. Ipsilateral and contralateral measurements of volume (normalized against the mean contralateral volume), MD, FA, and μ FA are plotted in Figure 4-3 for all subregions, in addition to average measurements spanning both the right and left side for all subregions in healthy volunteers. Notably, MD was significantly elevated and μ FA was significantly reduced in the ipsilateral CA4/DG region relative to the contralateral side in TLE patients, with respective p-values of 0.012 and <0.01 . Compared to the average values in the healthy cohort, ipsilateral MD was significantly elevated in every subregion except CA1, and ipsilateral μ FA was significantly reduced in every subregion. Although the mean ipsilateral volume was reduced relative to the contralateral side in all four subregions and in the full hippocampus in the TLE cohort, this metric varied considerably from patient to patient and the difference was not statistically significant in any region. However, ipsilateral volume was significantly reduced in every region except SB relative to average measurements in the healthy cohort. For the FA metric, no significant asymmetries were observed in the patients in any of the subregions.

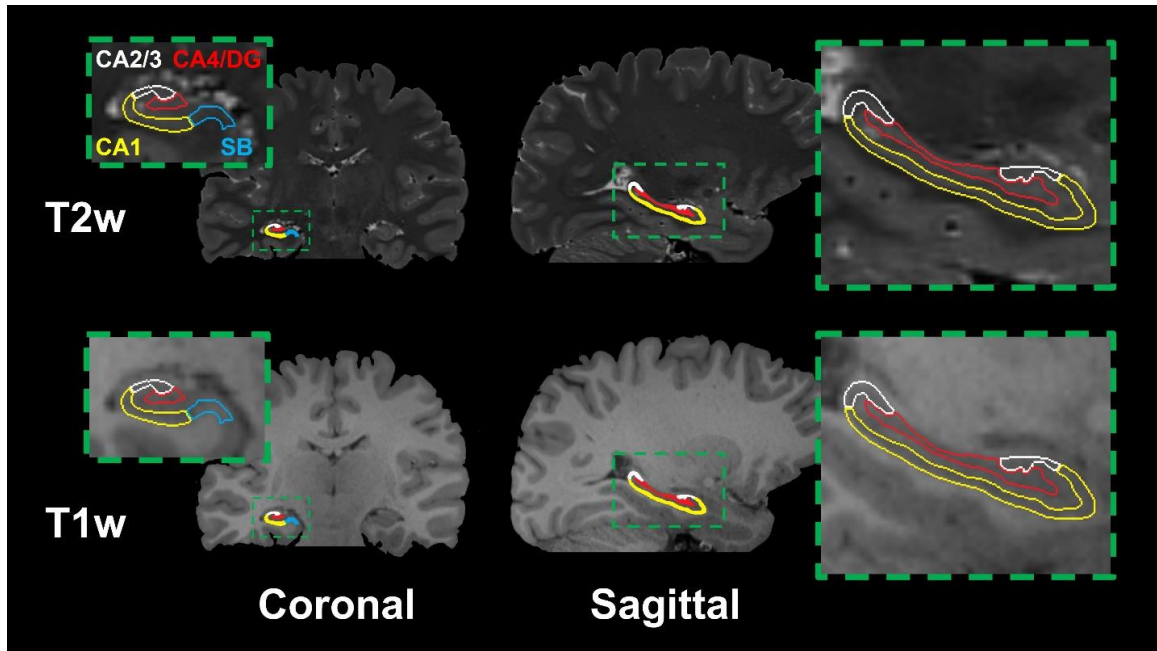


Figure 4-1. Sagittal and coronal T₁-weighted (top) and T₂-weighted (bottom) MR images from a healthy volunteer with insets highlighting the four hippocampal subregions used in this study: the subiculum (SB), cornu ammonis 1 (CA1), cornu ammonis 2 and 3 (CA2/3) and cornu ammonis 4 plus dentate gyrus (CA4/DG). Note that only the right hippocampus is labeled although both hippocampi were analyzed.

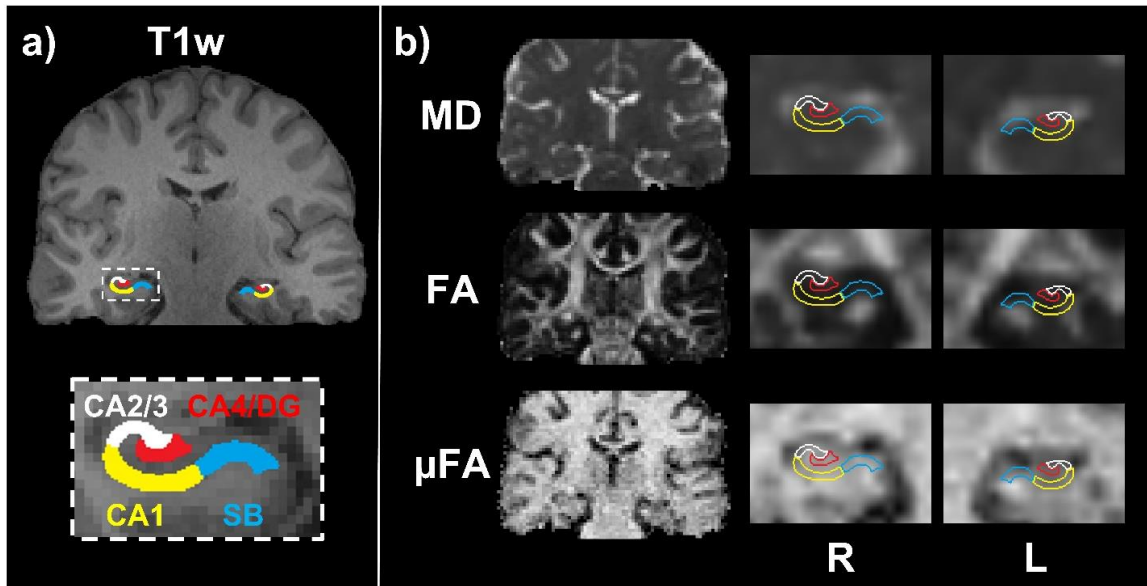


Figure 4-2. (a) Example T₁-weighted coronal image from a TLE patient with confirmed MTS, with the four hippocampal subregions highlighted. (b) MD, FA, and μ FA coronal slices from the same patient before registration to T₁-space (left), and after registration to T₁-space and interpolation (right) depicting the ipsilateral and contralateral hippocampal regions. Note that for this patient, the left side (L) is the ipsilateral side and the right side (R) is the contralateral side.

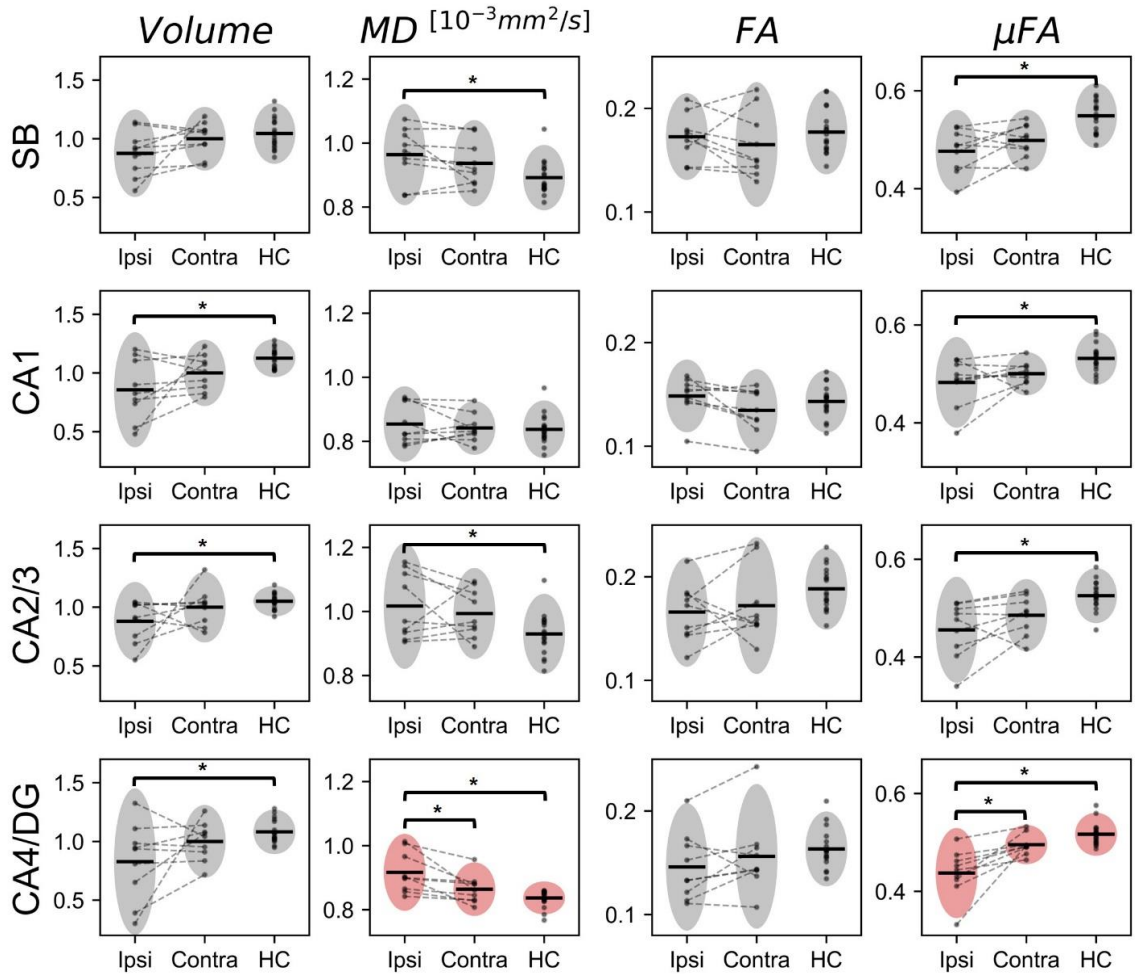


Figure 4-3. Volume (normalized against the mean contralateral volume), MD, FA, and μFA measurements in the ipsilateral and contralateral sides of each of the four hippocampal subregions across 9 TLE patients, plus mean measurements of both hemispheres across 9 healthy control volunteers (HC). The horizontal black lines depict the mean measurement across the cohort, and the gray ovals highlight a region spanning two standard deviations above and below the mean. The two plots with pink ovals highlight significant MD ($p=0.012$) and μFA ($p<0.01$) asymmetries in the TLE cohort.

To further investigate asymmetries in the CA4/DG subregion, and to compare these asymmetries with full-hippocampus measurements, the percentage differences between ipsilateral and contralateral measurements in CA4/DG and in the full hippocampus were plotted in Figure 4-4. Overall, the mean percentage difference between the ipsilateral and contralateral measurements in the CA4/DG region was -24.4% for volume, +5.8% for MD, -6.6% for FA, and -12.9% for μ FA; in the full hippocampus the mean percentage difference between ipsilateral and contralateral measurements was -16.5% for volume, +2.7% for MD, +3.3% for FA, and -5.9% for μ FA.

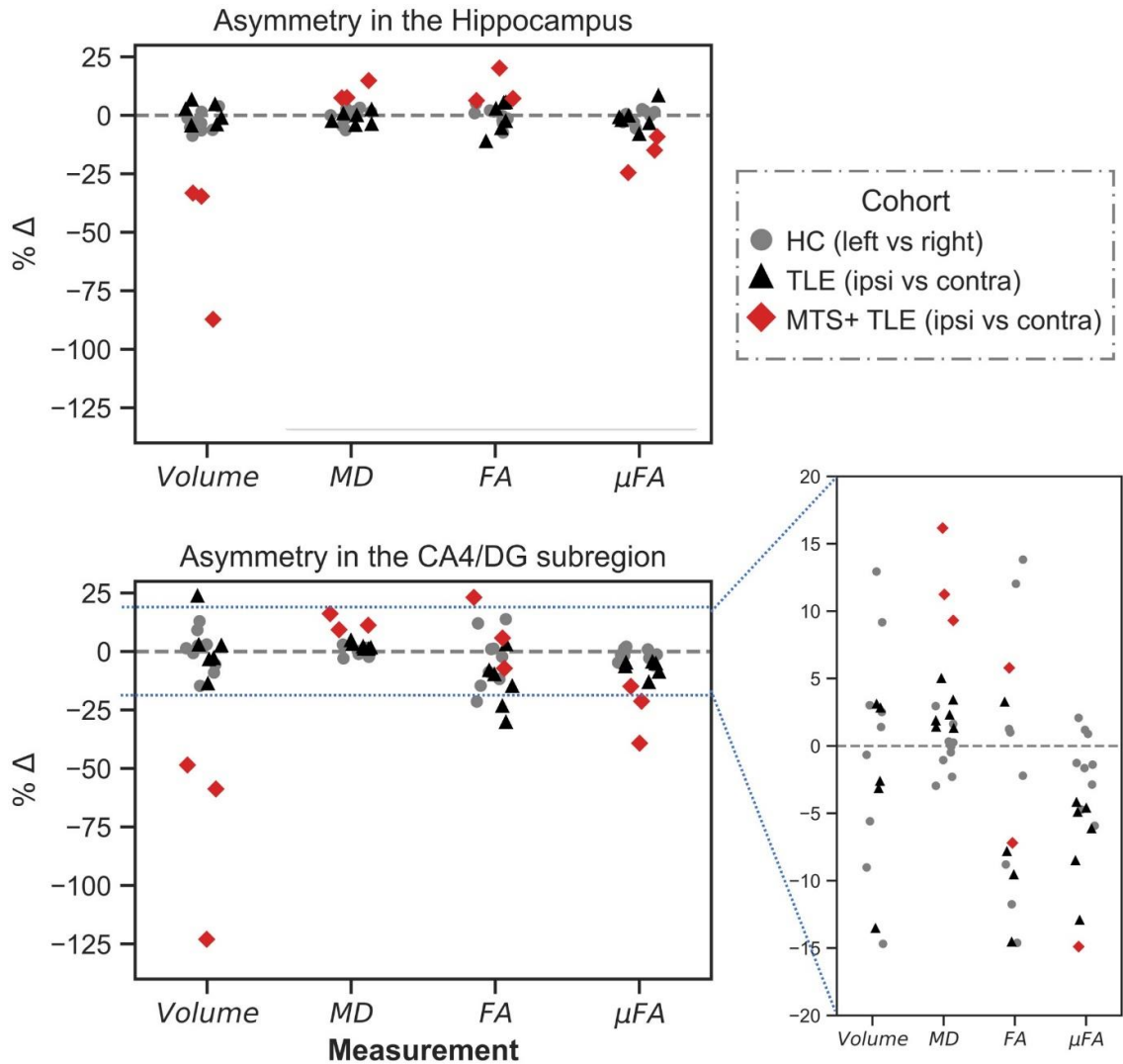


Figure 4-4. Percentage difference (% Δ) between ipsilateral and contralateral measurements of volume, MD, FA, and μ FA in the full hippocampus (top) and CA4/DG region (bottom) in unilateral TLE patients, and % Δ between left and right measurements in 9 healthy control volunteers (HC).

All three patients with confirmed MTS were found to have reduced volume and μ FA and increased MD in both the full hippocampus and the ipsilateral CA4/DG subregion relative to the contralateral side. Only one of these patients had reduced ipsilateral FA in CA4/DG, and none had reduced ipsilateral FA in the full hippocampus. Of the six MR-

negative patients, only three had reduced volume in ipsilateral CA4/DG and in the full hippocampus relative to the contralateral side. Five had reduced ipsilateral FA in CA4/DG and four had reduced ipsilateral FA in the full hippocampus. All six MR- patients had reduced μ FA and increased MD in the ipsilateral CA4/DG subregion relative to the contralateral side, but only five had reduced μ FA and increased MD in the ipsilateral full hippocampus. Generally, greater asymmetries were observed between hemispheres in the CA4/DG subregion than across the entire hippocampus in the TLE cohort.

4.5. Discussion

In this preliminary study, the dMRI metrics of MD, FA, and μ FA were measured in several hippocampal subfields, and compared to a volumetric measurement, to assess whether they demonstrate sensitivity to unilateral hippocampal abnormalities in TLE patients. This study is the first to apply μ FA imaging to the study of TLE. It was observed that MD was significantly elevated and μ FA was significantly reduced in the ipsilateral CA4/DG region, relative to the contralateral side, in all patients. This subregion is affected by severe cell loss and gliosis in TLE patients with ILAE HS types 1 and 3. The increased ipsilateral MD is consistent with other diffusion MRI studies of temporal lobe epilepsy [173], [186]–[189]. In particular, Goubran *et al* observed a strong negative correlation between MD and cell density in CA4/DG [174]. μ FA values were more asymmetric (between hemispheres) than were MD values in the CA4/DG region, suggesting that it is more sensitive to hippocampal abnormalities. Although the mean CA4/DG volume asymmetry across patients was greater than those of the dMRI metrics, a decreased ipsilateral volume in the region correctly predicted the side of the epileptic focus in only six of nine patients, while MD and μ FA measurements demonstrated asymmetry in the CA4/DG that was consistent with the EEG results in all nine patients.

We hypothesize that the reduced ipsilateral μ FA stemmed from the loss of axons that invariably occurs when neurons die. Notably, axons are more sensitive to homeostatic imbalances than cell bodies, and so are generally lost earlier: when under stress axons can degenerate while the cell body remains [190]–[193]. Accordingly, these results, although from a small sample, suggest that μ FA may be an early marker of mesial temporal sclerosis.

4.5.1. Confirmed MTS vs. MR-Negative TLE

Both full hippocampus and CA4/DG-specific asymmetries in region volume, MD, and μ FA correctly lateralized the epileptic focus in all three patients with confirmed MTS. These patients exhibited considerable unilateral hippocampal atrophy which, when combined with concordant results from EEG and other clinical testing, made them candidates for anterior temporal lobectomy procedures. All three patients with confirmed MTS had total hippocampal volume asymmetries greater than 30% (prior to surgery) and CA4/DG volume asymmetries greater than 45%, while the six MR-negative patients had total hippocampal volume asymmetries of <10% and CA4/DG volume asymmetries of <20%. The confirmed MTS patients also had the greatest MD and μ FA asymmetries.

The inability of volume asymmetries to lateralize the epileptogenic zone in the MR-negative cohort highlights the need for supplementary imaging techniques in the TLE clinical workflow. In the MR- subgroup, the full hippocampus and CA4/DG volume asymmetries correctly lateralized the epileptic focus in only half of the patients. Right-left hemispheric asymmetry of hippocampal volume occurs in healthy subjects and is not necessarily indicative of pathology or injury [194]. In contrast, diffusion metrics are linked to microstructural changes that suggest neuron damage or gliosis, perhaps giving said metrics better specificity to unilateral hippocampal abnormalities relevant to TLE. The results of this work support this theory as MD and μ FA asymmetries in CA4/DG correctly

lateralized the epileptic focus for all six MR-negative patients, regardless of whether the ipsilateral side was in the left or right hemisphere, and regardless of whether CA4/DG volume was reduced or elevated in that side.

4.5.2. Microscopic Fractional Anisotropy vs. Fractional Anisotropy

Since both FA and μ FA index water diffusion anisotropy, they are particularly comparable. Mean FA values typically fell in the 0.1-0.2 range across all hippocampal subregions and were consistently lower than mean μ FA values, which fell in the 0.4-0.5 range. This discrepancy likely resulted from crossing and fanning fibers in the hippocampus, which attenuate FA measurements but do not affect μ FA. The mean values for both anisotropy metrics were consistent with the results of Yoo *et al* [147], in which mean FA and μ FA values of 0.2 and 0.47, respectively, were observed in the hippocampi of healthy volunteers.

Although CA4/DG was the only region in which a statistically significant asymmetry in μ FA was observed in the TLE cohort, mean ipsilateral μ FA was consistently reduced relative to both the contralateral and average healthy control μ FA across all four hippocampal subregions (Fig. 3). FA asymmetry in the TLE group was not statistically significant in any of the subregions and was inconsistent across regions. Given that FA values were significantly lower in all subregions relative to μ FA values, and that no significant FA asymmetries were observed, it is likely that the sensitivity of FA in detecting hippocampal abnormalities in TLE is suppressed by its lack of specificity to neuron fiber microstructure and that μ FA is a more suitable measure of diffusion anisotropy in brain regions containing crossing fibers.

4.5.3. Limitations

This preliminary work was limited by the small size of the unilateral TLE patient cohort. Although μ FA and MD measurements were reliably asymmetric in CA4/DG, future work should include larger patient cohorts to validate these findings and to potentially elucidate asymmetries in other subregions, such as CA1.

Since ILAE HS type 1 is the most common subtype of HS, accounting for 60-80% of TLE-HS cases [178], [195], [196], it was expected that asymmetries might present in the CA1 and CA4/DG regions. However, no significant asymmetries were observed in CA1 in any of the metrics. It may be the case that MD and μ FA are more sensitive to abnormalities in the CA4/DG region, but the small sample size may have affected the results.

The spatial resolutions of the dMRI volumes acquired in this study (1.8 mm isotropic for μ FA) are suboptimal for visualizing hippocampal subfields [197], so some partial volume effects near the boundaries between subregions and near CSF likely affected the results. Since the SB, CA1, and CA2/3 subregions encompass the periphery of the hippocampus, they could be more susceptible to partial volumes of extra-hippocampal brain tissue or CSF; contrarily, the CA4/DG region lies in the center of the hippocampus and would only be affected by partial volumes of other hippocampal subregions. The significant asymmetries in MD and especially μ FA in CA4/DG demonstrate the potential for dMRI in lateralizing the epileptic zone in TLE and demonstrate the increased utility of μ FA over FA in studying the hippocampus. In future work, the spatial resolution could be improved at the expense of increased scan duration; the μ FA protocol used in this study required 3 minutes to achieve 1.8 mm resolution, but Yoo *et al* demonstrated a μ FA protocol with 1.5 mm isotropic resolution that could be acquired in 15 minutes [147]. To

counter the increased scan time needed for higher resolution, the field-of-view and number of slices could be reduced to capture a smaller subvolume of the brain containing the hippocampus. Additionally, techniques to mitigate CSF partial-volume effects, such as a recently proposed free water elimination μ FA protocol [131], could be employed.

4.6. Conclusions

This study demonstrated that the combination of hippocampal subfield segmentation with μ FA and MD imaging may be helpful for lateralizing the epileptogenic zone in patients with unilateral TLE. Assuming the poorer surgical outcomes experienced by patients with MR- TLE are in part due to poorer identification of the epileptic focus, then dMRI techniques that can complement the current techniques for lateralizing and localizing the epileptic focus may be able to improve surgical outcomes in these patients.

Both the DTI and μ FA protocols in this work are clinically feasible and could easily be included in a clinical workflow, as both scans were performed at a clinical field strength of 3T and each only required 6 minutes or fewer of total scan time (as the $b=2000\text{s/mm}^2$ acquisitions in the DTI scan were redundant). To further optimize the protocol, MD and FA could be estimated from a μ FA scan by fitting the low b -value data ($<1000\text{s/mm}^2$) to the diffusion tensor signal representation, eliminating the need for a separate DTI scan, though this was not possible in this work because only STE scans were acquired at the lower b -values.

Chapter 5

5 Conclusions

Microscopic fractional anisotropy is a powerful tool that can probe brain microstructure by quantifying water diffusion anisotropy. Since μ FA is not affected by the orientation of neurites, such as crossing axon fibers in WM and incoherently arranged dendritic branches in pyramidal and granular neurons of the hippocampus, it may serve as a useful biomarker to characterize pathological microstructural changes or abnormalities in neural tissue. Despite its potential, μ FA imaging is still in the early research stages. As of 2019, the number of MRI scanners per 1 million population in Canada was only 10.4 [198], so scan time is limited and new techniques like μ FA have to demonstrate clinical benefit to warrant their usage.

The overarching goal of this Thesis was to assess the feasibility and efficacy of μ FA imaging for clinical usage. In Chapter 2 it was shown that a data set acquired within a clinically viable scan time could be used to generate μ FA maps with high repeat measurement reliability in WM brain regions. Furthermore, the powder average kurtosis signal representation used to estimate μ FA can be rapidly computed via least squares, and yields other valuable metrics like MD and K. The FWE method investigated in Chapter 3 demonstrates the potential for tissue-specific μ FA imaging, which could improve the metric's specificity to microstructural abnormalities in regions contaminated by CSF partial volumes. Finally, Chapter 4 provides an example of a clinical use case by demonstrating the benefit of μ FA imaging over traditional DTI and relaxation-weighted MRI in patients with unilateral TLE.

5.1. Limitations and Suggestions

Though many of the limitations of the work presented in this Thesis are discussed in the previous chapters, the following subsections investigate some of the broader limitations in greater detail, and how they can be addressed in future studies.

5.1.1. Diffusion Time-Dependence

The techniques presented in this work to estimate μFA rely on a joint fit between STE and LTE dMRI data and assume that the apparent mean diffusivity is equal regardless of encoding scheme (i.e., $D_{STE} = D_{LTE}$). This assumption holds true if the diffusion time is long enough that steady-state measurements are achieved, or if the STE and LTE sequences are calibrated to ensure they have the same effective diffusion time. Diffusion time differences between the LTE and STE waveforms, or between the different gradient channels in the STE sequence, may have introduced biases in μFA .

To demonstrate how diffusion time differences between LTE and STE waveforms can bias measurements, consider dMRI data acquired such that $D_{STE} > D_{LTE}$ because of effective diffusion time inconsistencies. The joint fit will yield a mean diffusivity estimate that falls between the true values (i.e., $D_{STE} > D_{fit} > D_{LTE}$), and this deviation from the true values can affect estimates of K_{STE} , K_{LTE} , and μFA . Table 5-1 depicts a scenario in which a 6% difference between D_{STE} and D_{LTE} results in an 11% difference in the measured μFA value from jointly fitting the data to the powder kurtosis representation.

Table 5-1. Example diffusion MRI data in which the LTE and STE waveforms probe different diffusion times, resulting in different apparent diffusivities. When a joint fit to the powder average diffusion kurtosis representation is performed, the resulting μ FA estimate is biased.

<i>Metric</i>	<i>True value</i>	<i>Estimate from joint fit</i>
D_{LTE}	$7.5 * 10^{-3} \text{ mm}^2/\text{s}$	$7.75 * 10^{-3} \text{ mm}^2/\text{s}$
D_{STE}	$8 * 10^{-3} \text{ mm}^2/\text{s}$	
K_{LTE}	0.2	0.215
K_{STE}	0.1	0.087
μ FA	0.34	0.38

Potential diffusion time differences between the STE and LTE sequences were not investigated in this Thesis, but any biases resulting from such inconsistencies would have been consistently replicated (i.e., the same bias would be present in both the test and retest measurements in Chapter 2, and between ipsilateral and contralateral measurements in Chapter 4).

Potentially more deleterious to measurement reliability are effective diffusion time differences between the different gradient channels in the STE sequence. If the G_x , G_y , and G_z gradient waveforms in the STE sequence probe different diffusion times, it is possible to introduce a rotational bias into measurements that changes depending on how the subject is positioned inside the MRI scanner. Such a bias could limit the repeat measurement reliability of μ FA and could confound comparisons made between multiple subjects. To assess this bias, a Monte Carlo simulation was performed using Camino software in which infinitely long cylinders were simulated with radii of $1 \mu\text{m}$, a water diffusivity of $3 * 10^{-3} \text{ mm}^2/\text{s}$, and an extra-cylinder volume fraction of 0.25. The individual G_x , G_y , and G_z

waveforms from the STE sequence were then separately used to generate signals from the simulated geometry using a b-value of 667 s/mm^2 , which represents their individual contributions to the STE sequence with a b-value of 2000 s/mm^2 . These gradients were applied in a direction perpendicular to the cylinders and then separately applied parallel to the cylinders. All three gradient waveforms produced the same signal when applied parallel to the cylinders (<1% difference), which is the result of the simulated water molecules experiencing free diffusion along that direction. However, signal varied in the perpendicular direction, in which diffusing water molecules interact with the cylinders and experience restricted and hindered diffusion; in this direction the G_x waveform yielded a signal that was $\sim 7.3\%$ greater than that of the G_y waveform, and $\sim 4.5\%$ greater than that of the G_z waveform. Future studies should aim to calibrate the sequences so that the effective diffusion times of the G_x , G_y , and G_z gradient waveforms in the STE sequence match the effective diffusion time of the LTE sequences.

5.1.2. Sample Size and Demographics

The total sample size for each of the healthy volunteer cohorts in Chapter 2 and Chapter 3 ($n = 4$), and the sample size for the epilepsy and healthy volunteer cohorts in Chapter 4 ($n = 9$) were small. Furthermore, all healthy volunteer cohorts were primarily comprised of graduate students, potentially introducing selection biases related to age, education level, location, and other factors. The results of this Thesis work should thus be considered a proof-of-concept of methods (Chapter 2, Chapter 3) and a potential application for these methods (Chapter 4) that should be investigated further in a larger and more diverse cohort that better represents the global population.

5.1.3. k-space Trajectory

The typical single shot EPI sequence used in dMRI has several drawbacks, many of which are discussed in Appendix B. Notably, the k-space sampling trajectory conferred by the sequence introduces two main issues: (1) it samples k-space non-uniformly, with greater temporal separation between adjacent points in the phase-encoding direction than frequency encoding direction, and (2) it begins sampling at higher spatial frequencies, rather than at the center of k-space, necessitating longer TEs. The non-uniform sampling introduces artifacts in the phase-encoding direction, while the higher TE reduces SNR. One potential solution for these limitations is to implement spiral k-space trajectories instead of the typical “crisscross” path. Spiral trajectories begin at the center of k-space (i.e., $k_x, k_y \approx 0$) and can achieve lower TEs and higher SNR while also sampling k-space more uniformly in time and introducing fewer contaminating artifacts [199]. Though spiral imaging comes with a tradeoff in resolution (i.e., a conventional EPI sequence will have slightly greater effective resolution than a spiral sequence at the same nominal resolution^{*}), this can easily be overcome by sacrificing some of the gained SNR in exchange for better resolution. Another drawback of spiral imaging is that it is more sensitive to field inhomogeneities and gradient imperfections along all sampling directions, potentially necessitating the use of concurrent field monitoring for correction [200].

5.1.4. Microscopic Kurtosis

The conventional and FWE techniques presented in this work assume that the total effective kurtosis arises from two sources: K_{iso} due to variance in apparent diffusion

* Nominal resolution is defined here as the width of a voxel in the x or y direction in image space, while effective resolution is defined as the full-width-at-half-maximum of the point spread function along x or y .

magnitude, and K_{aniso} due to directional anisotropy. A third source of non-Gaussian diffusivity is microscopic kurtosis (μK), which describes non-Gaussian diffusivity arising from restricted diffusion and tissue disorder due to microscopic hindrances like membranes and organelles, and exchange between water-containing compartments [94], [201]. A recent study has shown that μK is non-negligible in the human brain, including the WM and hippocampus regions relevant to this Thesis work [161].

Though disentangling μK from other kurtosis sources may provide clinical benefit, the μFA technique presented in this work demonstrated good repeat measurement reliability in WM (Chapter 2) and was sensitive to CA4/DG asymmetries in unilateral TLE patients (Chapter 4), evidence for its potential utility despite the assumption that μK is negligible. In future work, it may be desirable to compare the K_{iso} and K_{aniso} measurements derived from the methods presented herein with those derived from a technique that incorporates μK (such as CTI) to quantify potential biases.

5.1.5. Protocol Optimized for White Matter

The optimization performed in Chapter 2 was based on signal data from a frontal WM region. WM is primarily composed of axon fibers, making it a prime target for measurements of water diffusion anisotropy like FA and μFA . However, the optimal b-value and ratio of LTE to STE acquisitions may differ for other tissue types such as cortical GM and the deep GM structures. The sequence used in the TLE study (Chapter 4) may have been suboptimal for imaging the hippocampus, and it is likely that changing the parameters could have improved image quality and SNR.

If a rapid protocol for a study involving a non-WM ROI is desired, it may be desirable to perform another optimization to determine the best ceiling b-value and ratio of

LTE to STE scans for that region. Monte Carlo simulations of different geometries with added noise may be a sufficient substitute for true *in vivo* data. If scan time requirements are less prohibitive, optimization can be bypassed altogether in favor of a more thorough protocol in which more than three b-shells are probed and excess directions/acquisitions are obtained.

5.1.6. Fitting Errors in the Free Water Elimination Algorithm

The algorithm presented in Chapter 3 to fit dMRI data to the FWE signal representation consisted of two iterative methods and each was run for exactly 100 iterations with no other stopping criteria. To improve robustness in future studies, stopping criteria can be implemented to terminate the iterative fitting procedures after an optimal number of iterations. Repeat measurement reliability assessments should also be performed to gauge the algorithm's robustness and reliability.

5.1.7. Why no FWE in the TLE study?

The TLE study described in Chapter 4 did not make use of the FWE technique despite the high likelihood of CSF partial volumes affecting measurements in the hippocampus. This was due to the fact that the projects described in Chapter 3 and Chapter 4 were performed in parallel, and the protocol used in the TLE study was designed and implemented before the FWE technique was developed and assessed. Since only three b-shells were acquired in the TLE study (and only one of those b-shells was acquired in the STE encoding scheme), the data set was too sparse to yield high quality FWE images. Ideally, four or more b-shells are desired for FWE fitting.

Future studies observing μ FA in TLE patients can implement the FWE method to probe the following questions:

1. Does the significant μ FA asymmetry observed in CA4/DG in unilateral TLE patients arise from ipsilateral microstructural abnormalities (i.e., beading, demyelination, etc.), or from increased ipsilateral free water concentration (i.e., due to neuronal atrophy)?
2. Do CSF partial volumes confound measurements made in peripheral hippocampal subfields such as CA1 and CA2/3?

5.2. Future Work

The demonstrated sensitivity of microscopic fractional anisotropy to abnormalities in temporal lobe epilepsy (and other pathologies via the literature) supports further investigation into its potential use as a biomarker in clinical or pre-clinical applications. The high repeat measurement reliability displayed in white matter in Chapter 2 suggests that μ FA could be suitable for longitudinal studies that track the progression of disease, injury, or normal aging over time. When designing a μ FA imaging protocol, parameters can be tailored to the needs of the application. A study quantitatively assessing water diffusion anisotropy in a progressive disease like dementia, for example, may require a comprehensive protocol with high SNR to enable accurate and precise measurements for comparison across different time points. A study in which μ FA serves as a complimentary imaging tool and is only assessed qualitatively, such as one tracking the sizes of tumors over time or detecting lesions in multiple sclerosis, may instead opt for a rapid and minimalistic protocol.

The study of μ FA in temporal lobe epilepsy described in Chapter 4 was intended to serve as a preliminary assessment of μ FA as a biomarker of hippocampal abnormalities. Future works exploring μ FA in TLE should probe higher resolutions for hippocampal subfield segmentation and should acquire more b-shells and acquisitions to improve SNR

in conventional μ FA and allow for free water elimination, at the expense of increased total scan time. Surgical removal of the epileptic focus is an irreversible and highly risky procedure, so an acceptable tradeoff for pre-surgical imaging would be to prioritize image quality over acquisition time. Future studies could attempt to prospectively predict surgical outcomes in MR-negative patients based on μ FA asymmetries, or retrospectively assess if there are differences in μ FA features between patients with positive and negative surgical outcomes.

A potential future avenue for μ FA research is to incorporate the metric into multiparametric imaging models. While μ FA alone may demonstrate sensitivity to neuronal microstructure, other imaging techniques can probe different contrasts such as glucose metabolism (i.e., positron emission tomography (PET)), macrostructure (i.e., relaxation-weighted MRI), and blood flow (i.e., perfusion MRI), among others. Models that incorporate two or more contrasts together may have greater diagnostic or predictive power in clinical applications. As an example, PET is routinely used in the TLE workflow and glucose hypometabolism can correctly lateralize the epileptic focus in as many as 95% of MR-positive and 84% of MR-negative patients [202]. A model that combines relaxation-weighted MRI measures of hippocampal (or subfield) volume and T_2 signal intensity, PET intensity, and diffusion metrics such as diffusivity and μ FA, may better lateralize and localize the epileptic focus and potentially lead to better surgical outcomes.

Appendices

Appendix A: Signal-to-noise Ratio of μA^2 Estimation

This Appendix was published in *Magnetic Resonance Imaging*, volume 80, Arezza *et al*, *Rapid Microscopic Fractional Anisotropy Imaging via an Optimized Linear Regression Formulation* [81], pages 132-143, Copyright Elsevier, 2021.

The variance of μA^2 ($\sigma_{\mu A^2}^2$), assuming equal noise in STE and LTE images and that there is no covariance between the two acquisition types, can be approximated using the error propagation equation. Propagating error from equation (2.8) yields:

$$\begin{aligned} \sigma_{\mu A^2}^2 &= \left(\frac{\partial \mu A^2}{\partial S_{LTE}} \right)^2 \frac{\sigma^2}{n_{LTE}} + \left(\frac{\partial \mu A^2}{\partial S_{STE}} \right)^2 \frac{\sigma^2}{n_{STE}} \\ &= \frac{\sigma^2}{b^4} \left(\frac{n_{STE} S_{STE}^2 + n_{LTE} S_{LTE}^2}{n_{STE} n_{LTE} S_{STE}^2 S_{LTE}^2} \right) \end{aligned} \quad (A.1)$$

where σ is the noise in an STE or LTE diffusion-weighted MR image, b is the b-value, n_{LTE} is the number of LTE directions acquired, n_{STE} is the number of STE averages acquired, and S_{LTE} and S_{STE} are the mean signals in LTE and STE acquisitions, respectively. The SNR of a μA^2 image or volume ($SNR_{\mu A^2}$) can be estimated as the μA^2 metric divided by its standard deviation:

$$SNR_{\mu A^2} = \frac{\mu A^2}{\sigma_{\mu A^2}} \quad (A.2)$$

Substituting equations (2.8) and (A.1) into (A.2) yields equation (2.10):

$$\frac{\mu A^2}{\sigma_{\mu A^2}} = \frac{\frac{\ln\left(\frac{S_{LTE}}{S_{STE}}\right)}{b^2}}{\sqrt{\frac{\sigma^2}{b^4} \left(\frac{n_{STE} S_{STE}^2 + n_{LTE} S_{LTE}^2}{n_{STE} n_{LTE} S_{STE}^2 S_{LTE}^2} \right)}}$$

$$= \frac{\ln\left(\frac{S_{lin}}{S_{iso}}\right) \sqrt{n_{LTE} n_{STE}} S_{LTE} S_{STE}}{\sigma \sqrt{n_{LTE} S_{LTE}^2 + n_{STE} S_{STE}^2}}$$

To determine the optimal ratio of $\frac{n_{STE}}{n_{LTE}}$ as a function of the mean LTE and STE signal at a single b-value, we can express the above equation in terms of only n_{STE} and n_{LTE} , replacing most other terms with the constant C . We can also confine the total number of acquisitions to an integer value, N , and replace n_{STE} with $N - n_{LTE}$ to reduce the number of unknown variables in the formula. The resulting expression is:

$$\frac{\mu A^2}{\sigma_{\mu A^2}} = \frac{C \sqrt{n_{LTE}(N - n_{LTE})}}{\sqrt{n_{LTE} S_{LTE}^2 + (N - n_{LTE}) S_{STE}^2}} \quad (\text{A.3})$$

The maxima and minima of equation (A.3) can be calculated by solving for the roots of the derivative of the SNR equation:

$$\frac{d\left(\frac{\mu A^2}{\sigma_{\mu A^2}}\right)}{dn_{LTE}} = C \left(\frac{N - 2n_{LTE}}{2\sqrt{n_{LTE}(N - n_{LTE})} \sqrt{S_{STE}^2(N - n_{LTE}) + S_{LTE}^2 n_{LTE}}} - \frac{\sqrt{n_{LTE}(N - n_{LTE})} (S_{LTE}^2 - S_{STE}^2)}{2(S_{STE}^2(N - n_{LTE}) + S_{LTE}^2 n_{LTE})^{\frac{3}{2}}} \right) \quad (\text{A.4})$$

The roots of (A.4) are $n_{LTE} = \frac{NS_{STE}}{(S_{STE} - S_{LTE})}$ and $n_{LTE} = \frac{NS_{STE}}{(S_{STE} + S_{LTE})}$, the prior of which is not realizable because n_{LTE} would be negative if $S_{STE} < S_{LTE}$. Rearranging the latter yields the optimal ratio of STE to LTE acquisitions:

$$n_{lin} = \frac{NS_{STE}}{S_{STE} + S_{LTE}} = \frac{(n_{LTE} + n_{STE}) S_{STE}}{S_{STE} + S_{LTE}}$$

$$\frac{n_{STE}}{n_{LTE}} = \frac{S_{LTE}}{S_{STE}}$$

Appendix B: Challenges of dMRI

There are challenges associated with dMRI that amplify some image artifacts and necessitate various compromises to image quality. Some of these pitfalls result from the diffusion-encoding gradient waveforms, while others are associated with the EPI acquisition strategy. The main challenges associated with dMRI are summarized in this section [203], as well as techniques to mitigate them. Figure B-0-1 depicts the data acquisition and post-processing pipeline used in this work.

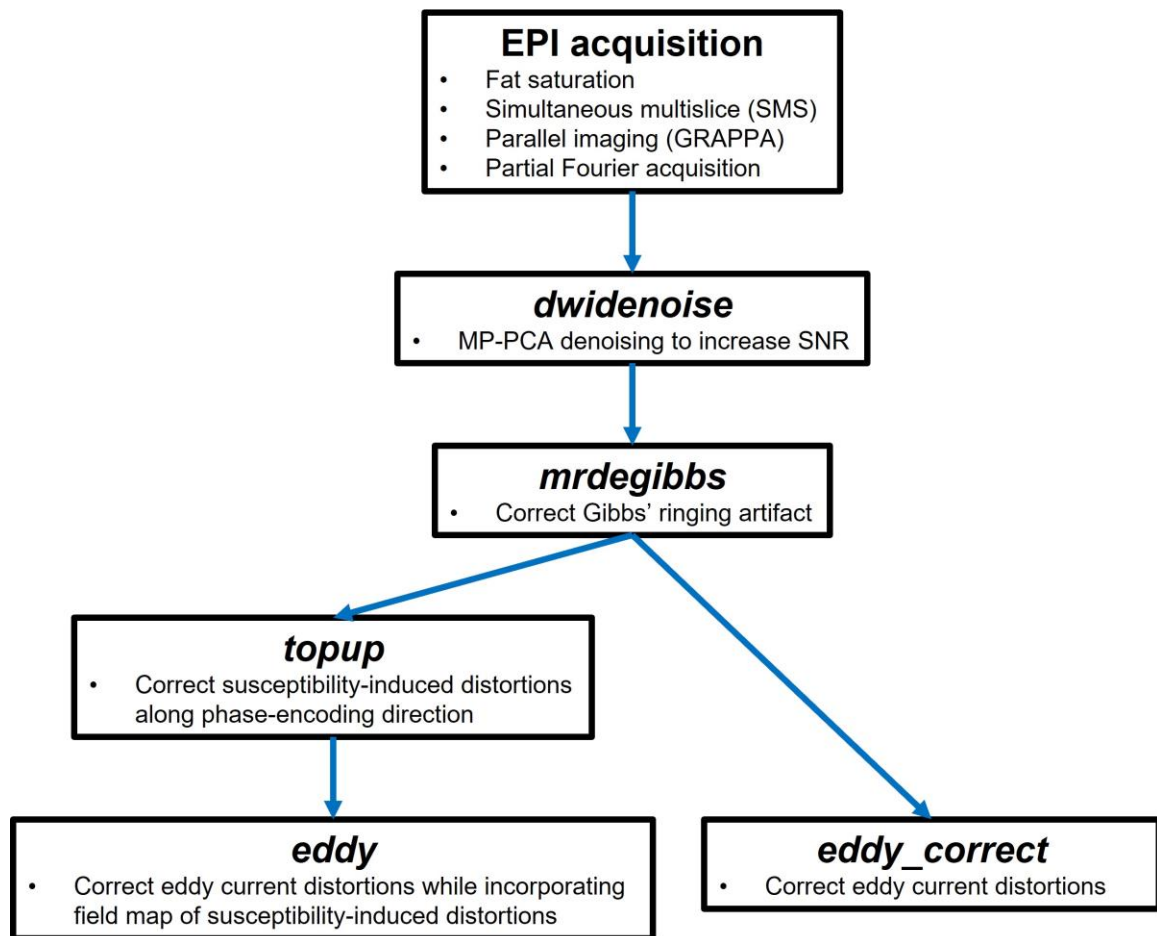


Figure B-0-1. Data acquisition and post-processing pipeline for the diffusion MRI data used in this work. For Chapter 2, *eddy_correct* was used to correct eddy current artifacts, while in Chapter 3 and Chapter 4, *topup* and *eddy* were used instead.

Sensitivity to Unwanted Motion

dMRI is highly sensitive to all forms of motion; thus, gross motion of the subject's head and physiological motion (such as cardiac pulsations and respiratory motion) confound the diffusion of water molecules that provides clinically relevant information about tissue microstructure. Though post-processing techniques can reduce the effects of unwanted motion on dMRI signals, the main strategy to desensitize dMRI to this motion is to acquire data within a very short period. The EPI acquisition strategy allows for the acquisition of an entire dMRI slice after a single excitation, during which it is expected that minimal unwanted movement occurs.

Simultaneous multislice excitation, or SMS, is a technique to reduce scan time by simultaneously acquiring two or more slices [204]. After acquisition, various techniques can be employed to separate and reconstruct the acquired slices [205]. Unlike parallel imaging techniques discussed later in this Appendix, SMS does not significantly reduce SNR [206].

Partial Fourier acquisition is a technique to reduce scan time by taking advantage of the redundancy of k-space signal data [207]. Assuming there are no phase differences in the data, k-space possesses a property called conjugate symmetry, which suggests that:

$$S(k_x, k_y) = S^*(-k_x, -k_y) \quad (\text{B.1})$$

or

$$|S(k_x, k_y)| = |S(-k_x, -k_y)|$$

In theory, only half of k-space must be sampled to generate an entire MR image. In practice, phase errors render the conjugate symmetry approximation imperfect, requiring that more

than half of k-space is sampled. For example, an acquisition using partial Fourier sampling in the k_y direction with a fraction of 6/8 would omit 25% of k-space, as depicted in Figure B-0-2. The symmetrically sampled region at the center of k-space (i.e., the low k_y region) would be used to estimate phase differences, which would then be used along with the asymmetrically sampled high k_y data to estimate the rest of k-space.

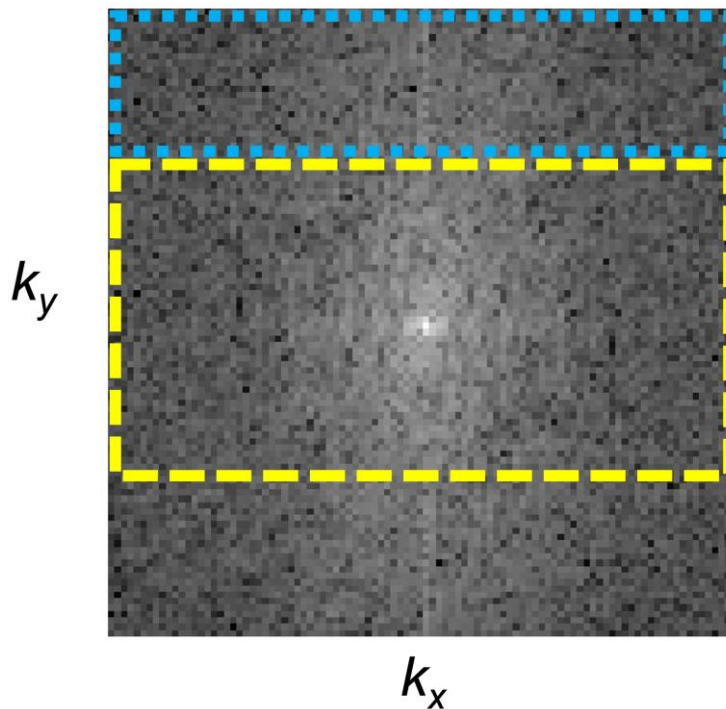


Figure B-0-2. Example k-space signal magnitude [A.U.] for a single diffusion-weighted MRI slice. The blue dotted outline highlights the region that would be asymmetrically sampled if 6/8 partial Fourier is used, while the yellow dashed outline highlights the symmetrically sampled region. Data below the yellow dashed region would be estimated by assuming conjugate symmetry with the blue dotted region while simultaneously incorporating phase error corrections derived from the yellow dashed region.

Low SNR

By design, dMRI trades SNR for diffusion-weighted contrast as the recorded signal is attenuated by both the b-value and the diffusivity of water molecules. Furthermore, dMRI gradient sequences require longer TEs to achieve high b-values and to probe long diffusion times, further reducing the measured signal due to the TE-dependent T_2 decay. These factors, along with others described in this Appendix (such as the use of parallel acquisition strategies), result in significantly lower SNR in dMRI images relative to traditional relaxation-weighted MRI techniques.

Some acquisition strategies to maximize SNR include acquiring large voxels and obtaining multiple dMRI volumes at each b-value and then averaging them together. However, the effectiveness of averaging is limited by the fact that MRI noise is governed by a Rician distribution that skews towards a positive bias in voxels with low signal [162]. In this work, a technique known as Marchenko-Pastur Principal Component Analysis (MP-PCA) denoising [124], [180] was used to improve SNR in dMRI data via the *dwidenoise* tool in MRtrix3 [152].

Principal component analysis is a technique used to analyze large datasets by reorganizing the data into principal components (PCs), which are independent linear combinations of the initial variables. An n -dimensional data set will in turn have n PCs, and they represent the linear combinations of the initial variables that explain a maximal amount of the data set's variance in descending order (i.e., the first PC contributes the most to the variance, followed by the second, etc.). Each PC is characterized by an eigenvector, which describes a line in n -space, and an eigenvalue, which describes its magnitude. In a typical multidirectional dMRI data set, most of the PCs arise due to noise and can be

identified by the fact that the noise eigenvalues are described by the Marchenko-Pastur distribution in a PCA eigenvalue histogram (see Figure B-0-3.) [180]. Removing the PCs associated with noise and then mapping the remaining PCs back into the original dMRI space enhances SNR and image quality [124].

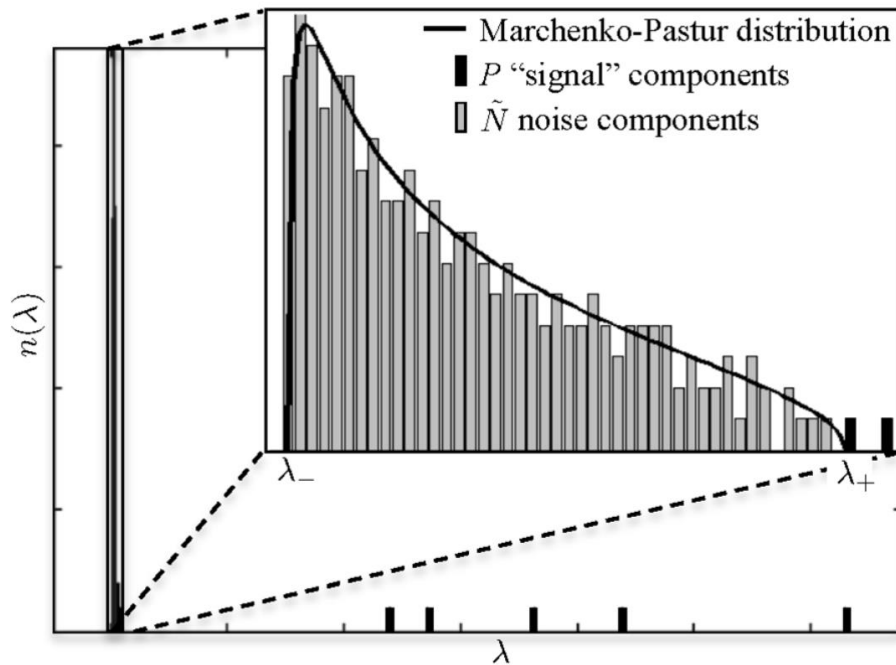


Figure B-0-3: Eigenvalue (λ) spectrum of simulated dMRI data with the Marchenko-Pastur distribution superimposed. Image adapted from “Diffusion MRI noise mapping using random matrix theory”, Veraart, J. *et al*, *Magnetic Resonance in Medicine*, 2015, with permission from John Wiley and Sons (see Appendix C).

Gibbs Ringing Artifact

To perfectly recreate a finite image from k-space data, all of k-space must be sampled. In practice, MRI data are acquired up to some maximum k_x and k_y , typically encompassing a finite rectangular portion of k-space, as depicted in Figure B-0-4. This truncation is equivalent to multiplying the entire k-space data set by a 2D rectangular (or *rect*) function.

After converting to image space using the 2D Fourier transform, the convolution theorem states that the resulting image is a convolution of the true image with a 2D *sinc* function (also depicted in Figure B-0-4). This convolution results in image blurring and an artifact known as Gibbs ringing, which manifests as oscillating fluctuations in image intensity. The single shot EPI technique is susceptible to Gibbs ringing artifacts because the width of k-space (in both the k_x and k_y directions) that can be acquired after a single excitation is limited.

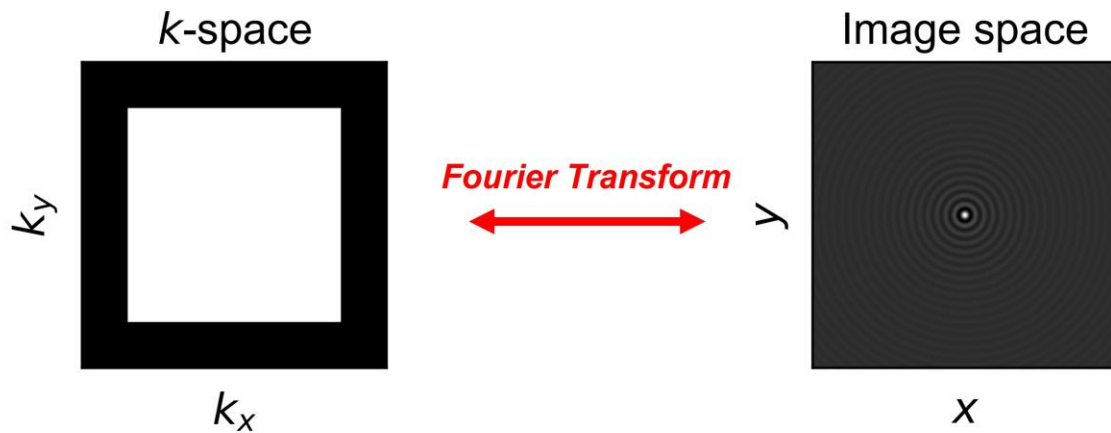


Figure B-0-4. A truncated k-space is shown on the left, with the white square representing the sampled region and the black outer region representing unsampled higher spatial frequencies. When the 2D Fourier transform is applied to this data, the result in image space (on the right) is a 2D sine cardinal (or *sinc*) function.

In this work, the Gibbs ringing artifact was corrected using the method of local subvoxel-shifts via the *mrdegibbs* tool [151] from MRtrix3. Since MR images are discrete, the severity of truncation-induced fluctuations depends on how the image is sampled. The true image and the acquired image (i.e., after convolution with a *sinc*) are equivalent at some points, known as zero crossings, as depicted in Figure B-0-5. The method of local

subvoxel-shifts involves shifting each pixel by a small distance (i.e., less than the size of a voxel) so that it is sampled at zero crossings, eliminating or mitigating ringing artifacts.

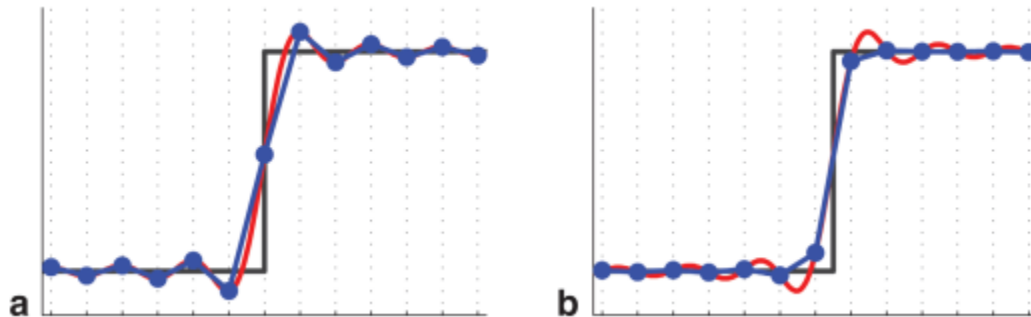


Figure B-0-5. Plot of pixel intensities of a 1D image with a single edge. The black line depicts the true image, while the red line depicts the image after convolution with a *sinc* function, the result of truncation in k-space. The blue dots depict the pixels sampled to create a discrete image. In (a), the image is sampled at suboptimal positions, capturing the signal fluctuations introduced by truncation in k-space. In (b), the image is repositioned so that it is sampled only at zero crossings, minimizing the ringing artifacts at the image edge. Image adapted from “Gibbs-ringing artifact removal based on local subvoxel shifts”, Kellner, E. *et al*, *Magnetic Resonance in Medicine*, 2015, with permission from John Wiley and Sons (see Appendix C).

Magnetic Susceptibility Distortions

As discussed in 1.5.2, magnetic susceptibility quantifies how magnetized a material will become in the presence of a magnetic field. While the unwanted phase accrual that results from susceptibility contributes to T_2^* decay, it also causes spatial distortions in images. Single shot EPI is particularly sensitive to susceptibility distortions in the phase encoding direction (G_y in Figure 1-7) because of the k-space trajectory used [208]: while adjacent points in k_x are sampled at a high rate (i.e., separated by a duration of t_{sample}) and minimal phase accrues between each sample, adjacent points at the center of k_y are sampled at a

very low rate as they are temporally separated by the time needed to acquire an entire k_x line (i.e., separated by a duration of $> nt_{sample}$ where n is the number of samples acquired along each line) or more.

Parallel imaging is a technique that can attenuate EPI distortions by reducing the readout time in the phase encoding direction at the cost of reduced SNR. In this work, the Generalized Autocalibrating Partially Parallel Acquisitions [209], or GRAPPA, technique was used. In GRAPPA, k-space is under-sampled at higher frequencies to reduce readout time but fully sampled at lower frequencies using multiple receiving coils. The fully sampled lines at low frequencies are used to estimate weighting factors for each coil, which describe how each coil distorts and displaces k-space data. The weighting factors are then used to estimate the missing k-space points before the Fourier transform is used to recover images.

EPI susceptibility distortions can be mitigated with post-processing techniques if two sets of image volumes with opposite phase-encoding trajectories (e.g., anterior-to-posterior and then posterior-to-anterior) are acquired. Given that the two acquisitions will have distortions going in opposite directions, a susceptibility field map can be estimated by gauging the similarity between the acquisitions, and this field map can then be used to correct the distortions [181]. In this work, the *topup* command from FSL was used to correct for susceptibility distortions [182].

Eddy Current Artifacts

Faraday's Law of Induction states that a changing magnetic field will induce electrical currents in conductors; these currents are referred to as eddy currents and can occur in patients as well as in MRI scanners (i.e., cables, wires, gradient coils, etc.) [210]. Eddy

currents are particularly severe when strong gradients are rapidly turned on and off, as in high b-value diffusion-encoding waveforms and in EPI, which can result in image distortion, blurring, ghosting, and other artifacts. Since dMRI volumes acquired at a b-value of 0 omit the diffusion-sensitizing gradients, they are free of the distortions caused by those waveforms. Volumes acquired at higher b-values can then be registered to the mean b=0 volume using rigid body transformations to correct for said distortions and can be further enhanced by incorporating susceptibility distortion correction into the eddy current correction algorithm [121]. The *eddy_correct* tool from FSL was used to correct for eddy current distortions in Chapter 2, while the *topup* and *eddy* tools from FSL were used to correct for susceptibility and eddy current distortions in Chapter 3 and Chapter 4.

Chemical Shift

Water and fat have different resonance frequencies and therefore accumulate phase at different rates when subjected to the same magnetic field and gradients. In EPI, significant phase differences between the two substances can accrue in the phase-encoding direction, resulting in an artifact characterized by a translation in the position of fat relative to water along the phase-encoding direction. Because dMRI is concerned with the signal arising from water, this artifact is typically corrected by suppressing the signal from fat. In this work, a fat saturation pulse was used to null the signal from fat without significantly affecting the signal from water [211]. To perform this technique, an RF pulse tuned to the resonance frequency of fat is applied before the main MRI sequence, which tips the net magnetization of fat molecules into the transverse plane and initiates the dephasing that occurs due to T_2 decay; a spoiler gradient applied after the RF pulse further amplifies the

transverse dephasing. Since the magnetization from fat is “saturated” prior to the imaging sequence, fat signal does not contribute to the recorded k-space signal.

Appendix C: Permissions for use of Copyrighted Content

Chapter 2:

From: Roopa Lingayath
Date: Tuesday, July 04, 2023 03:19 PM GMT

Dear Nico Arezza

We hereby grant you permission to reprint the material below at no charge in your thesis subject to the following conditions:

RE: Rapid microscopic fractional anisotropy imaging via an optimized linear regression formulation, Magnetic Resonance Imaging, Volume 80, July 2021, Pages 132-143, Arezza et al.

1. If any part of the material to be used (for example, figures) has appeared in our publication with credit or acknowledgment to another source, permission must also be sought from that source. If such permission is not obtained then that material may not be included in your publication/copies.

2. Suitable acknowledgment to the source must be made, either as a footnote or in a reference list at the end of your publication, as follows:

“This article was published in Publication title, Vol number, Author(s), Title of article, Page Nos, Copyright Elsevier (or appropriate Society name) (Year).”

3. Your thesis may be submitted to your institution in either print or electronic form.

4. Reproduction of this material is confined to the purpose for which permission is hereby given.

5. This permission is granted for non-exclusive world English rights only. For other languages please reapply separately for each one required. Permission excludes use in an electronic form other than submission. Should you have a specific electronic project in mind please reapply for permission.

6. As long as the article is embedded in your thesis, you can post/share your thesis in the University repository.

7. Should your thesis be published commercially, please reapply for permission.

8. Posting of the full article/ chapter online is not permitted. You may post an abstract with a link to the Elsevier website www.elsevier.com, or to the article on ScienceDirect if it is available on that platform.

Kind regards,

Roopa Lingayath
 Senior Copyrights Specialist
 ELSEVIER | HCM - Health Content Management

Dear Nico Arezza

We hereby grant you permission to reproduce the material detailed below in print and electronic format at no charge subject to the following conditions:

RE: Rapid microscopic fractional anisotropy imaging via an optimized linear regression formulation, Magnetic Resonance Imaging, Volume 80, July 2021, Pages 132-143, Arezza et al.

Proposed use: The thesis with above article embedded to be posted on ProQuest

1. If any part of the material to be used (for example, figures) has appeared in our publication with credit or acknowledgment to another source, permission must also be sought from that source. If such permission is not obtained then that material may not be included in your publication/copies.

2. Suitable acknowledgment to the source must be made, either as a footnote or in a reference list at the end of your publication as follows:

"This article was published in Publication title, Vol number, Author(s), Title of article, Page Nos, Copyright Elsevier (or appropriate Society name) (Year)."

3. This permission is granted for non-exclusive world rights in all languages.

4. Reproduction of this material is granted for the purpose for which permission is hereby given and includes use in any future editions of the work you have been granted permission to use this material in.

Kind regards,

Roopa Lingayath
Senior Copyrights Specialist
ELSEVIER | HCM - Health Content Management

Chapter 3:

Copyright © 2023 Arezza, Santini, Omer and Baron. This is an open-access article distributed under the terms of the Creative Commons Attribution License (CC BY). The use, distribution or reproduction in other forums is permitted, provided the original author(s) and the copyright owner(s) are credited and that the original publication in this journal is cited, in accordance with accepted academic practice. No use, distribution or reproduction is permitted which does not comply with these terms.

Figure 1-14 and Figure 1-16:

Copyright © 2014 Lasič, Szczepankiewicz, Eriksson, Nilsson and Topgaard. This is an open-access article distributed under the terms of the Creative Commons Attribution License (CC BY). The use, distribution or reproduction in other forums is permitted, provided the original author(s) or licensor are credited and that the original publication in this journal is cited, in accordance with accepted academic practice. No use, distribution or reproduction is permitted which does not comply with these terms.

Figure B-0-3:

JOHN WILEY AND SONS LICENSE
TERMS AND CONDITIONS
Aug 17, 2023

This Agreement between Dr. Nico Arezza ("You") and John Wiley and Sons ("John Wiley and Sons") consists of your license details and the terms and conditions provided by John Wiley and Sons and Copyright Clearance Center.

License Number	5611450174707
License date	Aug 17, 2023
Licensed Content Publisher	John Wiley and Sons
Licensed Content Publication	Magnetic Resonance in Medicine

Licensed Content Title	Diffusion MRI noise mapping using random matrix theory
Licensed Content Author	Dmitry S. Novikov, Els Fieremans, Jelle Veraart
Licensed Content Date	Nov 24, 2015
Licensed Content Volume	76
Licensed Content Issue	5
Licensed Content Pages	12
Type of use	Dissertation/Thesis
Requestor type	University/Academic
Format	Print and electronic
Portion	Figure/table
Number of figures/tables	1
Will you be translating?	No
Title	Towards Clinical Microscopic Fractional Anisotropy Imaging
Institution name	University of Western Ontario
Expected presentation date	Aug 2023
Portions	Figure 1

Figure B-0-5:

JOHN WILEY AND SONS LICENSE
TERMS AND CONDITIONS
Aug 17, 2023

This Agreement between Dr. Nico Arezza ("You") and John Wiley and Sons ("John Wiley and Sons") consists of your license details and the terms and conditions provided by John Wiley and Sons and Copyright Clearance Center.

License Number	5611451425282
License date	Aug 17, 2023
Licensed Content Publisher	John Wiley and Sons
Licensed Content Publication	Magnetic Resonance in Medicine
Licensed Content Title	Gibbs-ringing artifact removal based on local subvoxel-shifts
Licensed Content Author	Marco Reisert, Valerij G. Kiselev, Bibek Dhital, et al
Licensed Content Date	Nov 24, 2015
Licensed Content Volume	76
Licensed Content Issue	5
Licensed Content Pages	8
Type of use	Dissertation/Thesis
Requestor type	University/Academic
Format	Print and electronic
Portion	Figure/table
Number of figures/tables	1
Will you be translating?	No
Title	Towards Clinical Microscopic Fractional Anisotropy Imaging
Institution name	University of Western Ontario
Expected presentation date	Aug 2023
Portions	Figure 1

References

- [1] D. Le Bihan, C. Poupon, A. Amadon, and F. Lethimonnier, “Artifacts and pitfalls in diffusion MRI,” *J. Magn. Reson. Imaging*, vol. 24, no. 3, pp. 478–488, Sep. 2006.
- [2] N. Sim and D. Parker, “Critical design issues in the targeted molecular imaging of cell surface receptors,” *Chem. Soc. Rev.*, vol. 44, no. 8, pp. 2122–2134, Apr. 2015.
- [3] S. G. Waxman, *Clinical Neuroanatomy*, 28th ed. New York, NY: McGraw-Hill, 2016.
- [4] J. H. Martin, *Neuroanatomy Text and Atlas*, 4th ed. Maidenhead, England: McGraw Hill Higher Education, 2012.
- [5] E. Kandel and J. Schwartz, *Principles of Neural Science*, 5th ed. New York, NY: McGraw-Hill Professional Publishing, 2014.
- [6] R. W. Brown, Y. C Norman Cheng, E. M. Haacke, M. R. Thompson, and R. Venkatesan, *Magnetic resonance imaging: Physical properties and sequence design*. Wiley-Blackwell, 2014.
- [7] D. G. Nishimura, *Principles of magnetic resonance imaging*. Morrisville, NC: Lulu.com, 2013.
- [8] D. K. Jones, Ed., *Diffusion MRI: Theory, methods, and applications*. Cary, NC: Oxford University Press, 2010.
- [9] C. S. von Bartheld, J. Bahney, and S. Herculano-Houzel, “The search for true numbers of neurons and glial cells in the human brain: A review of 150 years of cell counting,” *J. Comp. Neurol.*, vol. 524, no. 18, pp. 3865–3895, Dec. 2016.
- [10] C. S. von Bartheld, “Myths and truths about the cellular composition of the human brain: A review of influential concepts,” *J. Chem. Neuroanat.*, vol. 93, pp. 2–15, Nov. 2018.
- [11] W. J. Streit, “Microglial senescence: does the brain’s immune system have an expiration date?,” *Trends Neurosci.*, vol. 29, no. 9, pp. 506–510, Sep. 2006.
- [12] R. E. Mrazek and W. S. T. Griffin, “Glia and their cytokines in progression of neurodegeneration,” *Neurobiol. Aging*, vol. 26, no. 3, pp. 349–354, Mar. 2005.
- [13] D. Purves, *Neuroscience*, 2nd ed. Sunderland, MA: Sinauer Associates, 2001.
- [14] B. L. C. Wright, J. T. F. Lai, and A. J. Sinclair, “Cerebrospinal fluid and lumbar puncture: a practical review,” *J. Neurol.*, vol. 259, no. 8, pp. 1530–1545, Aug. 2012.
- [15] E. V. Sullivan and A. Pfefferbaum, “Diffusion tensor imaging and aging,” *Neurosci. Biobehav. Rev.*, vol. 30, no. 6, pp. 749–761, Aug. 2006.
- [16] T. L. Jernigan *et al.*, “Effects of age on tissues and regions of the cerebrum and cerebellum,” *Neurobiol. Aging*, vol. 22, no. 4, pp. 581–594, Jul. 2001.
- [17] N. Raz *et al.*, “Selective aging of the human cerebral cortex observed in vivo: differential vulnerability of the prefrontal gray matter,” *Cereb. Cortex*, vol. 7, no. 3, pp. 268–282, Apr. 1997.
- [18] R. Raghupathi, “Cell death mechanisms following traumatic brain injury,” *Brain Pathol.*, vol. 14, no. 2, pp. 215–222, Apr. 2004.
- [19] P. Lipton, “Ischemic cell death in brain neurons,” *Physiol. Rev.*, vol. 79, no. 4, pp. 1431–1568, Jan. 1999.
- [20] L. Conforti, R. Adalbert, and M. P. Coleman, “Neuronal death: where does the end begin?,” *Trends Neurosci.*, vol. 30, no. 4, pp. 159–166, Apr. 2007.

- [21] E. Mioshi *et al.*, “Cortical atrophy in ALS is critically associated with neuropsychiatric and cognitive changes,” *Neurology*, vol. 80, no. 12, pp. 1117–1123, Mar. 2013.
- [22] L. Pini *et al.*, “Brain atrophy in Alzheimer’s Disease and aging,” *Ageing Res. Rev.*, vol. 30, pp. 25–48, Sep. 2016.
- [23] R. Dobson and G. Giovannoni, “Multiple sclerosis - a review,” *Eur. J. Neurol.*, vol. 26, no. 1, pp. 27–40, Jan. 2019.
- [24] M. de Curtis, R. Garbelli, and L. Uva, “A hypothesis for the role of axon demyelination in seizure generation,” *Epilepsia*, vol. 62, no. 3, pp. 583–595, Mar. 2021.
- [25] S. Ochs, R. Pourmand, R. A. Jersild Jr, and R. N. Friedman, “The origin and nature of beading: a reversible transformation of the shape of nerve fibers,” *Prog. Neurobiol.*, vol. 52, no. 5, pp. 391–426, Aug. 1997.
- [26] M. D. Budde and J. A. Frank, “Neurite beading is sufficient to decrease the apparent diffusion coefficient after ischemic stroke,” *Proc. Natl. Acad. Sci. U. S. A.*, vol. 107, no. 32, pp. 14472–14477, Aug. 2010.
- [27] S. Al-Noori and J. W. Swann, “A role for sodium and chloride in kainic acid-induced beading of inhibitory interneuron dendrites,” *Neuroscience*, vol. 101, no. 2, pp. 337–348, 2000.
- [28] R. L. Rungta *et al.*, “The cellular mechanisms of neuronal swelling underlying cytotoxic edema,” *Cell*, vol. 161, no. 3, pp. 610–621, Apr. 2015.
- [29] J. A. Hellas and R. D. Andrew, “Neuronal swelling: A non-osmotic consequence of spreading depolarization,” *Neurocrit. Care*, vol. 35, no. Suppl 2, pp. 112–134, Oct. 2021.
- [30] P. A. Pullarkat, P. Dommersnes, P. Fernández, J.-F. Joanny, and A. Ott, “Osmotically driven shape transformations in axons,” *Phys. Rev. Lett.*, vol. 96, no. 4, p. 048104, Feb. 2006.
- [31] M. V. Sofroniew, “Molecular dissection of reactive astrogliosis and glial scar formation,” *Trends Neurosci.*, vol. 32, no. 12, pp. 638–647, Dec. 2009.
- [32] M. Rivera-Zengotita and A. T. Yachnis, “Gliosis versus glioma?,” *Adv. Anat. Pathol.*, vol. 19, no. 4, pp. 239–249, Jul. 2012.
- [33] K. M. Fiest *et al.*, “Prevalence and incidence of epilepsy,” *Neurology*, vol. 88, no. 3, pp. 296–303, Jan. 2017.
- [34] J. Engel Jr, “Report of the ILAE classification core group,” *Epilepsia*, vol. 47, no. 9, pp. 1558–1568, Sep. 2006.
- [35] R. Ottman *et al.*, “Comorbidities of epilepsy: results from the Epilepsy Comorbidities and Health (EPIC) survey,” *Epilepsia*, vol. 52, no. 2, pp. 308–315, Feb. 2011.
- [36] P. Kwan and M. J. Brodie, “Early identification of refractory epilepsy,” *N. Engl. J. Med.*, vol. 342, no. 5, pp. 314–319, Feb. 2000.
- [37] I. Georgiadis, E. Z. Kapsalaki, and K. N. Fountas, “Temporal lobe resective surgery for medically intractable epilepsy: a review of complications and side effects,” *Epilepsy Res. Treat.*, vol. 2013, p. 752195, Oct. 2013.
- [38] J. Engel Jr, “Surgery for seizures,” *N. Engl. J. Med.*, vol. 334, no. 10, pp. 647–652, Mar. 1996.
- [39] H. M. Duvernoy, F. Cattin, and P.-Y. Risold, *The human hippocampus*, 4th ed. Berlin, Germany: Springer, 2013.

- [40] E. Tramonì-Negre, I. Lambert, F. Bartolomei, and O. Felician, "Long-term memory deficits in temporal lobe epilepsy," *Rev. Neurol. (Paris)*, vol. 173, no. 7–8, pp. 490–497, Jul. 2017.
- [41] R. Turner and D. Le Bihan, "Single-shot diffusion imaging at 2.0 tesla," *J. Magn. Reson.*, vol. 86, no. 3, pp. 445–452, Feb. 1990.
- [42] R. Brown, "XXVII. A brief account of microscopical observations made in the months of June, July and August 1827, on the particles contained in the pollen of plants; and on the general existence of active molecules in organic and inorganic bodies," *Philos. Mag.*, vol. 4, no. 21, pp. 161–173, Sep. 1828.
- [43] A. Einstein, *Investigations on the theory of the Brownian movement*. Mineola, NY: Dover Publications, 1956.
- [44] H. C. Torrey, "Bloch equations with diffusion terms," *Phys. Rev.*, vol. 104, no. 3, pp. 563–565, Nov. 1956.
- [45] V. M. Kenkre, E. Fukushima, and D. Sheltraw, "Simple solutions of the Torrey–Bloch equations in the NMR study of molecular diffusion," *J. Magn. Reson.*, vol. 128, no. 1, pp. 62–69, Sep. 1997.
- [46] E. O. Stejskal and J. E. Tanner, "Spin Diffusion Measurements: Spin Echoes in the Presence of a Time-Dependent Field Gradient," *J. Chem. Phys.*, vol. 42, no. 1, pp. 288–292, Jan. 1965.
- [47] P. J. Basser, J. Mattiello, and D. LeBihan, "Estimation of the effective self-diffusion tensor from the NMR spin echo," *J. Magn. Reson. B*, vol. 103, no. 3, pp. 247–254, Mar. 1994.
- [48] L. J. O'Donnell and C.-F. Westin, "An introduction to diffusion tensor image analysis," *Neurosurg. Clin. N. Am.*, vol. 22, no. 2, pp. 185–96, viii, Apr. 2011.
- [49] P. J. Basser and C. Pierpaoli, "Microstructural and physiological features of tissues elucidated by quantitative-diffusion-tensor MRI," *Journal of Magnetic Resonance - Series B*, vol. 111, no. 3, pp. 209–219, Dec. 1996.
- [50] J. Neil, J. Miller, P. Mukherjee, and P. S. Hüppi, "Diffusion tensor imaging of normal and injured developing human brain - a technical review," *NMR Biomed.*, vol. 15, no. 7–8, pp. 543–552, Nov. 2002.
- [51] P. J. Basser, S. Pajevic, C. Pierpaoli, J. Duda, and A. Aldroubi, "In vivo fiber tractography using DT-MRI data," *Magn. Reson. Med.*, vol. 44, no. 4, pp. 625–632, Oct. 2000.
- [52] J. B. Fiebach, O. Jansen, P. D. Schellinger, S. Heiland, W. Hacke, and K. Sartor, "Serial analysis of the apparent diffusion coefficient time course in human stroke," *Neuroradiology*, vol. 44, no. 4, pp. 294–298, Apr. 2002.
- [53] G. Schlaug, B. Siewert, A. Benfield, R. R. Edelman, and S. Warach, "Time course of the apparent diffusion coefficient (ADC) abnormality in human stroke," *Neurology*, vol. 49, no. 1, pp. 113–119, Jul. 1997.
- [54] T. Yoshiura *et al.*, "Cerebral white matter degeneration in frontotemporal dementia detected by diffusion-weighted magnetic resonance imaging," *Acad. Radiol.*, vol. 13, no. 11, pp. 1373–1378, Nov. 2006.
- [55] R. Hanks *et al.*, "The relation between cognitive dysfunction and diffusion tensor imaging parameters in traumatic brain injury," *Brain Inj.*, vol. 33, no. 3, pp. 355–363, 2019.

- [56] M. Inglese and M. Bester, "Diffusion imaging in multiple sclerosis: Research and clinical implications," *NMR in Biomedicine*, vol. 23, no. 7, pp. 865–872, 2010.
- [57] L. T. Westlye *et al.*, "Life-span changes of the human brain white matter: diffusion tensor imaging (DTI) and volumetry," *Cereb. Cortex*, vol. 20, no. 9, pp. 2055–2068, Sep. 2010.
- [58] J. L. Villegas Martínez, J. A. Blanco Garrote, F. Uribe Ladrón de Cegama, B. Arribas Simón, and G. Cabús Piñol, "Diffusion tensor imaging (DTI) findings in schizophrenia: A review," *Eur. Psychiatry*, vol. 26, no. S2, pp. 960–960, Mar. 2011.
- [59] C. Beaulieu and P. S. Allen, "Water diffusion in the giant axon of the squid: implications for diffusion-weighted MRI of the nervous system," *Magn. Reson. Med.*, vol. 32, no. 5, pp. 579–583, Nov. 1994.
- [60] H. Johansen-Berg and T. E. J. Behrens, Eds., *Diffusion MRI: From quantitative measurement to in vivo neuroanatomy*, 2nd ed. Academic Press, 2013.
- [61] N. Shemesh, T. Adiri, and Y. Cohen, "Probing microscopic architecture of opaque heterogeneous systems using double-pulsed-field-gradient NMR," *J. Am. Chem. Soc.*, vol. 133, no. 15, pp. 6028–6035, Apr. 2011.
- [62] J. H. Jensen, J. A. Helpert, A. Ramani, H. Lu, and K. Kaczynski, "Diffusional kurtosis imaging: the quantification of non-gaussian water diffusion by means of magnetic resonance imaging," *Magnetic Resonance in Medicine: An Official Journal of the International Society for Magnetic Resonance in Medicine*, vol. 53, no. 6, pp. 1432–1440, 2005.
- [63] C. R. Figley, M. N. Uddin, K. Wong, J. Kornelsen, J. Puig, and T. D. Figley, "Potential Pitfalls of Using Fractional Anisotropy, Axial Diffusivity, and Radial Diffusivity as Biomarkers of Cerebral White Matter Microstructure," *Front. Neurosci.*, vol. 15, p. 799576, 2021.
- [64] C. Pierpaoli *et al.*, "Water diffusion changes in Wallerian degeneration and their dependence on white matter architecture," *Neuroimage*, vol. 13, no. 6 Pt 1, pp. 1174–1185, Jun. 2001.
- [65] C. Pierpaoli and P. J. Basser, "Toward a quantitative assessment of diffusion anisotropy," *Magn. Reson. Med.*, vol. 36, no. 6, pp. 893–906, Dec. 1996.
- [66] H. Lu, J. H. Jensen, A. Ramani, and J. A. Helpert, "Three-dimensional characterization of non-gaussian water diffusion in humans using diffusion kurtosis imaging," *NMR Biomed.*, vol. 19, no. 2, pp. 236–247, Apr. 2006.
- [67] J.-J. Wang *et al.*, "Parkinson disease: diagnostic utility of diffusion kurtosis imaging," *Radiology*, vol. 261, no. 1, pp. 210–217, Oct. 2011.
- [68] H. Struyfs *et al.*, "Diffusion kurtosis imaging: A possible MRI biomarker for AD diagnosis?," *J. Alzheimers. Dis.*, vol. 48, no. 4, pp. 937–948, 2015.
- [69] L. Bonilha *et al.*, "Altered microstructure in temporal lobe epilepsy: a diffusional kurtosis imaging study," *AJNR Am. J. Neuroradiol.*, vol. 36, no. 4, pp. 719–724, Apr. 2015.
- [70] L. W. Kasa, T. Peters, S. M. Mirsattari, M. T. Jurkiewicz, A. R. Khan, and R. A M Haast, "The role of the temporal pole in temporal lobe epilepsy: A diffusion kurtosis imaging study," *NeuroImage Clin.*, vol. 36, no. 103201, p. 103201, Sep. 2022.
- [71] S. N. Jespersen, H. Lundell, C. K. Sønderby, and T. B. Dyrby, "Orientationally invariant metrics of apparent compartment eccentricity from double pulsed field

- gradient diffusion experiments,” *NMR Biomed.*, vol. 26, no. 12, pp. 1647–1662, Dec. 2013.
- [72] S. Lasič, F. Szczepankiewicz, S. Eriksson, M. Nilsson, and D. Topgaard, “Microanisotropy imaging: quantification of microscopic diffusion anisotropy and orientational order parameter by diffusion MRI with magic-angle spinning of the q-vector,” *Frontiers in Physics*, vol. 2, 2014.
- [73] Y. Ikenouchi *et al.*, “Evaluation of white matter microstructure in patients with Parkinson’s disease using microscopic fractional anisotropy,” *Neuroradiology*, vol. 62, no. 2, pp. 197–203, Feb. 2020.
- [74] G. Yang, Q. Tian, C. Leuze, M. Wintermark, and J. A. McNab, “Double diffusion encoding MRI for the clinic,” *Magn. Reson. Med.*, vol. 80, no. 2, pp. 507–520, Aug. 2018.
- [75] F. Szczepankiewicz *et al.*, “Quantification of microscopic diffusion anisotropy disentangles effects of orientation dispersion from microstructure: Applications in healthy volunteers and in brain tumors,” *Neuroimage*, vol. 104, pp. 241–252, Jan. 2015.
- [76] S. Eriksson, S. Lasic, and D. Topgaard, “Isotropic diffusion weighting in PGSE NMR by magic-angle spinning of the q-vector,” *J. Magn. Reson.*, vol. 226, pp. 13–18, 2013.
- [77] O. Pasternak, N. Sochen, Y. Gur, N. Intrator, and Y. Assaf, “Free water elimination and mapping from diffusion MRI,” *Magn. Reson. Med.*, vol. 62, no. 3, pp. 717–730, Sep. 2009.
- [78] P. J. Planetta *et al.*, “Free-water imaging in Parkinson’s disease and atypical parkinsonism,” *Brain*, vol. 139, no. Pt 2, pp. 495–508, Feb. 2016.
- [79] A. R. Hoy *et al.*, “Microstructural white matter alterations in preclinical Alzheimer’s disease detected using free water elimination diffusion tensor imaging,” *PLoS One*, vol. 12, no. 3, p. e0173982, Mar. 2017.
- [80] O. Pasternak *et al.*, “Hockey Concussion Education Project, Part 2. Microstructural white matter alterations in acutely concussed ice hockey players: a longitudinal free-water MRI study,” *J. Neurosurg.*, vol. 120, no. 4, pp. 873–881, Apr. 2014.
- [81] N. J. J. Arezza, D. H. Y. Tse, and C. A. Baron, “Rapid microscopic fractional anisotropy imaging via an optimized linear regression formulation,” *Magn. Reson. Imaging*, vol. 80, pp. 132–143, May 2021.
- [82] J. E. Tanner, “Pulsed Field Gradients for NMR Spin-Echo Diffusion Measurements,” *Rev. Sci. Instrum.*, vol. 36, no. 8, pp. 1086–1087, Aug. 1965.
- [83] M. Rovaris *et al.*, “Diffusion MRI in multiple sclerosis,” *Neurology*, vol. 65, no. 10, pp. 1526–1532, Nov. 2005.
- [84] Y. Zhang *et al.*, “White matter damage in frontotemporal dementia and Alzheimer’s disease measured by diffusion MRI,” *Brain*, vol. 132, no. Pt 9, pp. 2579–2592, Sep. 2009.
- [85] K. J. van Everdingen, J. van der Grond, L. J. Kappelle, L. M. Ramos, and W. P. Mali, “Diffusion-weighted magnetic resonance imaging in acute stroke,” *Stroke*, vol. 29, no. 9, pp. 1783–1790, Sep. 1998.
- [86] P. J. Basser, J. Mattiello, and D. LeBihan, “MR diffusion tensor spectroscopy and imaging,” *Biophys. J.*, vol. 66, no. 1, pp. 259–267, 1994.

- [87] P. J. Basser, “Inferring microstructural features and the physiological state of tissues from diffusion-weighted images,” *NMR Biomed.*, vol. 8, no. 7–8, pp. 333–344, Nov. 1995.
- [88] B. J. Frisken, “Revisiting the method of cumulants for the analysis of dynamic light-scattering data,” *Appl. Opt.*, vol. 40, no. 24, pp. 4087–4091, Aug. 2001.
- [89] H. Lundell *et al.*, “Multidimensional diffusion MRI with spectrally modulated gradients reveals unprecedented microstructural detail,” *Sci. Rep.*, vol. 9, no. 1, p. 9026, Jun. 2019.
- [90] T. M. de Swiet and P. P. Mitra, “Possible Systematic Errors in Single-Shot Measurements of the Trace of the Diffusion Tensor,” *J. Magn. Reson. B*, vol. 111, no. 1, pp. 15–22, Apr. 1996.
- [91] M. F. Falangola *et al.*, “Age-related non-Gaussian diffusion patterns in the prefrontal brain,” *Journal of Magnetic Resonance Imaging*, vol. 28, no. 6, pp. 1345–1350, 2008.
- [92] E. Fieremans *et al.*, “Novel White Matter Tract Integrity Metrics Sensitive to Alzheimer Disease Progression,” *American Journal of Neuroradiology*, vol. 34, no. 11, pp. 2105–2112, 2013.
- [93] S. N. Jespersen, J. L. Olesen, A. Ianuş, and N. Shemesh, “Effects of nongaussian diffusion on ‘isotropic diffusion’ measurements: An ex-vivo microimaging and simulation study,” *J. Magn. Reson.*, vol. 300, pp. 84–94, Mar. 2019.
- [94] R. N. Henriques, S. N. Jespersen, and N. Shemesh, “Correlation tensor magnetic resonance imaging,” *Neuroimage*, vol. 211, p. 116605, May 2020.
- [95] L. M. Burcaw, E. Fieremans, and D. S. Novikov, “Mesoscopic structure of neuronal tracts from time-dependent diffusion,” *Neuroimage*, vol. 114, pp. 18–37, Jul. 2015.
- [96] D. K. Jones, T. R. Knösche, and R. Turner, “White matter integrity, fiber count, and other fallacies: the do’s and don’ts of diffusion MRI,” *Neuroimage*, vol. 73, pp. 239–254, Jun. 2013.
- [97] E. Fieremans, J. H. Jensen, and J. A. Helpert, “White matter characterization with diffusional kurtosis imaging,” *Neuroimage*, vol. 58, no. 1, pp. 177–188, Sep. 2011.
- [98] N. Shemesh *et al.*, “Conventions and nomenclature for double diffusion encoding NMR and MRI,” *Magn. Reson. Med.*, vol. 75, no. 1, pp. 82–87, Jan. 2016.
- [99] D. S. Novikov, E. Fieremans, S. N. Jespersen, and V. G. Kiselev, “Quantifying brain microstructure with diffusion MRI: Theory and parameter estimation,” *NMR Biomed.*, vol. 32, no. 4, p. e3998, Apr. 2019.
- [100] E. Kaden, F. Kruggel, and D. C. Alexander, “Quantitative mapping of the per-axon diffusion coefficients in brain white matter,” *Magn. Reson. Med.*, vol. 75, no. 4, pp. 1752–1763, Apr. 2016.
- [101] E. Kaden, N. D. Kelm, R. P. Carson, M. D. Does, and D. C. Alexander, “Multi-compartment microscopic diffusion imaging,” *Neuroimage*, vol. 139, pp. 346–359, Oct. 2016.
- [102] D. G. Cory, A. N. Garroway, and J. B. Miller, “Applications of spin transport as a probe of local geometry,” in *Abstracts of Papers of the American Chemical Society*, 1990, vol. 199, pp. 105-POLY.
- [103] S. Eriksson, S. Lasič, M. Nilsson, C.-F. Westin, and D. Topgaard, “NMR diffusion-encoding with axial symmetry and variable anisotropy: Distinguishing between prolate and oblate microscopic diffusion tensors with unknown orientation distribution,” *The Journal of Chemical Physics*, vol. 142, no. 10, p. 104201, 2015.

- [104] C.-F. Westin *et al.*, “Q-space trajectory imaging for multidimensional diffusion MRI of the human brain,” *Neuroimage*, vol. 135, pp. 345–362, Jul. 2016.
- [105] B. Lampinen, F. Szczepankiewicz, J. Mårtensson, D. van Westen, P. C. Sundgren, and M. Nilsson, “Neurite density imaging versus imaging of microscopic anisotropy in diffusion MRI: A model comparison using spherical tensor encoding,” *Neuroimage*, vol. 147, pp. 517–531, Feb. 2017.
- [106] R. N. Henriques, S. N. Jespersen, and N. Shemesh, “Microscopic anisotropy misestimation in spherical-mean single diffusion encoding MRI,” *Magn. Reson. Med.*, Jan. 2019.
- [107] P. P. Mitra, “Multiple wave-vector extensions of the NMR pulsed-field-gradient spin-echo diffusion measurement,” *Phys. Rev. B Condens. Matter*, vol. 51, no. 21, pp. 15074–15078, Jun. 1995.
- [108] A. Ianuş, S. N. Jespersen, T. Serradas Duarte, D. C. Alexander, I. Drobnjak, and N. Shemesh, “Accurate estimation of microscopic diffusion anisotropy and its time dependence in the mouse brain,” *Neuroimage*, vol. 183, pp. 934–949, 2018.
- [109] E. Ozarslan and P. J. Basser, “Microscopic anisotropy revealed by NMR double pulsed field gradient experiments with arbitrary timing parameters,” *J. Chem. Phys.*, vol. 128, no. 15, p. 154511, Apr. 2008.
- [110] M. Lawrenz and J. Finsterbusch, “Mapping measures of microscopic diffusion anisotropy in human brain white matter in vivo with double-wave-vector diffusion-weighted imaging,” *Magn. Reson. Med.*, vol. 73, no. 2, pp. 773–783, Feb. 2015.
- [111] L. Kerkelä, R. N. Henriques, M. G. Hall, C. A. Clark, and N. Shemesh, “Validation and noise robustness assessment of microscopic anisotropy estimation with clinically feasible double diffusion encoding MRI,” *Magn. Reson. Med.*, vol. 83, no. 5, pp. 1698–1710, May 2020.
- [112] C. A. Baron, R. M. Lebel, A. H. Wilman, and C. Beaulieu, “The effect of concomitant gradient fields on diffusion tensor imaging,” *Magn. Reson. Med.*, vol. 68, no. 4, pp. 1190–1201, Oct. 2012.
- [113] F. Szczepankiewicz, C. Westin, and M. Nilsson, “Maxwell-compensated design of asymmetric gradient waveforms for tensor-valued diffusion encoding,” *Magn. Reson. Med.*, vol. 82, no. 4, p. mrm.27828, May 2019.
- [114] F. Szczepankiewicz *et al.*, “The link between diffusion MRI and tumor heterogeneity: Mapping cell eccentricity and density by diffusional variance decomposition (DIVIDE),” *Neuroimage*, vol. 142, pp. 522–532, Nov. 2016.
- [115] C.-F. Westin *et al.*, “Measurement tensors in diffusion MRI: generalizing the concept of diffusion encoding,” *Med. Image Comput. Comput. Assist. Interv.*, vol. 17, no. Pt 3, pp. 209–216, 2014.
- [116] F. Nery *et al.*, “In vivo demonstration of microscopic anisotropy in the human kidney using multidimensional diffusion MRI,” *Magn. Reson. Med.*, vol. 82, no. 6, pp. 2160–2168, Dec. 2019.
- [117] M. Nilsson *et al.*, “Tensor-valued diffusion MRI in under 3 minutes: an initial survey of microscopic anisotropy and tissue heterogeneity in intracranial tumors,” *Magn. Reson. Med.*, Sep. 2019.
- [118] N. Shemesh, “Axon Diameters and Myelin Content Modulate Microscopic Fractional Anisotropy at Short Diffusion Times in Fixed Rat Spinal Cord,” *Frontiers in Physics*, vol. 6, 2018.

- [119] D. Xing, N. G. Papadakis, C. L. H. Huang, V. M. Lee, T. A. Carpenter, and L. D. Hall, "Optimised diffusion-weighting for measurement of apparent diffusion coefficient (ADC) in human brain," *Magn. Reson. Imaging*, vol. 15, no. 7, pp. 771–784, 1997.
- [120] P. R. Bevington, D. K. Robinson, J. M. Blair, A. J. Mallinckrodt, and S. McKay, "Data Reduction and Error Analysis for the Physical Sciences," *Computers in Physics*, vol. 7, no. 4, pp. 415–416, Jul. 1993.
- [121] J. L. R. Andersson and S. N. Sotiropoulos, "An integrated approach to correction for off-resonance effects and subject movement in diffusion MR imaging," *Neuroimage*, vol. 125, pp. 1063–1078, Jan. 2016.
- [122] J. P. Wansapura, S. K. Holland, R. S. Dunn, and W. S. Ball, "NMR relaxation times in the human brain at 3.0 Tesla," *J. Magn. Reson. Imaging*, vol. 9, no. 4, pp. 531–538, Apr. 1999.
- [123] C. Baron and N. J. J. Arezza, "Test-Retest Data Repository for Spherical Tensor Encoding," 14-Oct-2020. [Online]. Available: <https://osf.io/etkgx/>.
- [124] J. Veraart, D. S. Novikov, D. Christiaens, B. Ades-Aron, J. Sijbers, and E. Fieremans, "Denoising of diffusion MRI using random matrix theory," *Neuroimage*, vol. 142, pp. 394–406, Nov. 2016.
- [125] Y. Zhang, M. Brady, and S. Smith, "Segmentation of brain MR images through a hidden Markov random field model and the expectation-maximization algorithm," *IEEE Trans. Med. Imaging*, vol. 20, no. 1, pp. 45–57, Jan. 2001.
- [126] D. Q. Chen, F. Dell'Acqua, A. Rokem, and E. Garyfallidis, "Diffusion Weighted Image Co-registration: Investigation of Best Practices," *BioRxiv*, 2019.
- [127] D. K. Jones, M. A. Horsfield, and A. Simmons, "Optimal strategies for measuring diffusion in anisotropic systems by magnetic resonance imaging," *Magn. Reson. Med.*, vol. 42, no. 3, pp. 515–525, Sep. 1999.
- [128] M. Nilsson *et al.*, "An open-source framework for analysis of multidimensional diffusion MRI data implemented in MATLAB," in *Proc. Intl. Soc. Mag. Reson. Med.*, Paris, France, 2018.
- [129] F. Szczepankiewicz, J. Sjölund, F. Ståhlberg, J. Lätt, and M. Nilsson, "Tensor-valued diffusion encoding for diffusional variance decomposition (DIVIDE): Technical feasibility in clinical MRI systems," *PLoS One*, vol. 14, no. 3, p. e0214238, Mar. 2019.
- [130] F. Szczepankiewicz, C.-F. Westin, and M. Nilsson, "Gradient waveform design for tensor-valued encoding in diffusion MRI," *J. Neurosci. Methods*, vol. 348, p. 109007, Jan. 2021.
- [131] N. J. J. Arezza, T. Santini, M. Omer, and C. A. Baron, "Estimation of free water-corrected microscopic fractional anisotropy," *Front. Neurosci.*, vol. 17, 2023.
- [132] H. Johansen-Berg and T. E. J. Behrens, *Diffusion MRI: From Quantitative Measurement to In-vivo Neuroanatomy*, vol. 1. Elsevier/Academic Press, 2009.
- [133] J. H. Jensen and J. A. Helpert, "MRI quantification of non-Gaussian water diffusion by kurtosis analysis," *NMR Biomed.*, vol. 23, no. 7, pp. 698–710, Aug. 2010.
- [134] R. N. Henriques, S. N. Jespersen, D. K. Jones, and J. Veraart, "Toward more robust and reproducible diffusion kurtosis imaging," *Magn. Reson. Med.*, vol. 86, no. 3, pp. 1600–1613, Sep. 2021.

- [135] D. K. Jones and M. Cercignani, “Twenty-five pitfalls in the analysis of diffusion MRI data,” *NMR Biomed.*, vol. 23, no. 7, pp. 803–820, Aug. 2010.
- [136] S. B. Vos, D. K. Jones, M. A. Viergever, and A. Leemans, “Partial volume effect as a hidden covariate in DTI analyses,” *Neuroimage*, vol. 55, no. 4, pp. 1566–1576, Apr. 2011.
- [137] A. L. Alexander, K. M. Hasan, M. Lazar, J. S. Tsuruda, and D. L. Parker, “Analysis of partial volume effects in diffusion-tensor MRI,” *Magn. Reson. Med.*, vol. 45, no. 5, pp. 770–780, May 2001.
- [138] C. A. Baron and C. Beaulieu, “Acquisition strategy to reduce cerebrospinal fluid partial volume effects for improved DTI tractography,” *Magn. Reson. Med.*, vol. 73, no. 3, pp. 1075–1084, Mar. 2015.
- [139] K. W. Andersen *et al.*, “Disentangling white-matter damage from physiological fibre orientation dispersion in multiple sclerosis,” *Brain Commun*, vol. 2, no. 2, p. fcaa077, Jun. 2020.
- [140] S. Li *et al.*, “Increased global and local efficiency of human brain anatomical networks detected with FLAIR-DTI compared to non-FLAIR-DTI,” *PLoS One*, vol. 8, no. 8, p. e71229, Aug. 2013.
- [141] C. Metzler-Baddeley, M. J. O’Sullivan, S. Bells, O. Pasternak, and D. K. Jones, “How and how not to correct for CSF-contamination in diffusion MRI,” *Neuroimage*, vol. 59, no. 2, pp. 1394–1403, Jan. 2012.
- [142] N. G. Papadakis *et al.*, “Study of the effect of CSF suppression on white matter diffusion anisotropy mapping of healthy human brain,” *Magn. Reson. Med.*, vol. 48, no. 2, pp. 394–398, Aug. 2002.
- [143] M.-C. Chou *et al.*, “FLAIR diffusion-tensor MR tractography: comparison of fiber tracking with conventional imaging,” *AJNR Am. J. Neuroradiol.*, vol. 26, no. 3, pp. 591–597, Mar. 2005.
- [144] O. Pasternak, K. Maier-Hein, C. Baumgartner, M. E. Shenton, Y. Rathi, and C.-F. Westin, “The Estimation of Free-Water Corrected Diffusion Tensors,” in *Visualization and Processing of Tensors and Higher Order Descriptors for Multi-Valued Data*, 2014, pp. 249–270.
- [145] M. Golub, R. Neto Henriques, and R. Gouveia Nunes, “Free-water DTI estimates from single b-value data might seem plausible but must be interpreted with care,” *Magn. Reson. Med.*, Dec. 2020.
- [146] Q. Collier *et al.*, “Diffusion kurtosis imaging with free water elimination: A bayesian estimation approach,” *Magn. Reson. Med.*, vol. 80, no. 2, pp. 802–813, Aug. 2018.
- [147] J. Yoo, L. Kerkelä, P. W. Hales, K. K. Seunarine, and C. A. Clark, “High-resolution microscopic diffusion anisotropy imaging in the human hippocampus at 3T,” *Magn. Reson. Med.*, Nov. 2021.
- [148] M. Lawrenz, S. Brassens, and J. Finsterbusch, “Microscopic diffusion anisotropy in the human brain: Age-related changes,” *Neuroimage*, vol. 141, pp. 313–325, Nov. 2016.
- [149] P. A. Cook *et al.*, “Camino: Open-Source Diffusion-MRI Reconstruction and Processing,” *Proc. Intl. Soc. Mag. Reson. Med.*, vol. 14, p. 2759, 2006.
- [150] B. Dhital, M. Reisert, E. Kellner, and V. G. Kiselev, “Intra-axonal diffusivity in brain white matter,” *Neuroimage*, vol. 189, pp. 543–550, Apr. 2019.

- [151] E. Kellner, B. Dhital, V. G. Kiselev, and M. Reiser, “Gibbs-ringing artifact removal based on local subvoxel-shifts,” *Magn. Reson. Med.*, vol. 76, no. 5, pp. 1574–1581, Nov. 2016.
- [152] J.-D. Tournier *et al.*, “MRtrix3: A fast, flexible and open software framework for medical image processing and visualisation,” *Neuroimage*, vol. 202, p. 116137, Nov. 2019.
- [153] B. Patenaude, S. M. Smith, D. N. Kennedy, and M. Jenkinson, “A Bayesian model of shape and appearance for subcortical brain segmentation,” *Neuroimage*, vol. 56, no. 3, pp. 907–922, Jun. 2011.
- [154] J. Veraart, D. S. Novikov, and E. Fieremans, “TE dependent Diffusion Imaging (TEdDI) distinguishes between compartmental T2 relaxation times,” *Neuroimage*, vol. 182, pp. 360–369, Nov. 2018.
- [155] B. Bender and U. Klose, “Cerebrospinal fluid and interstitial fluid volume measurements in the human brain at 3T with EPI,” *Magn. Reson. Med.*, vol. 61, no. 4, pp. 834–841, Apr. 2009.
- [156] T. Ernst, R. Kreis, and B. D. Ross, “Absolute Quantitation of Water and Metabolites in the Human Brain. I. Compartments and Water,” *J. Magn. Reson. B*, vol. 102, no. 1, pp. 1–8, Aug. 1993.
- [157] S. K. Piechnik, J. Evans, L. H. Bary, R. G. Wise, and P. Jezzard, “Functional changes in CSF volume estimated using measurement of water T2 relaxation,” *Magn. Reson. Med.*, vol. 61, no. 3, pp. 579–586, Mar. 2009.
- [158] G. J. Stanisz *et al.*, “T1, T2 relaxation and magnetization transfer in tissue at 3T,” *Magn. Reson. Med.*, vol. 54, no. 3, pp. 507–512, Sep. 2005.
- [159] P. A. Bartlett, M. R. Symms, S. L. Free, and J. S. Duncan, “T2 relaxometry of the hippocampus at 3T,” *AJNR Am. J. Neuroradiol.*, vol. 28, no. 6, pp. 1095–1098, Jun. 2007.
- [160] J. A. Chad, O. Pasternak, D. H. Salat, and J. J. Chen, “Re-examining age-related differences in white matter microstructure with free-water corrected diffusion tensor imaging,” *Neurobiol. Aging*, vol. 71, pp. 161–170, Nov. 2018.
- [161] L. Novello, R. N. Henriques, A. Ianuş, T. Feiweier, N. Shemesh, and J. Jovicich, “In vivo Correlation Tensor MRI reveals microscopic kurtosis in the human brain on a clinical 3T scanner,” *Neuroimage*, vol. 254, p. 119137, Jul. 2022.
- [162] H. Gudbjartsson and S. Patz, “The Rician distribution of noisy MRI data,” *Magn. Reson. Med.*, vol. 34, no. 6, pp. 910–914, Dec. 1995.
- [163] S. Aja-Fernandez and G. Vegas-Sanchez-Ferrero, *Statistical analysis of noise in MRI*. Cham, Switzerland: Springer International Publishing, 2018.
- [164] M. Afzali, H. Knutsson, E. Özarslan, and D. K. Jones, “Computing the orientational-average of diffusion-weighted MRI signals: a comparison of different techniques,” *Sci. Rep.*, vol. 11, no. 1, p. 14345, Jul. 2021.
- [165] N. J. J. Arezza *et al.*, “Microscopic fractional anisotropy asymmetry in unilateral temporal lobe epilepsy,” *medRxiv*, 12-May-2023.
- [166] M. L. Bell *et al.*, “Epilepsy surgery outcomes in temporal lobe epilepsy with a normal MRI,” *Epilepsia*, vol. 50, no. 9, pp. 2053–2060, Sep. 2009.
- [167] S. Wiebe, W. T. Blume, J. P. Girvin, and M. Eliasziw, “A Randomized, Controlled Trial of Surgery for Temporal-Lobe Epilepsy,” *New England Journal of Medicine*, vol. 345, no. 5, pp. 311–318, 2001.

- [168] S. Vadera, V. R. Kshetry, P. Klaas, and W. Bingaman, “Seizure-free and neuropsychological outcomes after temporal lobectomy with amygdalohippocampectomy in pediatric patients with hippocampal sclerosis,” *J. Neurosurg. Pediatr.*, vol. 10, no. 2, pp. 103–107, Aug. 2012.
- [169] S. Chabardès *et al.*, “The temporopolar cortex plays a pivotal role in temporal lobe seizures,” *Brain*, vol. 128, no. Pt 8, pp. 1818–1831, Aug. 2005.
- [170] W. Muhlhof, Y.-L. Tan, S. G. Mueller, and R. Knowlton, “MRI-negative temporal lobe epilepsy-What do we know?,” *Epilepsia*, vol. 58, no. 5, pp. 727–742, May 2017.
- [171] G. P. Winston *et al.*, “Microstructural imaging in temporal lobe epilepsy: Diffusion imaging changes relate to reduced neurite density,” *Neuroimage Clin*, vol. 26, p. 102231, Feb. 2020.
- [172] C. Scanlon, S. G. Mueller, I. Cheong, M. Hartig, M. W. Weiner, and K. D. Laxer, “Grey and white matter abnormalities in temporal lobe epilepsy with and without mesial temporal sclerosis,” *J. Neurol.*, vol. 260, no. 9, pp. 2320–2329, Sep. 2013.
- [173] S. Treit *et al.*, “Regional hippocampal diffusion abnormalities associated with subfield-specific pathology in temporal lobe epilepsy,” *Epilepsia Open*, vol. 4, no. 4, pp. 544–554, Dec. 2019.
- [174] M. Goubran *et al.*, “In vivo MRI signatures of hippocampal subfield pathology in intractable epilepsy,” *Hum. Brain Mapp.*, vol. 37, no. 3, pp. 1103–1119, Mar. 2016.
- [175] J.-D. Tournier, S. Mori, and A. Leemans, “Diffusion tensor imaging and beyond,” *Magn. Reson. Med.*, vol. 65, no. 6, pp. 1532–1556, Jun. 2011.
- [176] H. Oouchi *et al.*, “Diffusion anisotropy measurement of brain white matter is affected by voxel size: underestimation occurs in areas with crossing fibers,” *AJNR Am. J. Neuroradiol.*, vol. 28, no. 6, pp. 1102–1106, Jun. 2007.
- [177] G. D. Cascino *et al.*, “Magnetic resonance imaging-based volume studies in temporal lobe epilepsy: pathological correlations,” *Ann. Neurol.*, vol. 30, no. 1, pp. 31–36, Jul. 1991.
- [178] I. Blümcke *et al.*, “International consensus classification of hippocampal sclerosis in temporal lobe epilepsy: a Task Force report from the ILAE Commission on Diagnostic Methods,” *Epilepsia*, vol. 54, no. 7, pp. 1315–1329, Jul. 2013.
- [179] K. Sato *et al.*, “Understanding microstructure of the brain by comparison of neurite orientation dispersion and density imaging (NODDI) with transparent mouse brain,” *Acta Radiol Open*, vol. 6, no. 4, p. 2058460117703816, Apr. 2017.
- [180] J. Veraart, E. Fieremans, and D. S. Novikov, “Diffusion MRI noise mapping using random matrix theory,” *Magn. Reson. Med.*, vol. 76, no. 5, pp. 1582–1593, Nov. 2016.
- [181] J. L. R. Andersson, S. Skare, and J. Ashburner, “How to correct susceptibility distortions in spin-echo echo-planar images: application to diffusion tensor imaging,” *Neuroimage*, vol. 20, no. 2, pp. 870–888, Oct. 2003.
- [182] S. M. Smith *et al.*, “Advances in functional and structural MR image analysis and implementation as FSL,” *Neuroimage*, vol. 23 Suppl 1, pp. S208–19, 2004.
- [183] J. DeKraker *et al.*, “Automated hippocampal unfolding for morphometry and subfield segmentation with HippUnfold,” *Elife*, vol. 11, Dec. 2022.
- [184] M. Jenkinson, P. Bannister, M. Brady, and S. Smith, “Improved optimization for the robust and accurate linear registration and motion correction of brain images,” *Neuroimage*, vol. 17, no. 2, pp. 825–841, Oct. 2002.

- [185] J. Veraart, J. Sijbers, S. Sunaert, A. Leemans, and B. Jeurissen, “Weighted linear least squares estimation of diffusion MRI parameters: strengths, limitations, and pitfalls,” *Neuroimage*, vol. 81, pp. 335–346, Nov. 2013.
- [186] B. A. Assaf *et al.*, “Diffusion tensor imaging of the hippocampal formation in temporal lobe epilepsy,” *AJNR Am. J. Neuroradiol.*, vol. 24, no. 9, pp. 1857–1862, Oct. 2003.
- [187] D. Liacu, G. de Marco, D. Ducreux, V. Bouilleret, P. Masnou, and I. Idy-Peretti, “Diffusion tensor changes in epileptogenic hippocampus of TLE patients,” *Neurophysiol. Clin.*, vol. 40, no. 3, pp. 151–157, Jun. 2010.
- [188] N. K. Focke, M. Yogarajah, S. B. Bonelli, P. A. Bartlett, M. R. Symms, and J. S. Duncan, “Voxel-based diffusion tensor imaging in patients with mesial temporal lobe epilepsy and hippocampal sclerosis,” *Neuroimage*, vol. 40, no. 2, pp. 728–737, Apr. 2008.
- [189] G. Chau Loo Kung *et al.*, “High-resolution hippocampal diffusion tensor imaging of mesial temporal sclerosis in refractory epilepsy,” *Epilepsia*, vol. 63, no. 9, pp. 2301–2311, Sep. 2022.
- [190] Y. Yang, M. Coleman, L. Zhang, X. Zheng, and Z. Yue, “Autophagy in axonal and dendritic degeneration,” *Trends Neurosci.*, vol. 36, no. 7, pp. 418–428, Jul. 2013.
- [191] T. Koike, Y. Yang, K. Suzuki, and X. Zheng, “Axon & dendrite degeneration: its mechanisms and protective experimental paradigms,” *Neurochem. Int.*, vol. 52, no. 4–5, pp. 751–760, Mar. 2008.
- [192] M. P. Coleman and V. H. Perry, “Axon pathology in neurological disease: a neglected therapeutic target,” *Trends Neurosci.*, vol. 25, no. 10, pp. 532–537, Oct. 2002.
- [193] A. Uyeda and R. Muramatsu, “Molecular Mechanisms of Central Nervous System Axonal Regeneration and Remyelination: A Review,” *Int. J. Mol. Sci.*, vol. 21, no. 21, Oct. 2020.
- [194] A. A. Woolard and S. Heckers, “Anatomical and functional correlates of human hippocampal volume asymmetry,” *Psychiatry Res.*, vol. 201, no. 1, pp. 48–53, Jan. 2012.
- [195] C. J. Bruton, *The Neuropathology of Temporal Lobe Epilepsy*. Oxford University Press, 1988.
- [196] K. G. Davies, B. P. Hermann, F. C. Dohan Jr, K. T. Foley, A. J. Bush, and A. R. Wyler, “Relationship of hippocampal sclerosis to duration and age of onset of epilepsy, and childhood febrile seizures in temporal lobectomy patients,” *Epilepsy Res.*, vol. 24, no. 2, pp. 119–126, Jun. 1996.
- [197] L. E. M. Wisse *et al.*, “Hippocampal subfield volumetry from structural isotropic 1 mm³ MRI scans: A note of caution,” *Hum. Brain Mapp.*, vol. 42, no. 2, pp. 539–550, Feb. 2021.
- [198] S. P. D. Dowhanik, N. Schieda, M. N. Patlas, F. Salehi, and C. B. van der Pol, “Doing more with less: CT and MRI utilization in Canada 2003–2019,” *Can. Assoc. Radiol. J.*, vol. 73, no. 3, pp. 592–594, Aug. 2022.
- [199] Y. Lee *et al.*, “On the signal-to-noise ratio benefit of spiral acquisition in diffusion MRI,” *Magn. Reson. Med.*, vol. 85, no. 4, pp. 1924–1937, Apr. 2021.
- [200] B. J. Wilm *et al.*, “Diffusion MRI with concurrent magnetic field monitoring,” *Magn. Reson. Med.*, vol. 74, no. 4, pp. 925–933, Oct. 2015.

- [201] R. N. Henriques, S. N. Jespersen, and N. Shemesh, “Evidence for microscopic kurtosis in neural tissue revealed by Correlation Tensor MRI,” *arXiv [physics.bio-ph]*, 23-Feb-2021.
- [202] B. Gok, G. Jallo, R. Hayeri, R. Wahl, and N. Aygun, “The evaluation of FDG-PET imaging for epileptogenic focus localization in patients with MRI positive and MRI negative temporal lobe epilepsy,” *Neuroradiology*, vol. 55, no. 5, pp. 541–550, May 2013.
- [203] T. Moritani, S. Ekholm, and P.-L. A. Westesson, *Diffusion-weighted MR imaging of the brain*, 2nd ed. Berlin, Germany: Springer, 2010.
- [204] A. A. Maudsley, “Multiple-line-scanning spin density imaging,” *J. Magn. Reson.*, vol. 41, no. 1, pp. 112–126, Oct. 1980.
- [205] M. Barth, F. Breuer, P. J. Koopmans, D. G. Norris, and B. A. Poser, “Simultaneous multislice (SMS) imaging techniques,” *Magn. Reson. Med.*, vol. 75, no. 1, pp. 63–81, Jan. 2016.
- [206] K. Setsompop, B. A. Gagoski, J. R. Polimeni, T. Witzel, V. J. Wedeen, and L. L. Wald, “Blipped-controlled aliasing in parallel imaging for simultaneous multislice echo planar imaging with reduced g-factor penalty,” *Magn. Reson. Med.*, vol. 67, no. 5, pp. 1210–1224, May 2012.
- [207] D. A. Feinberg, J. D. Hale, J. C. Watts, L. Kaufman, and A. Mark, “Halving MR imaging time by conjugation: demonstration at 3.5 kG,” *Radiology*, vol. 161, no. 2, pp. 527–531, Nov. 1986.
- [208] P. Jezzard and R. S. Balaban, “Correction for geometric distortion in echo planar images from B₀ field variations,” *Magn. Reson. Med.*, vol. 34, no. 1, pp. 65–73, Jul. 1995.
- [209] M. A. Griswold *et al.*, “Generalized Autocalibrating Partially Parallel Acquisitions (GRAPPA),” *Magn. Reson. Med.*, vol. 47, pp. 1202–1210, 2002.
- [210] A. D. Elster and J. H. Burdette, *Questions and answers in magnetic resonance imaging*, 2nd ed. St. Louis, MO: Mosby, 2001.
- [211] B. R. Rosen, V. J. Wedeen, and T. J. Brady, “Selective saturation NMR imaging,” *J. Comput. Assist. Tomogr.*, vol. 8, no. 5, pp. 813–818, Oct. 1984.

Curriculum Vitae

Name: Nico Joseph John Arezza

**Post-secondary
Education and
Degrees:** Toronto Metropolitan University
Toronto, Ontario, Canada
2016 B.Eng.

Toronto Metropolitan University
Toronto, Ontario, Canada
2018 M.Sc.

The University of Western Ontario
London, Ontario, Canada
2023 Ph.D.

**Honours and
Awards:**

Doctorate:

NSERC Canada Graduate Scholarship – Doctoral
2022-2023

NSERC Postgraduate Scholarship – Doctoral
2020-2022

Ontario Graduate Scholarship
2019

ISMARM Educational Stipend
2019, 2020, 2021

CAMPEP Quality Assurance Internship Award
2019

Queen Elizabeth II Graduate Scholarship
2018

Western Graduate Research Scholarship
2018, 2019, 2020, 2021, 2022

Master's:

Ryerson Graduate Fellowship
2016, 2017

Undergraduate:

NSERC Undergraduate Research Scholarship Award
2016

Gordon and Agnes Brash Award
2014

Academic Excellence Award
2014, 2015

Dean's List
2012, 2013, 2014, 2015, 2016

**Related Work
Experience**

Graduate Teaching Assistant
2020-2021
Western University
Calculus for Engineers, Linear Algebra, Physics I

Medical Physics Internship
2019
London Health Sciences Centre
Radiation Oncology department

Graduate Teaching Assistant
2016-2018
Toronto Metropolitan University
Mechanics, Waves and Fields, Physics I

Publications:*Peer-reviewed journal articles:*

NJJ Arezza, T Santini, M Omer, & CA Baron.
Estimation of free water-corrected microscopic fractional anisotropy. *Frontiers in Neuroscience* 17. March 2023. DOI: <https://doi.org/10.3389/fnins.2023.1074730>

NJJ Arezza, DHY Tse, & CA Baron.
Rapid microscopic fractional anisotropy imaging via an optimized linear regression formulation. *Magnetic Resonance Imaging* 80:132-143. July 2021. DOI: [10.1016/j.mri.2021.04.015](https://doi.org/10.1016/j.mri.2021.04.015)

NJJ Arezza, M Razani, & MC Kolios.

Dynamic light scattering optical coherence tomography to probe motion of subcellular scatterers. *Journal of Biomedical Optics* 24(2):025002. February 2019. DOI: 10.1117/1.jbo.24.2.025002

Manuscripts in progress:

NJJ Arezza, H Abbas, C Chadwick, IS Johnsrude, JG Burneo, AR Khan, & CA Baron.
Evidence for microscopic fractional anisotropy asymmetry in unilateral temporal lobe epilepsy. medRxiv. 2023.

Theses/Dissertations:

NJJ Arezza.

Development of dynamic light scattering optical coherence tomography techniques for detecting cell death. MSc Thesis (Toronto Metropolitan University). August 2018.

Presentations:

- i. International

NJJ Arezza, T Santini, M Omer, & CA Baron.

Microscopic fractional anisotropy with free water elimination. ISMRM 2023. June 2023.

NJJ Arezza, JG Burneo, AR Khan, & CA Baron.

Microscopic fractional anisotropy may be sensitive to unilateral hippocampal abnormalities in temporal lobe epilepsy. ISMRM 2022. May 2022.

N Rahman, K Xu, NJJ Arezza, K Borsos, M Budde, A Brown, & CA Baron.

Microstructural diffusion MRI in mouse models of severe and repetitive mild traumatic brain injury. ISMRM 2021. May 2021.

NJJ Arezza, & CA Baron.

Cerebrospinal fluid partial volume effects in microscopic fractional anisotropy imaging. ISMRM 2021. May 2021.

NJJ Arezza, DHY Tse, A Arbabi, & CA Baron.

Clinical microscopic fractional anisotropy imaging in 4 minutes: an optimization approach. ISMRM 2020. August 2020.

NJJ Arezza, DHY Tse, & CA Baron.

An optimised diffusion MRI technique to study neuron microstructure. AAPM/COMP Joint Annual Scientific Meeting 2020. July 2020.

NJJ Arezza, A Arbabi, & CA Baron.

Toward clinically viable and robust measurement of microscopic diffusion anisotropy. ISMRM 2019. May 2019.

MJ Moore, C Hernandez, **NJJ Arezza**, AA Exner, & MC Kolios.
Indirect assessment of nanobubble size through agarose trapping and ultrasound M-mode imaging. IEEE IUS. October 2018.

M Razani, A Zam, **NJJ Arezza**, YJ Wang, & MC Kolios.
Visualization and characterization of the acoustic radiation force assisted displacement of particles using an OCT technique. SPIE BIOS. February 2016.

ii. National

NJJ Arezza, JG Burneo, AR Khan, & CA Baron.
Diffusion anisotropy imaging in temporal lobe epilepsy. COMP Annual Scientific Meeting 2022. June 2022.

N Rahman, K Xu, **NJJ Arezza**, K Borsos, A Brown, & CA Baron.
Microstructural diffusion MRI in mouse models of severe and repetitive mild traumatic brain injury. IMNO 2021. March 2021.

M Omer, N Rahman, **NJJ Arezza**, & CA Baron.
Reliability assessment of cerebrospinal fluid suppressed microscopic fractional anisotropy. IMNO 2021. March 2021.

NJJ Arezza, DHY Tse, & CA Baron.
Microscopic fractional anisotropy imaging in the human brain: an optimized kurtosis approach vs. the gamma model. IMNO 2021. March 2021.

N Rahman, FN Mushtaha, TK Kuehn, **NJJ Arezza**, AR Khan, A Brown, & CA Baron.
Beyond the diffusion tensor: validation of advanced approaches for microstructural diffusion MRI. IMNO 2020. March 2020.

NJJ Arezza & CA Baron.
An optimised diffusion MRI technique to study white matter integrity. IMNO 2020. March 2020.

NJJ Arezza, A Arbabi, & CA Baron.
Clinically-viable and robust measurement of microscopic diffusion anisotropy. IMNO 2019. March 2019.